Title
Evidence for the production of two W bosons with the same electric charge and two jets in 20.3 fb^{-1} of pp collisions at $\sqrt{s} = 8$ TeV using the ATLAS detector

Author
Sood, Alexander

Publication Date
2014

Peer reviewed|Thesis/dissertation

Evidence for the production of two W bosons with the same electric charge and two jets in 20.3 fb^{-1} of pp collisions at $\sqrt{s} = 8$ TeV using the ATLAS detector

By

Alexander Sood

A dissertation submitted in partial satisfaction of the

requirements for the degree of

Doctor of Philosophy

in

Physics

in the

Graduate Division

of the

University of California, Berkeley

Committee in charge:

Professor Beate Heinemann, Chair
Professor Yury Kolomensky
Professor Eric Norman

Fall 2014

Abstract

Evidence for the production of two W bosons with the same electric charge and two jets in 20.3 fb^{-1} of pp collisions at $\sqrt{s} = 8$ TeV using the ATLAS detector

by

Alexander Sood

Doctor of Philosophy in Physics

University of California, Berkeley

Professor Beate Heinemann, Chair

This dissertation presents a measurement of $W^{\pm}W^{\pm}jj$ production in proton-proton collisions with a center-of-mass energy of 8 TeV at the Large Hadron Collider using the ATLAS detector. The W bosons are required to decay leptonically, giving a signature of two leptons of the same electric charge, two jets, and missing transverse energy. The analysis is performed on the entire 8 TeV dataset, corresponding to an integrated luminosity of 20.3 fb^{-1}. The cross section is measured in two fiducial regions, and an excess over the background-only prediction is observed with a significance of 4.5σ for inclusive $W^{\pm}W^{\pm}jj$ production and 3.6σ for electroweak $W^{\pm}W^{\pm}jj$ production. The measured cross sections are in agreement with Standard Model predictions, and limits are set on anomalous quartic gauge couplings.

Contents

1 Introduction **1**

2 Theoretical Introduction **4**
2.1 Standard Model 5
2.1.1 Gauge Structure of the Standard Model 6
2.1.2 Electroweak Symmetry Breaking 11
2.2 $W^{\pm}W^{\pm}jj$ Production at the LHC 17
2.3 Anomalous Quartic Gauge Couplings 20
2.3.1 Effective Field Theory 21
2.3.2 The Electroweak Chiral Lagrangian 22
2.3.3 Unitarization 23
2.3.4 Constraints from electroweak precision tests 24

3 The Large Hadron Collider **26**
3.1 Injection Chain 29
3.2 Run 1 Performance 31

4 The ATLAS Detector **33**
4.1 Inner Detector 34
4.1.1 Pixel Detector 36
4.1.2 Semi-Conductor Tracker 37
4.1.3 Transition Radiation Tracker 37
4.2 Calorimeter 38
4.2.1 EM Calorimeter 38
4.2.2 Hadronic Tile Calorimeter 40
4.2.3 Hadronic Endcap and Forward Calorimeters 41
4.3 Muon Spectrometer 42
4.3.1 Precision Chambers 43
4.3.2 Trigger Chambers 43

4.4 Trigger System 44

5 Object Reconstruction and Event Selection 46

5.1 Track and Vertex Reconstruction 46

5.2 Electron Reconstruction 48

5.3 Muon Reconstruction 50

5.4 Jet Reconstruction 51

5.4.1 Tagging b jets 54

5.5 $E_{\mathrm{T}}^{\mathrm{miss}}$ Reconstruction 55

5.6 Event Selection 57

6 Signal and Background Estimation 60

6.1 Prompt Processes 61

6.1.1 $W^{\pm}W^{\pm}$ 61

6.1.2 $W^{\pm}Z$ 62

6.1.3 Other Prompt Backgrounds 66

6.2 Background from Photon Conversions 66

6.2.1 Charge Misidentification 66

6.2.2 $W^{\pm}\gamma$ 69

6.3 Other Non-prompt Background 72

7 Systematic Uncertainties 79

7.1 Uncertainties due to Theoretical Modeling 79

7.2 Systematic Uncertainties from Object Reconstruction/Identification 81

7.2.1 Jet Uncertainties 82

7.2.2 Lepton Uncertainties 85

7.2.3 $E_{\mathrm{T}}^{\mathrm{miss}}$ Uncertainties 85

7.2.4 Additional Uncertainties 86

7.3 Systematic Uncertainties on Data-Driven Background Estimates 88

7.3.1 Charge-misID Background 88

7.3.2 Non-prompt Background 90

7.4 Summary 97

8 Jet Energy Scale Performance Studies Using Z+jet Events 99

8.1 Event Selection 100

8.2 Measuring Average p_{T} Balance 101

8.3 FCAL High Voltage Problem 107

8.4 Results 108

9 Results **111**
9.1 Summary of Control Region Observations 111
9.2 Signal Region Observations 111
9.3 Testing the Standard Model Hypothesis 117
9.4 Testing aQGC Hypotheses 120

10 Conclusions and Outlook **125**

A Description of Author Contributions **135**

B The FE-I4 Chip **137**
B.1 Single Pixel 137
B.2 Overall Structure 138
B.3 Generic ADC 139

List of Figures

1.1 Example diagram of WW scattering at the LHC. Two quarks from the incoming protons radiate W bosons which then interact with each other. 2
1.2 Examples of non-VBS diagrams that contribute to (a) electroweak production and (b) strong production of the $VVjj$ final state. 3

2.1 Leading-order diagram (left) and an example next-to-leading-order diagram (right) for $e^+e^- \to \mu^+\mu-$. 7
2.2 Full photon propagator as a perturbation series in the contribution from one-particle-irreducible insertions (top), which sums over all one-particle-insertion diagrams (bottom). 8
2.3 Measurements of the strong coupling α_s at energies ranging from ~2 GeV almost up to 1 TeV [8]. 10
2.4 Leading order diagrams for $W^\pm W^\pm$ scattering involving triple gauge couplings in the t-channel (left) and u-channel (middle) and quartic gauge couplings (right). 15
2.5 Vector boson scattering diagrams with Higgs exchange in the t-channel (left) and u-channel (right). 17
2.6 A few leading order diagrams for electroweak $W^\pm W^\pm jj$ production. 18
2.7 CT10 parton distribution functions for $Q^2 = 10$ GeV^2 and $Q^2 = 10000$ GeV^2 [13]. 20
2.8 Vector boson scattering cross sections (nb) for the Standard Model without a Higgs with (right) and without (left) K-matrix unitarization [37]. 24
2.9 Example diagram for one-loop contribution of quartic gauge interactions to the gauge boson self-energies. 24

3.1 Layout of the LHC [38]. 27

3.2 Schematic of cryomodule containing four RF cavities [38]. . . 27
3.3 Cross section of LHC dipole magnet [39]. 28
3.4 Injection chain for the LHC [40]. 30
3.5 Integrated luminosity as a function of time delivered by the LHC and recorded by the ATLAS detector [43]. 32

4.1 Illustration of the ATLAS detector with various subsystems indicated [45]. 34
4.2 View of the barrel region of the ATLAS Inner Detector [44]. . 35
4.3 Schematic showing the cells in a barrel module of the EM calorimeter [44]. 39
4.4 Sketch showing the structure of the tile calorimeter [44]. . . . 40
4.5 Arrangement of endcap and forward calorimeters [44]. 41
4.6 Sketch of the ATLAS muon system [50]. 42

5.1 Track reconstruction efficiency for tracks belonging to muons, pions, and electrons with a p_{T} of 5 GeV [51]. 47
5.2 Vertex reconstruction efficiency as a function of the number of reconstructed tracks. Figure taken from Ref. [53]. 48
5.3 Electron reconstruction and identification efficiency as a function of p_{T} (left) and η (right). Filled points show the efficiencies measured in data while efficiencies measured in MC are indicated by the open points. Figure taken from Ref. [55]. . . 50
5.4 Muon reconstruction efficiency as a function of η. Filled points show the efficiencies measured in data while efficiencies measured in MC are indicated by the open points. Figure taken from Ref. [58]. 53
5.5 Jet reconstruction efficiency as a function of truth jet p_{T} for jets with $\eta < 1.9$ [59]. 53
5.6 Jet energy resolution as a function of the average p_{T} of the two jets in the event for jets calibrated using EM+JES (left) and LCW+JES (right). Filled points show the resolution measured in data while the resolution measured in MC is indicated by the open points. Figure taken from Ref. [61]. . . 54
5.7 Number of reconstructed jets as a function of the number of reconstructed vertices with and without requiring the jet vertex fraction to be greater than 0.75. Figure taken from Ref. [64]. 56

5.8 Efficiency as a function of p_{T} (left) and $|\eta|$ (right) in simulated $t\bar{t}$ events for b, c, and light jets to pass a selection on the MV1 output calibrated to have an efficiency of 70% for b jets with p_{T} greater than 20 GeV and $|\eta| < 2.5$. Figure taken from Ref. [66]. 56
5.9 $E_{\mathrm{x}}^{\mathrm{miss}}$ and $E_{\mathrm{y}}^{\mathrm{miss}}$ resolution as a function of the scalar sum of all transverse energy in the calorimeter and the transverse momenta of any muons in the event. Figure taken from Ref. [68]. 57

6.1 Representative diagrams for tZj production with the subsequent top decay yielding WZ plus two jets. 62
6.2 Lepton p_{T} (left) and η (right) distributions for the leading (top) and sub-leading (bottom) leptons for $e\mu$ and $\mu\mu$ events in the ≤ 1 jet control region. 64
6.3 Di-jet invariant mass distribution (left) and rapidity difference distribution (right) for events in the tri-lepton control region. 65
6.4 Illustration of the "trident" process. If most of the energy of the original e^- ends up with the e^+, it is likely that only the e^+ will be reconstructed. Since the momentum of this lepton is very similar to that of the original prompt lepton, this is referred to as charge misidentification. 68
6.5 Charge-misID rates derived for electrons as a function of $|\eta|$ (left) and as a function of both $|\eta|$ and p_{T}. 68
6.6 Difference between true energy and reconstructed energy for electrons reconstructed with the correct charge (black), electrons reconstructed with the wrong charge due to the trident process (blue), and electrons reconstructed with the wrong charge when no trident was evident in the MC truth record (red). 70
6.7 Energy bias (left) and smearing (right) corrections in units of GeV derived using $Z \to ee$ MC. 70
6.8 Electron η distributions for the leading (left) and sub-leading (right) electrons in the ≤ 1 jet control region. 71
6.9 Di-electron invariant mass distribution for events in the ≤ 1 jet control region. 71
6.10 $m_{\mathrm{T}}(\ell, E_{\mathrm{T}}^{\mathrm{miss}}$ distribution for events with a tight electron (left) or muon (right) after all other di-jet selections have been applied. 74

6.11 Average p_{T} of the jet vs. loose lepton p_{T} + $E_{\mathrm{T}}^{\mathrm{iso}}$ for events passing the di-jet selection. 74
6.12 $E_{\mathrm{T}}^{\mathrm{iso}}$ (top) and $p_{\mathrm{T}}^{\mathrm{iso}}$ (bottom) as fractions of lepton p_{T} for loose electrons (left) and muons (right). The black curve shows the distribution for the TL region while the pink and green points show the distribution for the di-jet region before and after reweighting. 75
6.13 Fake factors as a function of lepton p_{T} (top) and $|\eta|$ (bottom) for electrons (left) and muons (right). 76
6.14 Lepton p_{T} distributions for the leading (left) and sub-leading (right) leptons in the b-tag control region. 78

7.1 Relative uncertainty on in situ JES corrections as a function of p_{T} (top) for jets with $|\eta|$ around 0.5 (left) and 2.0 (right) and as a function of η (bottom) for jets with p_{T} near 25 GeV (left) and 300 GeV (right). Figure taken from Ref. [83]. . . . 83
7.2 Jet η distributions for the leading (left) and sub-leading (right) jets in WZ MC. The yellow histogram contains all events while the red histogram contains only events in which both jets are matched to the primary interaction using truth information. The difference between the two is taken as a systematic uncertainty. 86
7.3 Electron η distribution for the ee (left) and $e\mu$ (right) channels. The red(blue) points show the effect of scaling events by charge-misID scale factors when those scale factors are greater(less) than one. 87
7.4 Uncertainty on the fake factor for electrons (left) and muons (right) due to the modeling of prompt contamination in the di-jet region. 92
7.5 Uncertainty on the fake factor for electrons (left) and muons (right) from variations of the selections used to define the di-jet region. 94
7.6 Comparison of derived underlying jet p_{T} distributions to the true distribution for different variations of the slope of the line relating lepton p_{T} + $E_{\mathrm{T}}^{\mathrm{iso}}$ to jet p_{T} for electrons (left) and muons (right) in $t\bar{t}$ (top) and W+jets MC samples. . . . 95
7.7 Uncertainty on the fake factor for electrons (left) and muons (right) due to the reweighting of the underlying jet p_{T} distribution. 98

8.1 The p_{T} balance between the leading jet and the Z boson is spoiled by additional QCD radiation, so the projection of the Z p_{T} onto the jet axis is used. 100
8.2 p_{T} balance distributions for jets calibrated with EM+JES with $|\eta| < 1.2$ and 20 GeV $< p_{\mathrm{T}}^{\mathrm{ref}} <$ 25 GeV (left), 35 GeV $< p_{\mathrm{T}}^{\mathrm{ref}} <$ 45 GeV (right), and 80 GeV $< p_{\mathrm{T}}^{\mathrm{ref}} <$ 100 GeV (middle). The mean (μ) and RMS (σ) of each distribution is indicated in the text labels along with the ratio of the means. 102
8.3 p_{T} balance distributions for $p_{\mathrm{T}}^{\mathrm{ref}}$ between 20 GeV and 25 GeV and $|\eta| < 1.2$ for jets calibrated with EM+JES (left) and LCW+JES (right) when requiring the leading jet to have $p_{\mathrm{T}} > 12$ GeV. Neither shape fits a Poisson with a linear turn-on between $12/p_{\mathrm{T}}^{\mathrm{ref,max}} = 0.48$ and $12/p_{\mathrm{T}}^{\mathrm{ref,min}} = 0.6$. The mean ($\mu$) and width ($\sigma$) of Poisson fitted to each distribution is indicated in the text labels along with the ratio of the means. 103
8.4 p_{T} balance distributions for jets calibrated with EM+JES with $|\eta| < 1.2$ and 20 GeV $< p_{\mathrm{T}}^{\mathrm{ref}} <$ 25 GeV (left), 35 GeV $< p_{\mathrm{T}}^{\mathrm{ref}} <$ 45 GeV (right), and 80 GeV $< p_{\mathrm{T}}^{\mathrm{ref}} <$ 100 GeV (middle). Each distribution is fit with a Poisson function convoluted with a linear turn-on. The mean (μ) and width (σ) of Poisson fitted to each distribution is indicated in the text labels along with the ratio of the means. 104
8.5 p_{T} balance distributions for $p_{\mathrm{T}}^{\mathrm{ref}}$ between 20 GeV and 25 GeV and $|\eta| < 1.2$ for jets calibrated with EM+JES (left) and LCW+JES (right) when requiring the leading jet to have $p_{\mathrm{T}} > 12$ GeV. The template fit used shows good agreement with the distributions but doesn't fix the bias. The half-width at half of the maximum (σ) and mean of the template between the half-maxima (μ) are indicated in the text labels for the fit to each distribution along with the ratio of the means. . . 105
8.6 p_{T} balance distributions for jets calibrated with EM+JES with $|\eta| < 1.2$ and 20 GeV $< p_{\mathrm{T}}^{\mathrm{ref}} <$ 25 GeV (left), 35 GeV $< p_{\mathrm{T}}^{\mathrm{ref}} <$ 45 GeV (right), and 80 GeV $< p_{\mathrm{T}}^{\mathrm{ref}} <$ 100 GeV (middle). Each distribution is fit with a template constructed from the MC. The half-width at half of the maximum (σ) and mean of the template between the half-maxima (μ) are indicated in the text labels for the fit to each distribution along with the ratio of the means. 106

8.7 p_{T} balance distributions for data taken before the installation of faulty HV modules (solid line) and data taken while the faulty units were in place (points). Average p_{T} balance is measured using the template fit method, with the distribution for the data taken with good HV units used for the template. The half-width at half of the maximum (σ) and mean of the template between the half-maxima (μ) are indicated in the text labels for the fit to each distribution along with the ratio of the means. 107
8.8 Average value of $\frac{p_T^{jet}}{p_T^{ref}}$ for EM+JES-calibrated jets as a function of p_T^{ref} for four bins in jet η with the data/MC double-ratio shown at the bottom. The yellow band on the double-ratio plot shows the systematic uncertainty from the jet energy scale. 109
8.9 Average value of $\frac{p_T^{jet}}{p_T^{ref}}$ for LCW+JES-calibrated jets as a function of p_T^{ref} for four bins in jet η with the data/MC double-ratio shown at the bottom. The yellow band on the double-ratio plot shows the systematic uncertainty from the jet energy scale. 110

9.1 $|\Delta y_{jj}|$ distribution for events in the low m_{jj} control region. The top panel shows the number of events for the data (points) and the Standard Model prediction (histogram) while the points in the bottom panel show the ratio of data/prediction. The systematic uncertainty on the prediction is indicated by the hatched band in the top panel and solid band in the bottom panel. 112
9.2 (a) The di-jet invariant mass distribution for events passing all signal selections before the m_{jj} requirement is applied (b) the Δy_{jj} distribution of events in the inclusive SR. In the bottom panel of the m_{jj} plot, the points show the ratio of data to the predicted background while the line and hatched band give the ratio of the total prediction (signal + background) to the background prediction and the systematic uncertainty on this ratio. 114
9.3 VBS SR distributions for (a) the transverse mass formed using both leptons and missing transverse energy and (b) the scalar sum of the lepton momenta. 115

9.4 Scalar sum of the lepton momenta in the VBS signal region. The Standard Model prediction ($\alpha_4 = \alpha_5 = 0$) is given by the solid histogram, and the red line shows how the prediction would change for $\alpha_4 = 0.1$. 116
9.5 VBS SR distributions for (a) the lepton centrality and (b) the jet multiplicity, which include the requirement $|\Delta y_{jj}| > 2.4$. The points show the observed data while the stacked histogram gives the SM prediction. 117
9.6 Sum of the lepton charges for events in the VBS signal region, which includes the requirement $|\Delta y_{jj}| > 2.4$. The points show the observed data while the stacked histogram gives the SM prediction. 119
9.7 Measured fiducial cross sections for electroweak+strong production in the inclusive SR(left) and electroweak+interference in the VBS SR(right). The inner red bands indicate the uncertainties on the measured cross sections due only to statistics while the outer blue bands give the total uncertainty. . . 120
9.8 Fiducial cross section for electroweak $W^{\pm}W^{\pm}jj$ production, determined using WHIZARD and scaled to include interference, as a function of α_4 and α_5. Contours of constant cross section form ellipses in the (α_4, α_5) plane. 121
9.9 Efficiency as a function of the fiducial cross section for electroweak $W^{\pm}W^{\pm}jj$ production in the VBS SR for (a) the ee channel, (b) the $e\mu$ channel, and (c) the $\mu\mu$ channel. 122
9.10 Limits on (α_4, α_5). Points outside the light blue ellipse are excluded at 95% CL while points outside the dark blue ellipse are excluded at 68% CL. 123
9.11 Expected (dashed) and observed (solid) profile likelihoods as a function of α_4 (left) and α_5 (right). 124

10.1 Projected sensitivity to the $\frac{f_{S,0}}{\Lambda^4}$ coupling from future measurements of $W^{\pm}W^{\pm}jj$ production at the LHC. 126

B.1 Schematic of an analog pixel circuit for the FE-I4. Figure taken from Ref. [93] 138
B.2 Schematic drawing showing the layout of the FE-I4 chip, not drawn to scale. Figure taken from Ref. [93] 139

List of Tables

2.1 Fundamental particles of the Standard Model [8]. 5

6.1 Event counts in the ≤ 1 jet control region. 63
6.2 Event counts in the tri-lepton control region. 65
6.3 Event counts in the b-tag control region. 73

7.1 Total theoretical uncertainties for the $W^{\pm}W^{\pm}jj$ and $W^{\pm}Zjj$ processes in the Inclusive and VBS signal regions (SR). 81
7.2 Summary of uncertainties on the charge-misID background. The final two rows indicate channel-specific uncertainties that are applied in addition to the uncertainty given in the "Total" row. This final uncertainty varies considerably depending on the fraction of the charge-misID background in a given region/channel that is expected to come from $t\bar{t}$ events. 88
7.3 Test comparing the prediction from scaling opposite-sign events by the charge-misID rate to the direct same-sign prediction in Drell-Yan MC. The SS Z region inverts the Z veto used in the signal selection while making no cuts on jets, and the VBF-like SS Z region additionally requires two jets with $m_{jj} >$ 150 GeV. The low N$_{jet}$ CF region does not apply a Z veto but is otherwise similar to the ≤ 1 jet control region, and the SS Incl. region requires only two same-sign leptons with no further selections. 89
7.4 Test comparing the prediction from scaling opposite-sign events by the charge-misID rate to the direct same-sign prediction in $t\bar{t}$ MC. 90
7.5 Contribution in weighted number of events from events where both leptons originate from hadronic activity and from events with two prompt leptons compared to the final non-prompt background prediction (including subtraction of these effects). 91

7.6 Comparison of observed event yields and the MC prediction for processes that produce prompt leptons with no m_T cut applied $\Delta\phi(\ell, j)$ required to be less than 2. The relative difference between the predicted and observed event yields is used to estimate the systematic uncertainty on the non-prompt background prediction due to the modeling of prompt contamination in the di-jet sample. 92
7.7 Summary of systematic uncertainties on the non-prompt background prediction due to uncertainties on the fake factor . . . 93
7.8 Comparison of non-prompt background predictions for the $\mu\mu$ channel using fake factors derived in the di-jet region and a "high-d_0" region in which both muons must have $d_0/\sigma(d_0) > 3$. 96
7.9 Summary of systematic uncertainties in the inclusive signal region. The left column indicates uncertainties as a percentage of the total background prediction while the right column indicates uncertainties as a percentage of the total signal prediction. 97
7.10 Summary of systematic uncertainties in the VBS signal region. The left column indicates uncertainties as a percentage of the total background prediction while the right column indicates uncertainties as a percentage of the total signal prediction. 98

9.1 Event counts in the low m_{jj} control region. Observed event yields agree well with the Standard Model prediction. 112
9.2 Comparison of predicted ("pred.") and observed ("data") event counts for all control regions. 113
9.3 Predicted and observed event counts in the signal regions. The "Total background" includes strong $W^{\pm}W^{\pm}jj$ production in the VBS region but not in the inclusive region, where both strong and electroweak production are treated as signal. 113
9.4 Probability (α) corresponding to a given significance (Z) [8]. 119

Chapter 1

Introduction

One of the major triumphs in the last half century of particle physics has been the successful unified description of the electromagnetic and weak force as a spontaneously broken gauge symmetry. For many years, results from particle colliders provided confirmation of this theory, through the discovery of the W and Z bosons predicted by the theory and by measuring their couplings to matter, but the nature of the symmetry breaking remained a mystery. The Large Hadron Collider (LHC) has begun to shed some light on this subject with the discovery a new spin-0 particle consistent with the HIggs boson of the Standard Model. It could be that the next 30 years of particle physics will follow the previous 30 years with precise measurements of Higgs properties continuing to confirm the Standard Model picture of electroweak symmetry breaking, but it is also possible that there are other new particles that play a role.

If these new particles are light enough, they may be observed directly at the LHC, but their effects can also be seen in the scattering of W and Z bosons [1, 2] ($VV \to VV$, where $V = W, Z$). Without the Higgs boson, the scattering of longitudinally-polarized bosons violates unitarity at center-of-mass energies around 1 TeV [3–5]. If the observed Higgs is not solely responsible for electroweak symmetry breaking, there can still be some residual growth of the scattering amplitude with energy that is prevented from violating unitarity at higher energies by the presence of additional particles. There are no previous measurements of processes that involve the quartic interaction of W and Z bosons. The theoretical implications of vector boson scattering (VBS) cross sections combined with the lack of experimental exploration make this an interesting process to study.

Figure 1.1 depicts how vector boson scattering occurs at the LHC. This

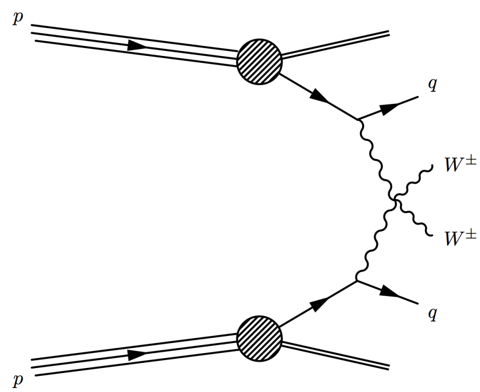

Figure 1.1: Example diagram of WW scattering at the LHC. Two quarks from the incoming protons radiate W bosons which then interact with each other.

leads to a final state that includes not only the two bosons but also two jets due to the quarks. There are several other diagrams that produce the same final state, examples of which are shown in Figure 1.2. The complete set of diagrams can be separated two classes that are each gauge invariant. The first involves only electroweak interactions at leading order and includes vector boson scattering (as shown in Figure 1.1) as well as other diagrams of order α_{EW}^4 like the one shown in Figure 1.2a. This will be referred to as electroweak production. The second, termed strong production, consists of diagrams, like the one shown in Figure 1.2b that contain both strong and electroweak interactions. For most choices of the two vector bosons, electroweak production is hard to measure because it is dwarfed by strong production. However, for two W bosons with the same electric charge, the cross sections for the two kinds of processes are comparable.

This dissertation presents a detailed description of the measurement in Ref. [6], which reports the first evidence for the electroweak production of two W bosons with the same electric charge in association with two jets. The measurement is performed using 20.3 fb^{-1} of proton-proton collision data with a center-of-mass energy of 8 TeV, provided by the LHC and collected using the ATLAS detector. The W bosons are required to decay leptonically ($W^\pm \to \ell^\pm \nu$, where $\ell = e, \mu$). Since neutrinos escape the interaction point without being detected, this leads to an experimental signature of two leptons with the same electric charge, two jets, and a transverse momentum imbalance.

The remaining chapters are organized as follows: Chapter 2 gives a the-

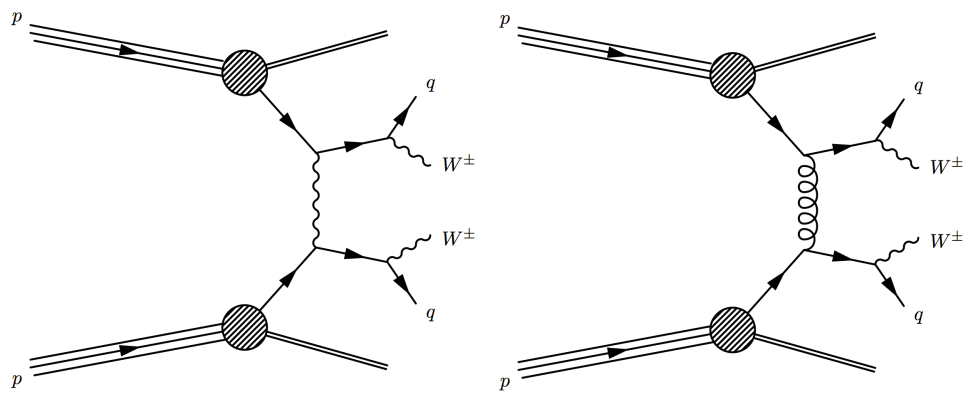

(a) (b)

Figure 1.2: Examples of non-VBS diagrams that contribute to (a) electroweak production and (b) strong production of the $VVjj$ final state.

oretical overview of the Standard Model and anomalous gauge couplings. Chapters 3 and 4 describe the LHC and the ATLAS detector. Chapter 5 discusses the reconstruction of physical objects from detector data and how events are selected using these objects. Chapter 6 explains how contributions to the selected events from various physical processes are estimated. Chapter 7 covers sources of systematic uncertainty on the measurement and how these uncertainties are estimated. Chapter 8 describes a study of jet energy scale performance using Z+jet events. The results of the measurement are shown in Chapter 9, and conclusions are presented in Chapter 10.

Chapter 2

Theoretical Introduction

The fundamental constituents of matter and their interactions are described with remarkable accuracy by the Standard Model, which has remained basically unchanged for 40 years. In that time, the Standard Model has been repeatedly validated by the discovery of new particles that play important roles in the theory. These discoveries include the W and Z bosons (weak force carriers), the third generation of fermions (needed to get CP violation in the Standard Model), and the Higgs boson (explains particle masses except for neutrinos). The first part of this chapter is devoted to a brief review of the Standard Model. A more complete description of the Standard Model and of quantum field theory, in general, is given in Ref. [7].

While the theory does an outstanding job of describing the phenomena it seeks to explain, the Standard Model also leaves several puzzles unsolved. For example, it contains no description of gravity or dark matter. Though it contains a mechanism for CP violation, the amount is too small to explain the matter/anti-matter asymmetry in the universe. There is no explanation for non-zero neutrino masses and the arbitrary scattering of fermion masses across several orders of magnitude or for why the universe has the symmetry group $SU(3)_C \otimes SU(2)_L \otimes U(1)_Y$. Several extensions of the Standard Model have been proposed to explain some of these puzzles. This measurement is not interpreted in the context of a particular model for new physics. Instead, the measured rate of $W^{\pm}W^{\pm}jj$ production is compared to an effective theory parameterizing the low-energy effects on vector boson scattering from new physics at high energies. Effective theories are described toward the end of the chapter.

Particle	Spin	Electric Charge	Color	Mass
Leptons				
Electron/Muon/Tau	1/2	-1	singlet	0.511 MeV/0.106 GeV/1.78 GeV
Electron/Muon/Tau neutrino	1/2	0	singlet	$<$ 2 eV/$<$ 0.19 MeV/$<$ 18 MeV
Quarks				
Up/Charm/Top	1/2	+2/3	triplet	2.3 MeV/1.28 GeV/173 GeV
Down/Strange/Bottom	1/2	-1/3	triplet	4.8 MeV/95 MeV/4.18 GeV
Gauge Bosons				
Gluon	1	0	octet	0
Photon	1	0	singlet	0
W	1	$\pm$1	singlet	80.4 GeV
Z	1	0	singlet	91.2 GeV
Higgs	0	0	singlet	125.6 GeV

Table 2.1: Fundamental particles of the Standard Model [8].

2.1 Standard Model

The particles of the Standard Model are summarized in Table 2.1. Matter in the Standard Model is made up of spin-1/2 fermions and comes in three generations. Each generation consists of two quarks, which experience both strong and electroweak interactions, and two leptons, which experience only electroweak interactions. The two quarks contain one up-type quark with an electric charge of Q =+2/3 and one down-type quark with Q =-1/3, while the two leptons are one charged lepton with Q =-1 and one neutrino with Q =0. The three generations of matter differ only by the masses of the particles. The lightest generation consists of the up (u) quark, the down (d) quark, the electron (e), and the electron neutrino (ν_e). For the second and third generation, the corresponding particles are the charm (c) and top (t) quarks, the strange (s) and bottom (b) quarks, the muon (μ) and tau lepton (τ), and their associated neutrinos (ν_μ,ν_τ).

Forces in the Standard Model are described by gauge symmetries, which predict the existence of massless spin-1 bosons to mediate these interactions. The boson responsible for carrying the electromagnetic force is the photon (γ). Eight gluons (g) are the force carriers for the strong nuclear force, and the weak nuclear force is mediated by the $W^{\pm}$ and Z bosons. The weak bosons are not massless as would be predicted by a plain gauge theory. In fact, they have quite large masses, nearly 100 times the mass of the proton.

In the Standard Model, this is explained by a spontaneous breaking of the electroweak gauge symmetry due to the presence of a spin-0 field. This is discussed in more detail in Section 2.1.2 and leads to the prediction of one fundamental spin-0 boson, called the Higgs boson.

2.1.1 Gauge Structure of the Standard Model

The symmetry group of the Standard Model is $SU(3)_C \otimes SU(2)_L \otimes U(1)_Y$. $SU(3)_C$ is the symmetry group of the strong interaction while $SU(2)_L \otimes U(1)_Y$ describes electroweak interactions. Fermions that are charged under a particular force transform as $\psi \rightarrow e^{i\alpha^a(x)\tau^a}\psi$ under the associated symmetry, where τ^a are the generators of that symmetry. Quarks come in three colors that transform as a triplet under $SU(3)_C$, left-handed fermions form $SU(2)_L$ doublets ($\begin{pmatrix} u_L \\ d_L \end{pmatrix}$, $\begin{pmatrix} \nu_L \\ e_L \end{pmatrix}$), and all Standard Model fermions carry hypercharge (are charged under $U(1)_Y$). Hypercharge is related to electric charge by $Q = T^3 + Y$, where T^3 is the $SU(2)_L$ quantum number of the particle ($\pm\frac{1}{2}$ for left-handed fermions and 0 for right-handed fermions). These symmetries are required to symmetries of the Lagrangian, but this will clearly not be the case in a theory that involves only fermions. Using the transformation law given above, we get:

$$\begin{aligned}
\mathcal{L} &= i\bar{\psi_L}\gamma^\mu\partial_\mu\psi_L + i\bar{\psi_R}\gamma^\mu\partial_\mu\psi_R - m(\bar{\psi_L}\psi_R + \bar{\psi_R}\psi_L) \\
&\rightarrow i\bar{\psi_L}V^\dagger\gamma^\mu\partial_\mu(V\psi_L) + i\bar{\psi_R}U^\dagger\gamma^\mu\partial_\mu(U\psi_R) - m(\bar{\psi_L}V^\dagger U\psi_R + \bar{\psi_R}U^\dagger V\psi_L) \\
&= i\bar{\psi_L}\gamma^\mu\partial_\mu\psi_L + i\bar{\psi_R}\gamma^\mu\partial_\mu\psi_R + i\bar{\psi_L}V^\dagger\gamma^\mu\partial_\mu(V)\psi_L + i\bar{\psi_R}U^\dagger\gamma^\mu\partial_\mu(U)\psi_R \\
&- m(\bar{\psi_L}V^\dagger U\psi_R + \bar{\psi_R}U^\dagger V\psi_L)
\end{aligned} \tag{2.1}$$

where $V(x) = e^{i\alpha_L^a(x)\tau_L^a}$ and $U(x) = e^{i\alpha_R^a(x)\tau_R^a}$ are the transformations for left-handed and right-handed fermions under the symmetry in question. As long as left-handed and right-handed fermions transform in the same way ($V = U$), the mass term will be invariant, but an extra piece remains from the transformation of the kinetic term. This can be remedied by adding to the Lagrangian a term coupling fermions to new spin-1 particles, $g\bar{\psi_L}\gamma^\mu A_\mu^a\tau^a\psi_L$, where g is a dimensionless constant and the symmetry transformation of the new field is given by $A_\mu^a\tau^a \rightarrow V(A_\mu^a\tau^a + \frac{i}{g}\partial_\mu)V^\dagger$ (and similarly for the right-handed fermions). This term is also not invariant under the symmetry:

$$
\begin{aligned}
\mathcal{L}_{int} &= g\bar{\psi_L}\gamma^\mu A^a_\mu \tau^a \psi_L \\
&\rightarrow g\bar{\psi_L}V^\dagger\gamma^\mu V(A^a_\mu\tau^a + \frac{i}{g}\partial_\mu)V^\dagger(V\psi_L) \\
&= g\bar{\psi_L}V^\dagger V\gamma^\mu A^a_\mu\tau^a V^\dagger V\psi_L + i\bar{\psi_L}V^\dagger V\gamma^\mu\partial_\mu(V^\dagger)V\psi_L \\
&= g\bar{\psi_L}\gamma^\mu A^a_\mu\tau^a\psi_L + i\bar{\psi_L}\gamma^\mu(\partial_\mu(V^\dagger V) - V^\dagger\partial_\mu(V))\psi_L \\
&= g\bar{\psi_L}\gamma^\mu A^a_\mu\tau^a\psi_L - i\bar{\psi_L}V^\dagger\gamma^\mu\partial_\mu(V)\psi_L
\end{aligned}
\tag{2.2}
$$

but the change in the interaction term is precisely opposite of the change in the fermion kinetic term, so the sum of the two is invariant. In this way, imposing gauge symmetries on the Lagrangian implies the existence of one spin-1 boson for each generator of the symmetry.

So far, the parameter m appearing in the Lagrangian has been interpreted as the physical mass of a fermion while g gives the coupling strength for a particular force. Assuming the coupling is small, cross sections for scattering processes can be calculated using a perturbation series in g. This expansion can be visualized in terms of Feynman diagrams. As an example, consider for the electromagnetic force the process $e^+e^- \rightarrow \mu^+\mu^-$. In this case, g is equal the electron charge e. Figure 2.1 shows two diagrams for $e^+e^- \rightarrow \mu^+\mu^-$, one leading order diagram which has a contribution to the cross section of order e^4 and one diagram at the next order in the expansion, which contributes at order e^8.

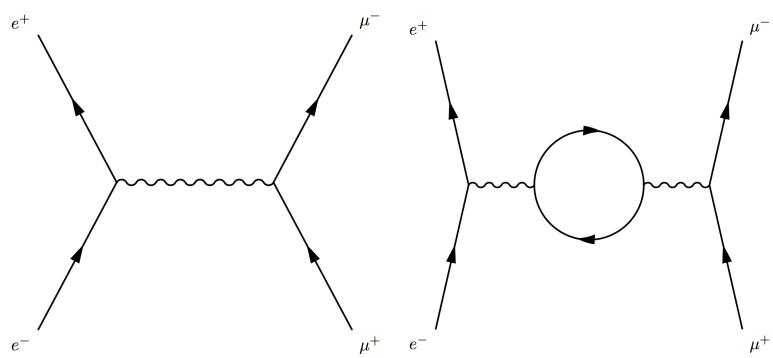

Figure 2.1: Leading-order diagram (left) and an example next-to-leading-order diagram (right) for $e^+e^- \rightarrow \mu^+\mu-$.

When calculating the cross section for this process, we must sum over all possible intermediate states, which includes summing over all possible momenta for the intermediate particles. For the leading-order diagram, there is only one term in the sum as the momentum of the gauge boson is fixed by momentum conservation. When including next-to-leading-order diagrams, we run into a complication. As can be seen in the right-hand side of Figure 2.1, when there is a closed loop, the number of constraints for momentum conservation is fewer than the number of particles in the loop, leaving the momentum of one of them unconstrained. Since we must sum over all possible momenta, this causes the contribution from this diagram to become divergent.

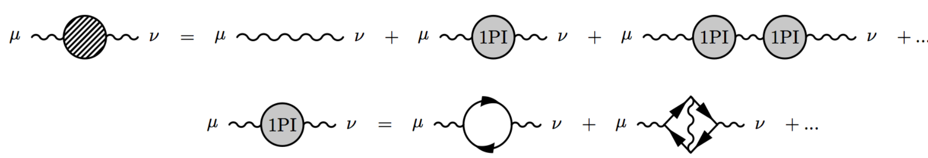

Figure 2.2: Full photon propagator as a perturbation series in the contribution from one-particle-irreducible insertions (top), which sums over all one-particle-insertion diagrams (bottom).

This would seem to be a disaster for the strategy of calculating cross sections using perturbative expansions, but these divergences can be reconciled by absorbing them into the Lagrangian parameters. This process is referred to as renormalization. To give an example of how renormalization works, we consider the two example diagrams of $e^+e^- \to \mu^+\mu-$. The second diagram can be thought of as a correction to the photon propagator. The full propagator containing all corrections can be written as a geometric series the correction from one-particle-irreducible insertions, diagrams that cannot be split in two by breaking a single line. This is illustrated in Figure 2.2. Summing the geometric series gives a correction factor of:

$$\frac{1}{1 - \Pi(q^2)} \tag{2.3}$$

where $(q^2 g^{\mu\nu} - q^\mu q^\nu)\Pi(q^2)$ is the contribution of one-particle-irreducible insertions. A photon propagator will always be accompanied by e^2, so the factor in Equation 2.3 can be interpreted as an effective electromagnetic coupling. Evaluating this contribution requires a method of regularizing divergent integrals over loop momenta. The most common procedure is dimensional regularization [11] in which the integral is evaluated in $d = 4 - \epsilon$ dimensions. At leading order using dimensional regularization, $\Pi(q^2)$ is given by:

$$\Pi(q^2) = \frac{e^2}{2\pi^2}\int_0^1 dx x(1-x)(\frac{2}{\epsilon} - log(m_e^2 - x(1-x)q^2) - \gamma) \tag{2.4}$$

where $\gamma \approx 0.5772$ is the Euler-Mascheroni constant. This contains a divergent piece that is independent of q^2. This can be eliminated by rescaling the coupling e that appears in the Lagrangian so that:

$$e^2 = \frac{e_0^2}{1 - \Pi(\mu^2)} \tag{2.5}$$

where e_0 is now the parameter appearing in the Lagrangian, which is now distinct from the physical coupling e, and μ^2 is the renormalization scale, the particular value of q^2 at which the coupling is rescaled. The effective coupling can now be written as:

$$e_{eff}^2 = \frac{e^2}{1 - (\Pi(q^2) - \Pi(\mu^2))} \tag{2.6}$$

The choice of renormalization scale is an arbitrary one on which physical observables should have no dependence. In practice, the truncation of the perturbation series causes some scale dependence to remain. The degree to which a prediction depends on the renormalization scale is frequently used to provide an estimate of the size of higher-order corrections [74].

Notice that the effective coupling depends on the energy scale of the interaction. This running of the coupling has important consequences for physics at the LHC. The effective coupling for the strong force increases with decreasing energy so that that coupling becomes $\mathcal{O}(1)$ at an energy scale of ∼1 GeV. This leads to a phenomenon known as "confinement" for quarks and gluons. As two colored particles move apart, it becomes energetically favorable to produce a new $q\bar{q}$ pair from the vacuum. As a result, only colorless combinations of these particles are able to propagate freely. Quarks and gluons are therefore confined to these colorless combinations, called hadrons. As the energy scale increases to hundreds of GeV, the effective coupling decreases to $\mathcal{O}(0.1)$. This frees quarks and gluons at this energy from their confinement to hadrons. This is known as "asymptotic freedom." The running of the strong coupling has been confirmed experimentally as shown in Figure 2.3, where $\alpha_s = \frac{g_s^2}{4\pi}$.

Both asymptotic freedom and confinement are important at the LHC. Protons are collided at very high energies, where the quarks and gluons are asymptotically free. A quark or gluon scattered away from the interaction point will begin to radiate, creating more gluons and $q\bar{q}$ pairs with lower energy until they reach the scale of confinement and become grouped into hadrons. This shower of hadrons, collimated in the direction of the original quark/gluon, is what is reconstructed in the detector and is termed a "jet." In order to make predictions, it is important to have a good understanding of both the initial hard scatter and jet formation. The former can be treated perturbatively while the latter is done with parton shower models, which handle the radiation of particles from an outgoing quark/gluon one at time, starting with the widest-angle or highest-transverse-momentum radiation. The ability to treat the short-distance physics (the hard scatter) and long-distance physics (the parton shower) independently is called factorization. The energy scale at which the switch is made from perturbative treatment to parton showering is called the factorization scale.

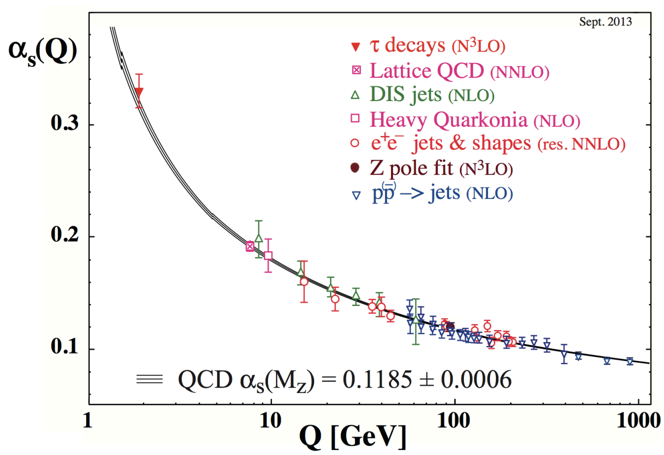

Figure 2.3: Measurements of the strong coupling α_s at energies ranging from $\sim$2 GeV almost up to 1 TeV [8].

The electroweak couplings are much weaker than the strong coupling, so electroweak interaction does not pose the same calculational difficulties at low energies, and unlike for strong interactions, the effective coupling increases with energy. But the electroweak symmetry presents a new challenge: it must be broken in order to explain why particles have mass. To begin with, the bosons of unbroken gauge theories must be massless because the addition of a mass term for the boson would violate gauge invariance. This is easiest to see using the infinitesimal transformation law for the vector fields, $A^a_\mu \rightarrow A^a_\mu + \frac{1}{g}\partial_\mu \alpha^a + f^{abc} A^b_\mu \alpha^c$, where the structure constant f^{abc} is defined by $[\tau^a, \tau^b] = if^{abc}\tau^c$.

$$\begin{aligned}\frac{1}{2}m^2 A^a_\mu A^{\mu a} \to \frac{1}{2}m^2(A^a_\mu + \frac{1}{g}\partial_\mu \alpha^a + f^{abc}A^b_\mu \alpha^c)(A^{\mu a} + \frac{1}{g}\partial^\mu \alpha^a + f^{aij}A^{\mu i}\alpha^j) \\ = \frac{1}{2}m^2(A^a_\mu A^{\mu a} + 2f^{abc}A^b_\mu \alpha^c A^{\mu a} + \frac{2}{g}A^a_\mu \partial^\mu \alpha^a) + \mathcal{O}(\alpha^2)\end{aligned} \tag{2.7}$$

where we see that an $\mathcal{O}\alpha$ rotation of the fields produces an $\mathcal{O}\alpha$ change to the Lagrangian. This requirement of massless bosons is inconsistent with the observed masses of the W and Z bosons, and the electroweak interaction has a further complication that only left-handed fermions are charged under $SU(2)_L$. Left-handed and right-handed fermions also have different hypercharges. Recall that fermion mass terms are only gauge invariant if the transformations for left-handed and right-handed fermions are the same. So imposing electroweak gauge symmetry requires fermions to be massless as well. In order for the Standard Model to be consistent with the observed masses for fermions and W and Z bosons, a mechanism must be introduced to break $SU(2)_L \otimes U(1)_Y$. And since the photon remains massless, this symmetry breaking mechanism must also leave intact a $U(1)$ symmetry corresponding to electromagnetism.

2.1.2 Electroweak Symmetry Breaking

In the Standard Model, electroweak symmetry is spontaneously broken using the Higgs mechanism. A complex scalar is introduced that has a hypercharge of 1/2 and transforms as a doublet under $SU(2)_L$. Then the following terms are added to the Lagrangian:

$$\Delta\mathcal{L}_{kinetic} = (D_\mu\phi)^\dagger D^\mu \phi \tag{2.8}$$

$$\Delta\mathcal{L}_{potential} = -\mu^2|\phi|^2 + \lambda|\phi|^4 \tag{2.9}$$

where $D_\mu = \partial_\mu - ig\frac{\sigma^a}{2}W^a_\mu - i\frac{g'}{2}B_\mu$. If μ^2 and λ are both positive, then the ground state will have a non-zero vacuum expectation value ("VEV"). Since the potential only depends on the magnitude of ϕ, there are many degenerate vacua, but only one of them can be the vacuum of our universe. By gauge invariance, coordinates can be chosen so that VEV is $\langle\phi\rangle = \frac{1}{\sqrt{2}}\begin{pmatrix} 0 \\ v \end{pmatrix}$, where $v = \sqrt{\mu^2/\lambda}$. The choice of orientation of the VEV breaks the electroweak symmetry, leaving behind the gauge symmetry of electromagnetism. Putting the VEV back into the kinetic term gives mass terms for the gauge bosons.

$$\begin{aligned}\Delta\mathcal{L} &= \langle\phi\rangle(ig\frac{\sigma^a}{2}W^a_\mu + i\frac{g'}{2}B_\mu)(-ig\frac{\sigma^b}{2}W^b_\mu - i\frac{g'}{2}B_\mu)\langle\phi\rangle \\ &= \frac{v^2}{2}(\frac{g^2}{4}W^a_\mu W^{\mu a} + \frac{g'^2}{4}B_\mu B^\mu + \frac{gg'}{2}W^3_\mu B^\mu)\end{aligned} \tag{2.10}$$

The mass matrix the gauge bosons, (W^a_μ, B_μ), is:

$$\frac{v^2}{4}\begin{pmatrix} g^2 & 0 & 0 & 0 \\ 0 & g^2 & 0 & 0 \\ 0 & 0 & g^2 & gg' \\ 0 & 0 & gg' & g'^2 \end{pmatrix} \tag{2.11}$$

which is invariant under rotations of the W^a_μ fields. This remaining global $SU(2)$ symmetry is referred to as "custodial symmetry" [91]. In the absence of hypercharge, this would imply equal masses for all of the weak gauge bosons, but mixing between the W^3_μ and B_μ fields shifts the mass of the neutral weak boson. Diagonalizing the matrix, the mass eigenstates of the gauge fields are

$$W^\pm_\mu = \frac{1}{\sqrt{2}}(W^1_\mu \mp iW^2_\mu),\ m_W = \frac{gv}{2} \tag{2.12}$$

$$Z_\mu = \frac{1}{\sqrt{g^2+g'^2}}(gW^3_\mu - g'B_\mu),\ m_Z = \frac{v}{2}\sqrt{g^2+g'^2} \tag{2.13}$$

$$A_\mu = \frac{1}{\sqrt{g^2+g'^2}}(g'W^3_\mu + gB_\mu),\ m_A = 0 \tag{2.14}$$

giving three massive gauge bosons corresponding to the three broken generators of $SU(2)_L \otimes U(1)_Y$ and one massless boson corresponding to the unbroken $U(1)_{EM}$. The W and Z bosons now have mass, but what about fermions? Masses for the fermions are generated in a similar manner, by introducing terms coupling the Higgs field to matter.

$$\Delta\mathcal{L} = -y_d(\bar{q}_L\dot{\phi})d_R - y_u(\epsilon^{ab}\bar{q}_{La}\phi^\dagger_b)u_R + h.c. \tag{2.15}$$

where $q_L = \begin{pmatrix} u_L \\ d_L \end{pmatrix}$. The $SU(2)_L$ indices of ϕ and q_L are contracted and, the hypercharges sum to zero (e.g. $-Y^{q_L} + Y^\phi + Y^{d_R} = -\frac{1}{6} + \frac{1}{2} - \frac{1}{3} = 0$), avoiding both problems that prevented the inclusion of $\bar{q_L} d_R$ and similar terms. Once again, mass terms arise from the non-zero Higgs VEV.

$$\begin{aligned}\Delta\mathcal{L} &= -y_d(\bar{q}_L \cdot \langle\phi\rangle)d_R - y_u(\epsilon^{ab}\bar{q}_{La}\langle\phi\rangle_b^\dagger)u_R + h.c.\\ &= -\frac{1}{\sqrt{2}}y_d(\left(\begin{array}{c}\bar{u}_L\\ \bar{d}_L\end{array}\right)\cdot\left(\begin{array}{c}0\\ v\end{array}\right))d_R - \frac{1}{\sqrt{2}}y_u(\epsilon^{ab}\left(\begin{array}{c}\bar{u}_L\\ \bar{d}_L\end{array}\right)_a\left(\begin{array}{c}0\\ v\end{array}\right)_b)u_R + h.c.\\ &= -y_d\frac{v}{\sqrt{2}}\bar{d}_L d_R - y_u\frac{v}{\sqrt{2}}\bar{u}_L u_R + h.c.\end{aligned} \tag{2.16}$$

So far we have recovered the particle masses we needed by inserting the VEV for the Higgs field. A natural question to ask is whether the addition of this new field leads to any new phenomena that we can observe. Expanding around the minimum of the Higgs potential, we have $\phi = \left(\begin{array}{c} w^1(x) + iw^2(x)\\ v + h(x) + iw^3(x)\end{array}\right)$. Inserting this into the potential, we get:

$$\begin{aligned}\Delta\mathcal{L}_{potential} &= \frac{-\mu^2}{2}[(v+h)^2 + w^a w^a] + \frac{\lambda}{4}[(v+h)^2 + w^a w^a]^2\\ &= (\lambda v^3 - \mu^2 v)h + \frac{1}{2}(3\lambda v^2 - \mu^2)h^2 + \frac{1}{2}(\lambda v^2 - \mu^2)w^a w^a\\ &+ \lambda v(h^3 + h w^a w^a) + \frac{\lambda}{4}(h^4 + 2h^2 w^a w^a)\\ &= \frac{1}{2}(2\lambda v^2)h^2 + \lambda v(h^3 + h w^a w^a) + \frac{\lambda}{4}(h^4 + 2h^2 w^a w^a)\end{aligned} \tag{2.17}$$

The mass terms for the w^a fields vanish while the remaining field acquires a mass of $m_h = \sqrt{2\lambda v^2}$. The three massless fields are not independent physical particles but are "eaten" to become the longitudinal polarizations of the W and Z bosons. The massive scalar field that remains is referred to as the Higgs boson. In another triumph for the Standard Model, a new particle with a mass of 125 GeV and properties consistent with the Higgs boson was discovered by the ATLAS and CMS collaborations at the LHC in 2012 [9, 10]. Going back to Equations 2.10 and 2.16 and substituting $v + h$ for v, we see that the couplings of the Higgs boson to vector bosons and fermions are:

$$\begin{aligned}\Delta\mathcal{L}_{boson} &= \frac{(v+h)^2}{2}(\frac{g^2}{4}W^a_\mu W^{\mu a} + \frac{g'^2}{4}B_\mu B^\mu + \frac{gg'}{2}W^3_\mu B^\mu) \\ &= \frac{(v+h)^2}{2}(\frac{g^2}{2}W^+_\mu W^{-\mu} + \frac{g^2+g'^2}{4}Z_\mu Z^\mu) \\ &\supset \frac{2m_W^2}{v}hW^+_\mu W^{-\mu} + \frac{m_Z^2}{v}hZ_\mu Z^\mu + \frac{m_W^2}{v^2}h^2 W^+_\mu W^{-\mu} + \frac{m_Z^2}{2v^2}h^2 Z_\mu Z^\mu\end{aligned} \tag{2.18}$$

$$\begin{aligned}\Delta\mathcal{L}_{fermion} &= -y_f\frac{v+h}{\sqrt{2}}\bar{f}_L f_R + h.c. \\ &\supset -\frac{m_f}{v}h\bar{f}_L f_R + h.c.\end{aligned} \tag{2.19}$$

where f runs over all fermions. The coupling of the Higgs boson to other Standard Model particles is proportional particle's mass. We therefore expect the inclusion of the Higgs boson to have the largest effects on processes involving heavy vector bosons or top quarks.

A quick aside on Mandelstam variables, three quantities that are defined for 2→2 scattering processes as follows:

$$\begin{aligned} s &= (p_i + k_i)^2 = (p_f + k_f)^2 \\ t &= (p_f - p_i)^2 = (k_f - k_i)^2 \\ u &= (k_f - p_i)^2 = (p_f - k_i)^2 \end{aligned} \tag{2.20}$$

where p_i and k_i are the momenta of the initial state particles and p_i and k_i are the momenta of the final state particles. Amplitudes are often expressed in terms of these variables in order to ease the use crossing symmetry, the equivalence between having a particle with momentum p in the initial state and having its antiparticle with momentum $-p$ in the final state, in determining the amplitudes for two similar processes without going through both calculations. For diagrams in which a single virtual particle with momentum q is exchanged, q^2 will be equal to one of the Mandelstam variables. It is common to refer to such diagrams as belonging to the $s/t/u$-channel, a convention I will adopt in a moment.

The Higgs boson plays a very important role in vector boson scattering (VBS). The non-Abelian nature of the electroweak gauge symmetry gives rise to interactions among the corresponding gauge bosons, allowing them to scatter off each other. The three leading-order diagrams for $W^{\pm}W^{\pm}$ scattering, not involving the Higgs boson, are shown in Figure 2.4. If these were the only contributions, the scattering of longitudinally-polarized vector bosons would present a problem at high energies. Expressions for the amplitude of these diagrams can be written using the Feynman rules for electroweak diagrams:

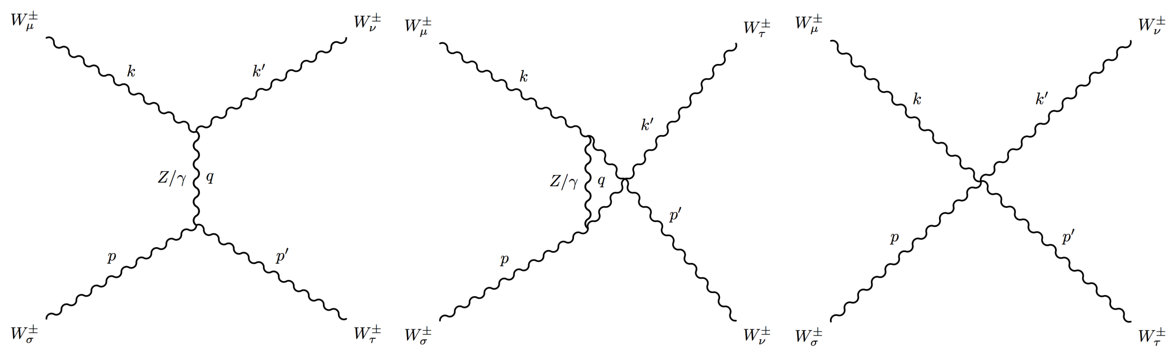

Figure 2.4: Leading order diagrams for $W^{\pm}W^{\pm}$ scattering involving triple gauge couplings in the t-channel (left) and u-channel (middle) and quartic gauge couplings (right).

$$\begin{aligned}
&t-\text{channel diagram:}\\
i\mathcal{M} = {}& i\hat{\epsilon}_{\mu}(k)\hat{\epsilon}^{*}_{\nu}(k')[g^{\mu\nu}(k-k')^{\rho} - g^{\mu\rho}(q+k)^{\nu} + g^{\rho\nu}(q+k')^{\mu}] \times \\
&(\frac{g^2 c_W^2}{q^2 - m_Z^2} + \frac{g^2 s_W^2}{q^2})g_{\lambda\rho} \times \\
&[g^{\sigma\tau}(p-p')^{\lambda} - g^{\sigma\lambda}(q+p)^{\tau} + g^{\lambda\tau}(q+p')^{\sigma}]\hat{\epsilon}_{\sigma}(p)\hat{\epsilon}^{*}_{\tau}(p')
\end{aligned} \tag{2.21}$$

$$\begin{aligned}
&u-\text{channel diagram:}\\
i\mathcal{M} = {}& i\hat{\epsilon}_{\mu}(k)\hat{\epsilon}^{*}_{\nu}(p')[g^{\mu\nu}(k-p')^{\rho} - g^{\mu\rho}(q+k)^{\nu} + g^{\rho\nu}(q+p')^{\mu}] \times \\
&(\frac{g^2 c_W^2}{q^2 - m_Z^2} + \frac{g^2 s_W^2}{q^2})g_{\lambda\rho} \times \\
&[g^{\sigma\tau}(p-k')^{\lambda} - g^{\sigma\lambda}(q+p)^{\tau} + g^{\lambda\tau}(q+k')^{\sigma}]\hat{\epsilon}_{\sigma}(p)\hat{\epsilon}^{*}_{\tau}(k')
\end{aligned} \tag{2.22}$$

$$\begin{aligned}
&\text{quartic coupling diagram:}\\
i\mathcal{M} = {}& ig^2\hat{\epsilon}_{\mu}(k)\hat{\epsilon}^{*}_{\nu}(k')\hat{\epsilon}_{\sigma}(p)\hat{\epsilon}^{*}_{\tau}(p')(2g^{\mu\nu}g^{\sigma\tau} - g^{\mu\sigma}g^{\nu\tau} - g^{\mu\tau}g^{\nu\sigma})
\end{aligned} \tag{2.23}$$

where $\{\epsilon\}$ are the polarization vectors of the W bosons, $\{p, k\}$ are their momenta, and c_W and s_W are the cosine and sine of the weak mixing angle, defined in terms of the weak and hypercharge couplings by $s_W = \frac{g'}{\sqrt{g^2+g'^2}}$. Now let us consider the case when the W bosons are longitudinally polarized. For a boson with momentum $k_\mu = (E_k, 0, 0, k)$ the longitudinal polarization vector is given by $\hat{\epsilon}_\mu = (\frac{k}{m}, 0, 0, \frac{E_k}{m})$. In the limit that the momentum is much larger than the mass of the particle, this polarization vector becomes proportional to the momentum.

$$\begin{aligned}\hat{\epsilon}_\mu &= (\frac{k}{m}, 0, 0, \frac{E_k}{m}) \\ &= \frac{1}{m}(E_k\sqrt{1-\frac{m^2}{E_k^2}}, 0, 0, k\sqrt{1+\frac{m^2}{k^2}}) \\ &= \frac{k^\mu}{m} + \mathcal{O}(\frac{m}{E_k})\end{aligned} \tag{2.24}$$

Substituting the large momentum limit for the longitudinal polarization vectors into the expressions for the scattering amplitudes, we can see that, to leading order in $\frac{s}{m_W^2}$, each diagram has a contribution of order $\frac{s^2}{m_W^4}$. When summing over the diagrams, these contributions cancel, but the terms of order $\frac{s}{m_W^2}$ do not. For a $2 \to 2$ scattering process with particles of equal masses, the cross section in the center-of-mass frame can be written as:

$$\sigma = \frac{1}{32\pi^2 s}\int d\Omega\sqrt{1-\frac{4m^2}{s}}|\mathcal{M}|^2 \tag{2.25}$$

Here we see that if the amplitude is proportional to $\frac{s}{m_W^2}$, the cross section will also be proportional to $\frac{s}{m_W^4}$. The indefinite growth of the cross section with energy will eventually violate unitarity, meaning that the predicted probability for vector boson scattering in pp collisions will exceed unity. For vector boson scattering, this occurs at energies near 1 TeV [3–5].

In the Standard Model, VBS can also proceed through the exchange of a Higgs boson, as shown in Figure 2.5. The contributions from Higgs exchange are:

$$\begin{aligned}&t-\text{channel diagram:} \\ i\mathcal{M} = &-ig^2 m_W^2 \frac{\hat{\epsilon}_\mu(k)\hat{\epsilon}^*_\nu(k')g^{\mu\nu}g^{\sigma\tau}\hat{\epsilon}_\sigma(p)\hat{\epsilon}^*_\tau(p')}{q^2-m_h^2}\end{aligned} \tag{2.26}$$

$$u\text{-channel diagram}:$$
$$i\mathcal{M} = -ig^2 m_W^2 \frac{\hat{\epsilon}_\mu(k)\hat{\epsilon}^*_\nu(p')g^{\mu\nu}g^{\sigma\tau}\hat{\epsilon}_\sigma(p)\hat{\epsilon}^*_\tau(k')}{q^2 - m_h^2} \tag{2.27}$$

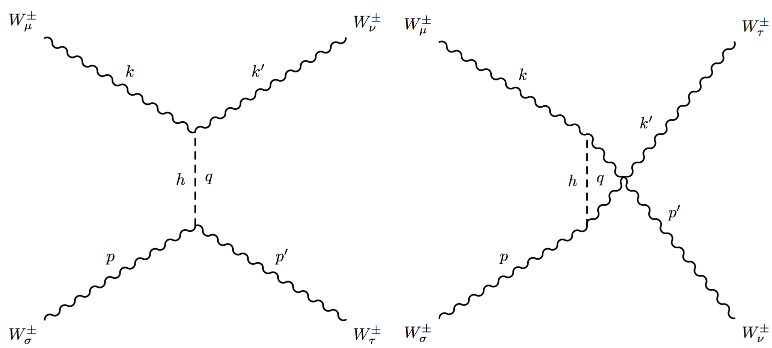

Figure 2.5: Vector boson scattering diagrams with Higgs exchange in the t-channel (left) and u-channel (right).

Putting in the longitudinal polarization vectors, we get the amplitude of these diagrams to go as $\frac{s}{m_W^2}$, but with the opposite sign. The contribution from these diagrams exactly cancels the $\frac{s}{m_W^2}$ contribution from the diagrams involving only the gauge bosons. The combined amplitude asymptotes to a constant as s increases, leading to a cross section that decreases with energy, thereby preserving unitarity.

2.2 $W^\pm W^\pm jj$ Production at the LHC

In this dissertation, $W^\pm W^\pm jj$ production is the process chosen for studying electroweak symmetry breaking. The Standard Model description of $W^\pm W^\pm jj$ production is tested by comparing the observed number of events passing some selection criteria to the theoretical prediction. The predicted number of events can be expressed as follows:

$$N = \int \mathcal{L}dt \cdot \sigma \cdot A \cdot \epsilon \tag{2.28}$$

where $\mathcal{L}$ is the luminosity, a measure of the collision rate discussed further in Chapter 3, σ is the cross section for the $W^\pm W^\pm jj$ process, the rate at which $W^\pm W^\pm jj$ production occurs in pp collisions, A is the acceptance, the fraction of $W^\pm W^\pm jj$ events that would pass all selections given a perfectly efficient detector, and ϵ is the efficiency to reconstruct events within the acceptance. The portion of the phase space of the final state particles that pass the selection criteria is referred to as the “fiducial phase space,” and the product $\sigma \cdot A$, which gives the rate to produce events in this phase space, is referred to as the “fiducial cross section.” Luminosity is independent of the physical process under consideration (see Chapter 3), and the efficiency is determined by simulating the interaction of final state particles with the detector. What must be provided by the theoretical calculation is the fiducial cross section for $W^\pm W^\pm jj$ production.

For a given two initial partons, the cross section for $W^\pm W^\pm jj$ production can be computed as follows. Working in the center-of-mass frame and neglecting quark masses, the cross section can be written as:

$$\sigma = \frac{1}{2E_{CM}^2} \int (\prod_f \frac{d^3 p_f}{(2\pi)^3} \frac{1}{2E_f}) |\mathcal{M}(\{p_f\})|^2 (2\pi)^4 \delta^4 (\sum p_f) \tag{2.29}$$

where $\{p_f\}$ and $\{E_f\}$ are the momenta and energy of the final state particles, E_{CM} is the center-of-mass energy of the collision, and $|\mathcal{M}|^2$ is the scattering amplitude for producing final state particles with momenta $\{p_f\}$. All of the information about the interactions in the theory is contained in $\mathcal{M}$, which sums over all diagrams with identical initial and final states as shown in Figure 2.6. The number of diagrams in the sum is infinite, but since both the electroweak and strong couplings are small at LHC energies, a good approximation can be obtained by neglecting terms that have higher powers of the couplings. The predictions used for this measurement truncate the sum at leading order in the electroweak coupling and next-to-leading order in the strong coupling.

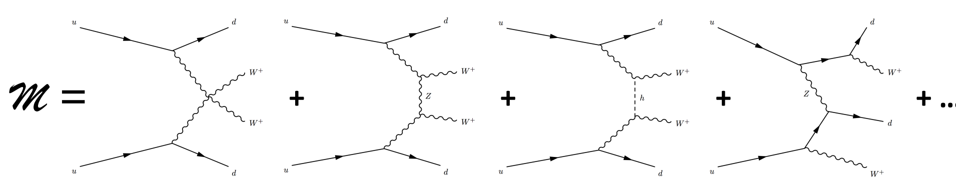

Figure 2.6: A few leading order diagrams for electroweak $W^\pm W^\pm jj$ production.

The $W^\pm W^\pm jj$ process can be split into electroweak production, which contains diagrams of order α_{EW}^4 in the coupling strengths, and strong production, which contains diagrams of order $\alpha_{EW}^2 \alpha_s^2$. Representative diagrams for both are shown in Figure 1.2. In both cases, the incoming quarks scatter off of each other through the exchange of vector bosons. The color connection forged between the quarks in the strong production mechanism pulls them closer together, causing them to scatter at large angles with respect to the beam direction. But for electroweak production, there is no color flow, and the quarks scatter at smaller angles. This difference between the production mechanisms provides a powerful tool for separating the two using kinematic selections.

The particles being collided at the LHC are not quarks but protons containing a mixture of quarks and gluons. Translating cross sections for qq initial states into a cross section for a pp initial state is done using parton distribution functions (PDFs). The PDF for a parton gives the probability density to find that parton carrying a particular fraction of the proton's momentum. PDFs also depend on the energy of the collision. Let $f_i(x, Q^2)$ and $f_j(y, Q^2)$ be the proton PDFs for partons i and j, where x/y denote the fraction of the proton's momentum the each parton is carrying and Q is the collision energy. In the case of two partons colliding at the LHC, $Q = (x + y)E_{beam}$, where E_{beam} is the energy of each proton beam. The expression for the cross section in Equation 2.29 depends on the identities and center-of-mass energy of the two partons: $\sigma = \sigma_{ij}((x + y)E_{beam})$. In order to translate this into a cross section for the pp center-of-mass energy, the cross section must be weighted by the probability of picking out in a given collision partons i and j carrying fractions x and y of the momenta of the two protons, and we must sum over all possible combinations of i, j, x, and y. Then the cross section for pp collisions is given by:

$$\sigma_p p = \sum_{\langle ij \rangle} \int_0^1 \int_0^1 dx dy f_i(x, ((x+y)E_{beam})^2) f_j(y, ((x+y)E_{beam})^2) \sigma_{ij}((x+y)E_{beam}) \tag{2.30}$$

Figure 2.7 shows two examples of PDFs at different energies. The PDFs used in this analysis are estimated using fits to deep inelastic scattering data from the HERA $e^{\pm}p$ collider and data on single-inclusive jet production, Z rapidity distributions, and asymmetry in the rapidity distribution of the charged lepton in $W \to \ell\nu$ events from the Tevatron $p\bar{p}$ collider [12]. Systematic uncertainties on the fitted parameters are provided in the form of alternate PDFs that correspond to one-dimensional 90% confidence level limits. There are 26 free parameters in the fit, and positive and negative variations along a given direction in the parameter space are allowed to be asymmetric, so the total PDF set (central value + systematic variations) contains 53 functions.

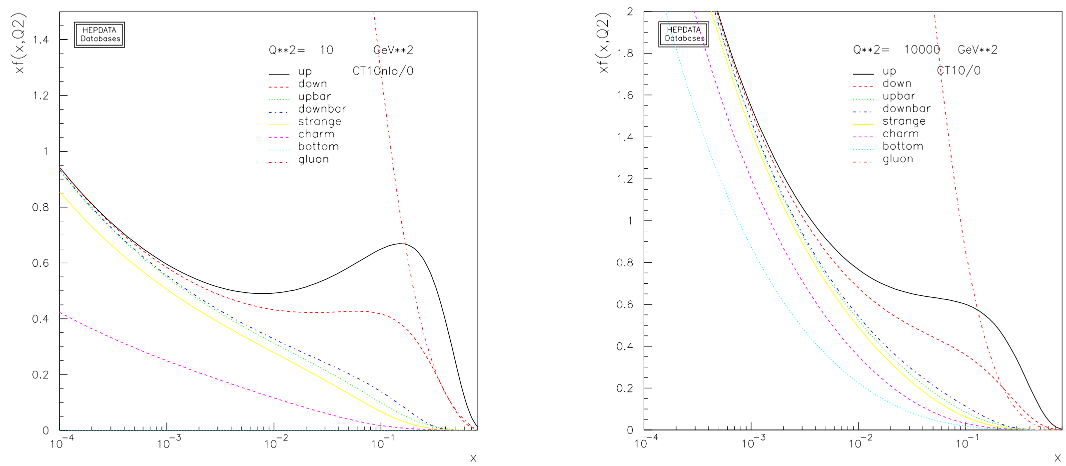

Figure 2.7: CT10 parton distribution functions for $\mathrm{Q}^2 = 10$ GeV^2 and $\mathrm{Q}^2 = 10000$ GeV^2 [13].

The production of two W boson with the same charge requires an initial state with two quarks whose charges must be either both positive or both negative. As can be seen from Figure 2.7, the dominant contribution to W^+W^+ production at the LHC comes from the uu initial state while W^-W^- is most often produced in collisions between two down quarks. If approximate the proton as just consisting of the three valence quarks (uud) each carrying an equal fraction of the proton's momentum, a simple counting of the possible combinations predicts that the cross section for W^+W^+ production will be four times higher for W^-W^- production. This is not far off from the prediction obtained using the full set of PDFs, which produces a W^+W^+/W^-W^- ratio of 3.3.

2.3 Anomalous Quartic Gauge Couplings

The discovery of a Higgs boson at the LHC marks an important milestone in our understanding of electroweak symmetry breaking, but it does not necessarily represent the finish line. Precise measurements of the couplings of the Higgs to other particles may reveal differences with the Standard Model expectation. This would require some new physics to explain the values of the W and Z masses and to help regulate the scattering of longitudinally-polarized vector bosons. In lieu of a specific theory, the effects of new physics on VBS can be parameterized as anomalous couplings among the gauge bosons.

2.3.1 Effective Field Theory

The effective field theory approach assumes that the Standard Model is the correct low-energy theory of nature and estimates the effects of new physics present at high energies using higher dimensional operators constructed from the Standard Model fields. An example of a successful effective field theory is the Fermi theory for weak interactions. Since the action $S = \int \mathcal{L} d^4x$ is a dimensionless quantity, terms in the Lagrangian must dimensions of $(\text{mass})^4$. The mass dimensions of the various fields can then be easily determined from the mass terms in the Lagrangian: fermions have dimension-$\frac{3}{2}$ while scalars and vector bosons are both dimension-1. When adding higher dimensional operators to the Lagrangian, the coefficients of these operators acquire dimensions of inverse mass and can be written as $\frac{c}{\Lambda^{d-4}}$, where c is a dimensionless coupling, Λ is the energy scale of new physics, and d is the dimension of the operator, determined from the combination of fields and derivatives. Since these operators are suppressed by the energy scale Λ, the Standard Model is recovered in the limit that the collision energy goes to zero. Another important feature to note is that higher-dimension operators are suppressed by greater powers of Λ, so operators of higher dimension than the ones under consideration can be safely neglected.

The lowest dimension operators that contribute to aTGCs and aQGCs have dimension six and are listed in Ref. [36]. For operators that give aQGCs without aTGCs, the lowest dimension is dimension eight [35]. The simplest dimension-8 operators that give rise to aQGCs are:

$$\mathcal{L}_{S,0} = \frac{f_{S,0}}{\Lambda^4} \left[(D_\mu \phi)^\dagger D_\nu \phi \right]^2 \tag{2.31}$$

$$\mathcal{L}_{S,1} = \frac{f_{S,1}}{\Lambda^4} \left[(D_\mu \phi)^\dagger D^\mu \phi \right]^2 \tag{2.32}$$

While there is no general conversion between these parameters and the α parameters of the electroweak chiral Lagrangian, they are related for a given vertex by a simple linear transformation [36]. The relationship for the $WWWW$ vertex is:

$$\frac{f_{S,0}}{\Lambda^4}\frac{v^4}{8} = \alpha_4 \tag{2.33}$$

$$\frac{f_{S,1}}{\Lambda^4}\frac{v^4}{8} = \alpha_4 + 2\alpha_5 \tag{2.34}$$

2.3.2 The Electroweak Chiral Lagrangian

The electroweak chiral Lagrangian [14] offers a more general description of electroweak symmetry breaking that starts with only the three scalar degrees of freedom that get cannibalized to become the longitudinal polarizations of the W and Z. Instead of a scalar doublet, a $SU(2)$ matrix is introduced: $\Sigma(x) = e^{\frac{-i}{2v}\sigma^a w^a(x)}$, where v is the symmetry breaking scale. Since this is a unitary matrix, the potential $V(\Sigma^\dagger\Sigma)$ is a constant, leaving terms constructed from derivatives of the Σ fields as the only non-trivial ones that can be added to the Lagrangian. In order for these new terms to be Lorentz-invariant, they must have an even number of derivatives. Σ is dimensionless, so the lowest-order operators, which contain two derivatives will be dimension 2. Therefore, the coefficients of these operators must have dimensions of Λ^2. The two possible dimension-2 operators that can be constructed are $\mathcal{L}_0 = \frac{v^2}{4}Tr\left[(D_\mu\Sigma)^\dagger D^\mu\Sigma\right]$ and $\mathcal{L}_1' = \beta_1 g^2\frac{v^2}{4}Tr\left[(D_\mu\Sigma)\frac{\sigma^3}{2}\Sigma^\dagger\right]^2$. $\mathcal{L}_1'$ violates custodial symmetry and would cause a deviation from $\rho = \frac{m_W}{m_Z c_W} = 1$. Since ρ has been measured to be unity to within 0.05% [8], this operator is strongly constrained. By expanding Σ around $w^a = 0$ we can see that the term $\mathcal{L}_0$ gives rise to mass terms for the gauge bosons.

$$\begin{aligned}
\mathcal{L}_0 &= \frac{v^2}{4}Tr\left[(D_\mu(1+\mathcal{O}(w)))^\dagger D^\mu(1+\mathcal{O}(w))\right] \\
&= \frac{v^2}{4}Tr\left[(ig\frac{\sigma^a}{2}W_\mu^a + i\frac{g'}{2}B_\mu)(-ig\frac{\sigma^b}{2}W_\mu^b - i\frac{g'}{2}B_\mu)\right] + \mathcal{O}(w) \\
&= \frac{v^2}{2}(\frac{g^2}{4}W_\mu^a W^{\mu a} + \frac{g'^2}{4}B_\mu B^\mu + \frac{gg'}{2}W_\mu^3 B^\mu) + \mathcal{O}(w)
\end{aligned} \tag{2.35}$$

which are exactly the same mass terms we got in Section 2.1.2. This framework is clearly desirable for a theory without a light Higgs, but it is still useful for parameterizing anomalous couplings in theories including a Higgs. A scalar resonance can be added to include the observed Higgs boson. As in the previous section, in order to generate anomalous gauge couplings, we only have to continue to add higher-dimension operators. There are several other operators of dimension 4 that give rise to anomalous triple and quartic gauge couplings (aTGCs and aQGCs). These are listed in Ref. [14]. Several limits exist on the possible size of aTGCs [15–30] and a few on aQGCs [31–34]. This measurement of $W^{\pm}W^{\pm}jj$ production is used to set limits on two dimension 4 operators, $\mathcal{L}_4$ and $\mathcal{L}_5$, which do not contribute to aTGCs but do contribute to the $WWWW$ coupling. These two terms are:

$$\mathcal{L}_4 = \alpha_4 \left[Tr(V_\mu V_\nu)\right]^2 \quad (2.36)$$

$$\mathcal{L}_5 = \alpha_5 \left[Tr(V_\mu V^\mu)\right]^2 \quad (2.37)$$

where $V_\mu = (D_\mu \Sigma)\Sigma^\dagger$. The first direct limits on the parameters α_4 and α_5 are presented in Chapter 9. While there is no general conversion between these parameters and the $f_{S,i}$ parameters, they are related for a given vertex by a simple linear transformation [36]. The relationship for the $WWWW$ vertex is:

$$\frac{f_{S,0}}{\Lambda^4}\frac{v^4}{8} = \alpha_4 \quad (2.38)$$

$$\frac{f_{S,1}}{\Lambda^4}\frac{v^4}{8} = \alpha_4 + 2\alpha_5 \quad (2.39)$$

2.3.3 Unitarization

In the Standard Model, the unitarity of the scattering of longitudinally polarized vector bosons is preserved by a cancellation between diagrams involving the vector boson self-interactions and diagrams involving the exchange of a Higgs. In effective theories with anomalous gauge couplings, this is no longer the case. This is not indicative of a problem with effective theories as they are only meant to describe the low-energy effects of some new physics. However, it can lead to an overestimation of the sensitivity of experiments to anomalous couplings. In order to prevent this, there are a few commonly used methods for restoring unitarity to effective theories.

One method is the "form factor" method, in which an energy dependence is added to the anomalous coupling so that it falls off after some cutoff scale, Λ. The cutoff scale and functional form of the form factor are arbitrary choices, but the most common choice for anomalous gauge couplings is a dipole form factor [16–23, 32], $1/(1+\frac{s}{\Lambda^2})^2$. The unitarization scheme used in this measurement is the K-matrix method [37]. Unitarity requires that the eigenamplitudes, $a(s)$, for vector boson scattering lie within the Argand circle, $|a(s) - i/2| = 1/2$. The K-matrix method projects scattering amplitudes calculated in the effective theory onto the Argand circle, causing the cross section to saturate at the maximum value allowed by unitarity. This avoids the arbitrary choices involved when applying a form factor. Figure 2.8 shows a comparison of VBS cross sections for a Higgsless Standard Model with and without K-matrix unitarization applied.

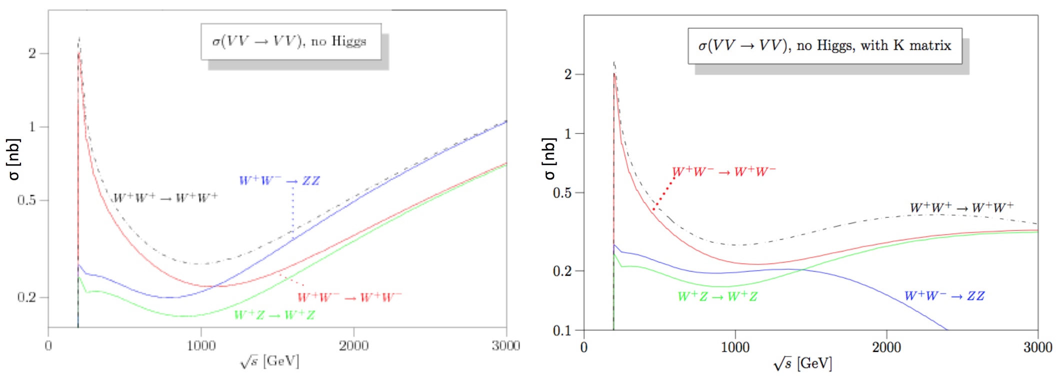

Figure 2.8: Vector boson scattering cross sections (nb) for the Standard Model without a Higgs with (right) and without (left) K-matrix unitarization [37].

2.3.4 Constraints from electroweak precision tests

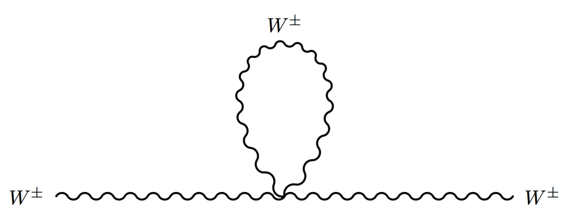

Figure 2.9: Example diagram for one-loop contribution of quartic gauge interactions to the gauge boson self-energies.

If anomalous quartic gauge couplings exist, VBS processes are not the only ones that will be affected. Anomalous quartic couplings will contribute to the self-energies of gauge bosons through the diagram shown in Figure 2.9. Therefore, these couplings also affect the scattering of fermions via exchange of a vector boson. For these processes there is a wealth of data available that can be used to constrain anomalous couplings. The contribution of new physics to the scattering of fermions through its effects on gauge boson propagators is parameterized by the Peskin-Takeuchi parameters, S, T, and U [90]. The measured values of the parameters are given in Ref. [8]:

$$\begin{aligned} S &= -0.03 \pm 0.10 \\ T &= 0.01 \pm 0.12 \\ U &= 0.05 \pm 0.10 \end{aligned} \tag{2.40}$$

in excellent agreement with the Standard Model ($S = T = U = 0$). These have been used to constrain the allowed values of α_4 and α_5 [89]. The α_4 and α_5 parameters to give the following contributions to T:

$$\alpha_{EW} T = \frac{-15\alpha_4}{64\pi^2} g^4 (1 + c_W^2) \frac{s_W^2}{c_W^2} \log \frac{\Lambda^2}{m_Z^2} \tag{2.41}$$

$$\alpha_{EW} T = \frac{-3\alpha_5}{32\pi^2} g^4 (1 + c_W^2) \frac{s_W^2}{c_W^2} \log \frac{\Lambda^2}{m_Z^2} \tag{2.42}$$

where Λ is the energy scale of the new physics responsible for the anomalous couplings. For $\Lambda = 2$ TeV, the resulting 95% confidence level limits on α_4 and α_5 are -0.06 $< \alpha_4 <$ 0.30 and -0.15 $< \alpha_5 <$ 0.76.

Chapter 3

The Large Hadron Collider

The Large Hadron Collider (LHC) [38] is a circular accelerator with a circumference of 26.7 km designed to collide beams of protons with a center-of-mass energy of 14 TeV. It is located near Geneva, Switzerland and reuses the tunnel and injection chain from the Large Electron-Positron (LEP) collider. The layout of the LHC in shown in Figure 3.1. The LHC ring has eight straight sections in which beams can be made to collide, only four of which are used for this purpose. The four experiments at the LHC are built around these interaction points. The straight sections are also used for inserting the proton beams, accelerating them, and dumping them. The capture and acceleration of the beams is done using RF cavities while superconducting magnets are used to bend and focus the beams.

Protons are accelerated by the electric field inside superconducting RF cavities. The frequency of EM waves in these cavities is kept at a harmonic of the revolution frequency so that protons experience the same electric field each time they pass through the cavity. The field in the cavity also keeps protons bunched together since protons that are spread out will see different electric fields and will therefore have different accelerations. Each beam is accelerated by a series of eight 400 MHz RF cavities divided into two cryomodules, a schematic of which is shown in Figure 3.2. Each cavity is powered by its own 300 kW klystron and provides a 2 MV accelerating voltage. With each revolution, the beam energy is increased by 485 keV until reaching the final energy for collisions.

The LHC uses electromagnets made from superconducting NbTi Rutherford cables that are cooled using superfluid helium to a temperature of 1.9 K. Since the LHC is a proton-proton collider, opposite magnetic fields are needed to direct each beam. However, the LEP tunnel was not designed to

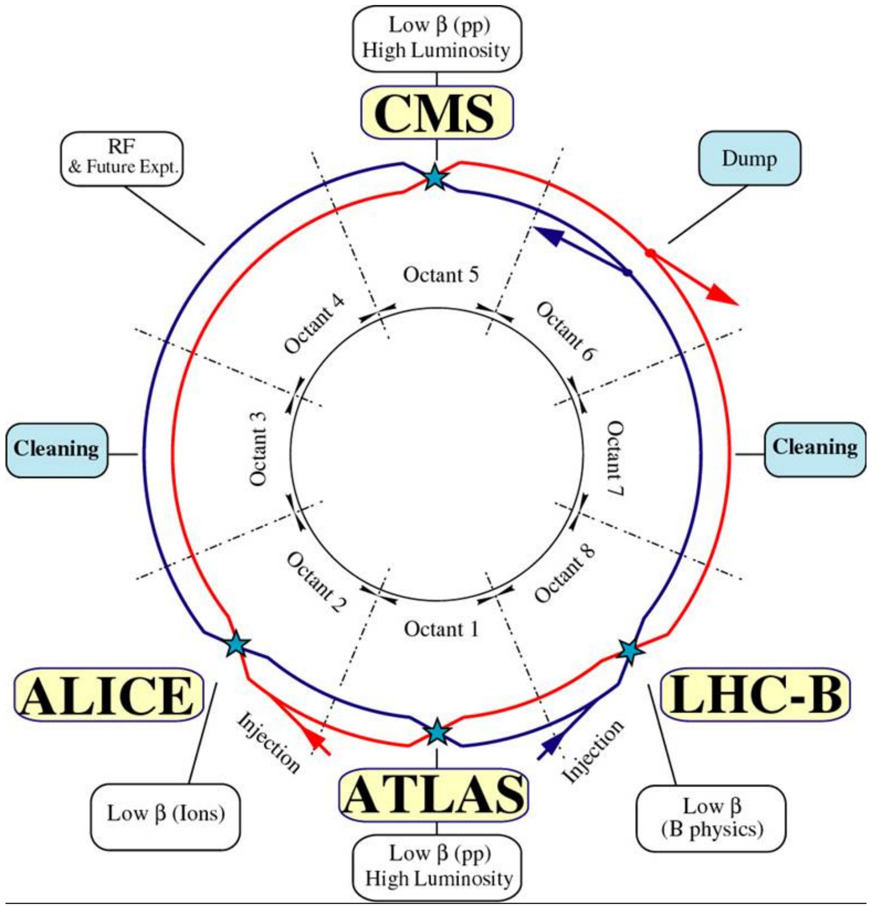

Figure 3.1: Layout of the LHC [38].

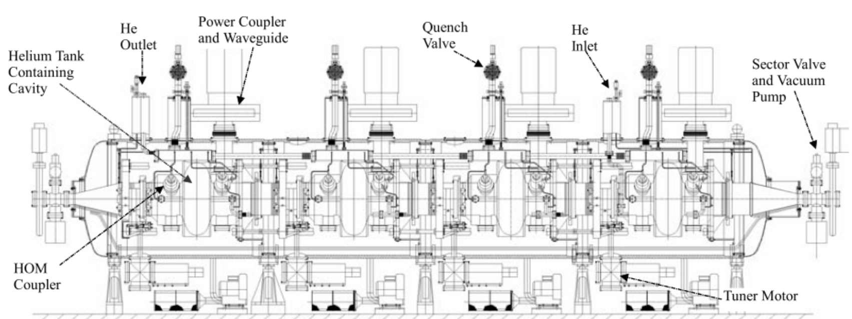

Figure 3.2: Schematic of cryomodule containing four RF cavities [38].

accommodate separate magnet systems for each beam. This led to the adoption of a "two-in-one" design in which the two beamlines share a common cold mass and cryostat.

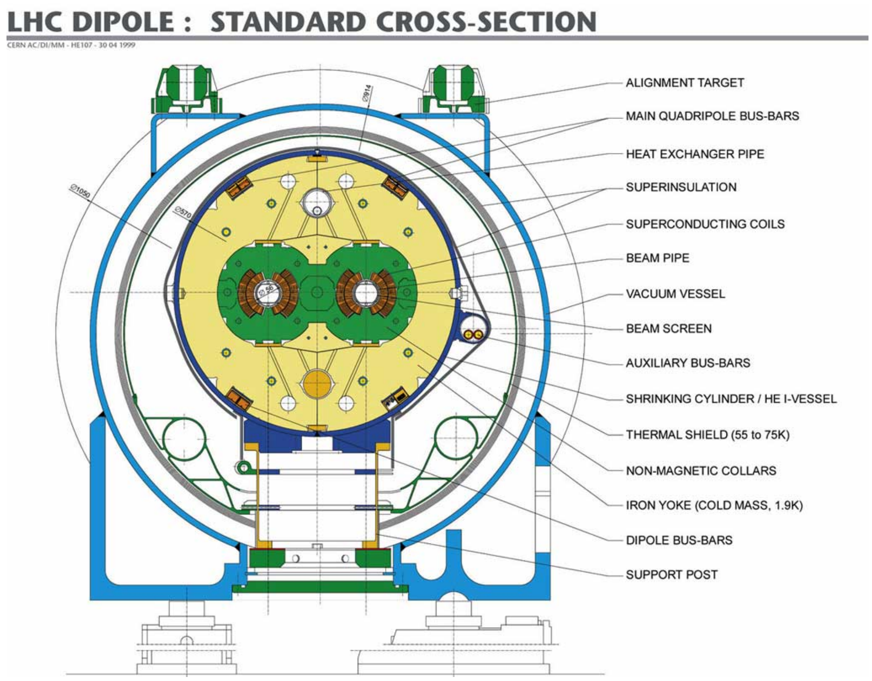

Figure 3.3: Cross section of LHC dipole magnet [39].

The cross section of an LHC dipole magnet is shown in Figure 3.3. 1,232 of these magnets are used to bend the beams and keep them going in a circle. The cables are wound in such a way that the magnetic field is oriented in opposite directions in each beam pipe. At injection, the current through the cables is 763 A, producing a magnetic field of 0.54 T. The maximum beam energy is limited by the peak field of the magnets, which reach 8.33 T at a current of 11850 A. Rigid collars are used to help maintain structural stability since the electromagnetic forces between cables can reach the level of a few MN. In order for the LHC to work properly, each dipole magnet must be nearly identical: relative variation of the field between magnets cannot exceed 10^{-4}.

Focusing of the beam is done using quadrupole magnets. The LHC ring contains 392 main quadrupoles to keep the beam from spreading out as it travels around the ring and several other multipole magnets for making beam corrections. Higher precision quadrupoles are located prior to the collision points and focus the beams down to a transverse size of about 15 μm.

In addition to reaching unprecedented energies, the LHC is also designed to reach unprecedented luminosity. Luminosity is a measure of the rate of proton-proton collisions. Given a cross section for a particular process, the rate at which those events are produced is given by $N = L\sigma$. Luminosity as a function of beam parameters is given by:

$$L = \frac{N_b^2 n_b f \gamma}{4\pi \epsilon_n \beta_*} F \tag{3.1}$$

where N_b is the number of protons per bunch, n_b is the number of colliding bunches, f is the revolution frequency, γ is the relativistic Lorentz factor, ϵ_n is the transverse beam emittance, β_* is the beta function relating emittance to beam width at the interaction point, and F is a geometric factor that accounts for the non-zero crossing angle of the colliding beams. The LHC is designed to circulate beams containing 2808 bunches with a bunch spacing of 25 ns and 1.15×10^{11} protons per bunch at a frequency of 11245 revolutions per second. The design values for transverse emittance and β_* are 3.75 μm and 0.55 m, and the geometric factor is about 1/40. The peak luminosity reach with all the design parameters is 10^{34} cm^{-2}s^{-1}.

3.1 Injection Chain

Protons are produced from hydrogen gas and go through several stages of acceleration before reaching the LHC [41]. The accelerator chain is shown in Figure 3.4. The process begins with hydrogen gas being fed into a duoplasmatron ion source, which ionizes the hydrogen atoms to produce a proton beam. A radio frequency quadrupole is used to accelerate and focus the beam before it is injected into the LINAC2. LINAC2 is a 30-meter long linear accelerator that takes protons from an energy of 750 keV to 50 MeV. After LINAC2, the proton beam passes through a series of circular accelerators, starting with the Proton Synchrotron Booster (PSB). The PSB consists of 4 vertically stacked rings with a circumference of 157 meters and accelerates protons to an energy of 1.4 GeV.

The next stop is the Proton Synchrotron (PS), which is a 628-meter long ring. In addition to raising the beam energy to 25 GeV, the PS establishes the bunch structure used at the LHC. Bunches are split in two stages, once at 1.4 GeV and once at 25 GeV, by raising the RF frequency to higher multiples of the revolution frequency. The beam leaving the PS consists of

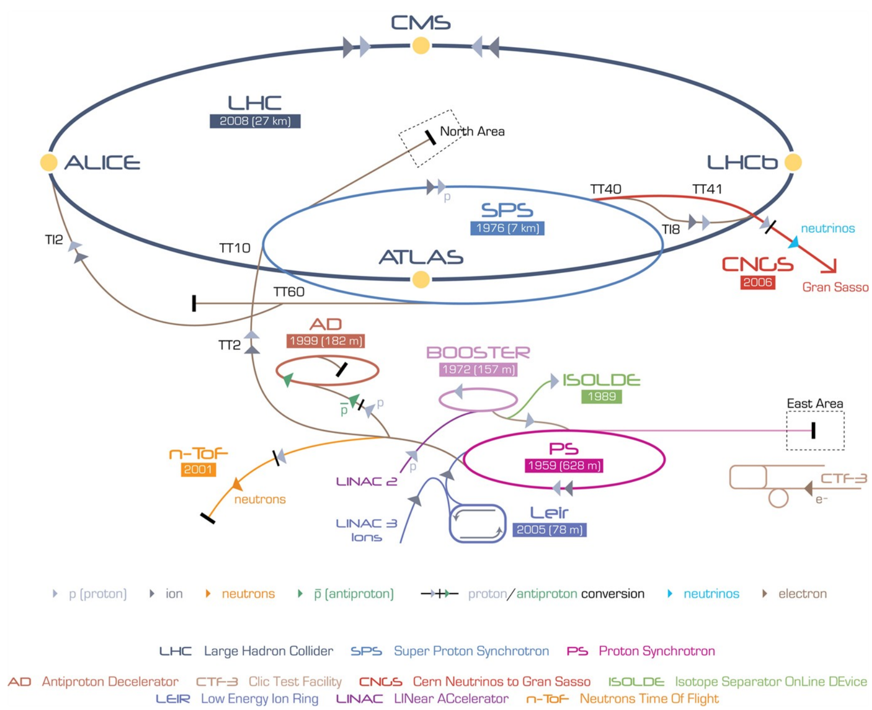

Figure 3.4: Injection chain for the LHC [40].

72 bunches of protons with a duration of about 4 ns and a spacing of 25 ns followed 12 empty bunches. The gap left by the empty bunches provides time for the ejection kicker magnet to ramp up. The final accelerator in the injection chain is the Super Proton Synchrotron (SPS). This 7-km long circular accelerator was used to discover the W and Z bosons in 1983. It takes the 25 GeV beam from the PS up to an energy of 450 GeV. Protons are then injected into the LHC and accelerated to their final energy before being made to collide.

3.2 Run 1 Performance

First collisions at the LHC were delayed by an accident that occurred on September 19, 2008. During powering tests, a quench developed in a region between two magnets, resulting in an electric discharge that ruptured the helium enclosure and damaged magnets and support structures along 700 meters of the tunnel. While the machine was being repaired, other connections between magnets were examined, and the quench detection system was upgraded to include these areas. However, it was decided that further upgrades were necessary before operating the machine at full design energy.

In 2010 and 2011, roughly 5 fb^{-1} of data was taken at half of the design energy ($\sqrt{s} = 7$ TeV). The measurement presented in this dissertation uses the data taken in 2012, which corresponds to 20.3 fb^{-1} of data with a center-of-mass energy of 8 TeV. In addition to running at lower energy, the LHC ran with about half as many bunches and twice the bunch spacing as designed. However, due to higher beam intensity, the peak luminosity reached, $7.7 \times 10^{33}\text{cm}^{-2}\text{s}^{-1}$, was not far below the design luminosity. The 2012 run also benefited from a $\epsilon_n \beta_*$ product of 2.5 μm$\times$ 0.6 m = 1.5 mm^2, which was about 25% lower than the design value [42]. Figure 3.5 shows the integrated luminosity as a function of time in 2012. The downside to having fewer bunches with more protons per bunch is that each bunch crossing produces more collisions, which makes it harder to reconstruct the rare collisions of interest to physicists. In 2012, there were an average of 20 proton-proton collisions per bunch crossing.

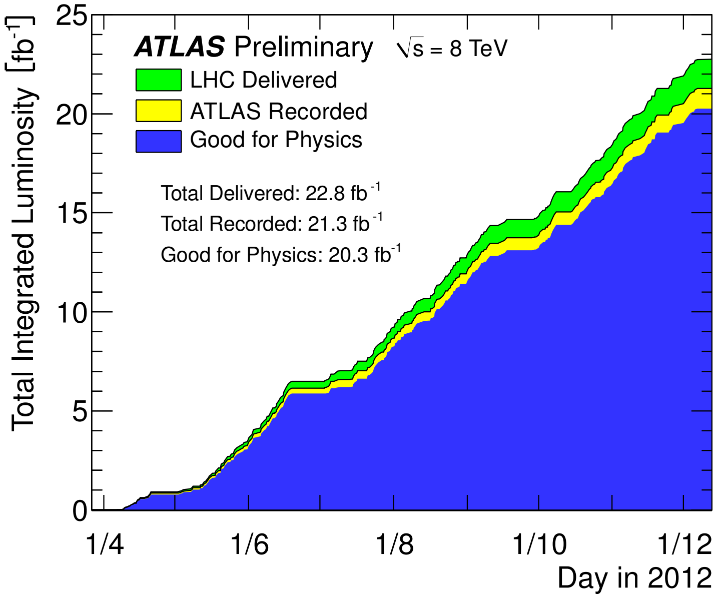

Figure 3.5: Integrated luminosity as a function of time delivered by the LHC and recorded by the ATLAS detector [43].

Chapter 4

The ATLAS Detector

The ATLAS detector, shown in Figure 4.1, has an approximately forward-backward symmetric cylindrical geometry. It consists of a cylindrical barrel region with endcap disks on either side. In both the barrel and the end-cap, the detector is comprised of three systems: the inner detector, the calorimeter, and the muon spectrometer. The inner detector (ID) is used to chart the trajectories of charged particles and measure their momenta. It sits within a solenoid that generates a 2 T magnetic field used to measure momentum in the transverse plane. The calorimeter is positioned outside of the solenoid and is used to measure the energies of both charged and neutral particles. The calorimeter is designed to be thick enough to force electrons, photons, and hadrons to exhaust all of their energy. Outside of the calorimeter sits the muon spectrometer (MS), which is used make a second measurement of muon trajectories. It uses a 0.5-1 T magnetic field produced by toroidal magnets. Details beyond those given in this chapter can be found in Ref. [44].

The coordinate system for the ATLAS detector has its origin at the nominal interaction point, which lies right at the center of the detector. The z-axis points along the beamline in the counterclockwise direction when viewed from above while the x-axis points toward the center of the LHC ring, and the y-axis points upward away from the plane containing the ring. In the plane transverse to the beam direction, radius and azimuthal angle coordinates are defined as $R = \sqrt{x^2 + y^2}$ and $\phi = \arctan \frac{y}{x}$, respectively. The polar angle, θ, is measured from the positive z-axis. When considering the proximity of a particle's trajectory to the beam direction, it is often more convenient to use rapidity, defined as $y = \frac{1}{2} \ln \frac{E+p_z}{E-p_z}$, rather than polar angle because differences in rapidity are independent of boosts along the

z-axis. In the case of a massless particle, the rapidity is related to the polar angle simply by $y = -\ln\tan\frac{\theta}{2}$. This quantity is taken as the definition of pseudorapidity, η, and is the most commonly used coordinate to described location along the z-axis.

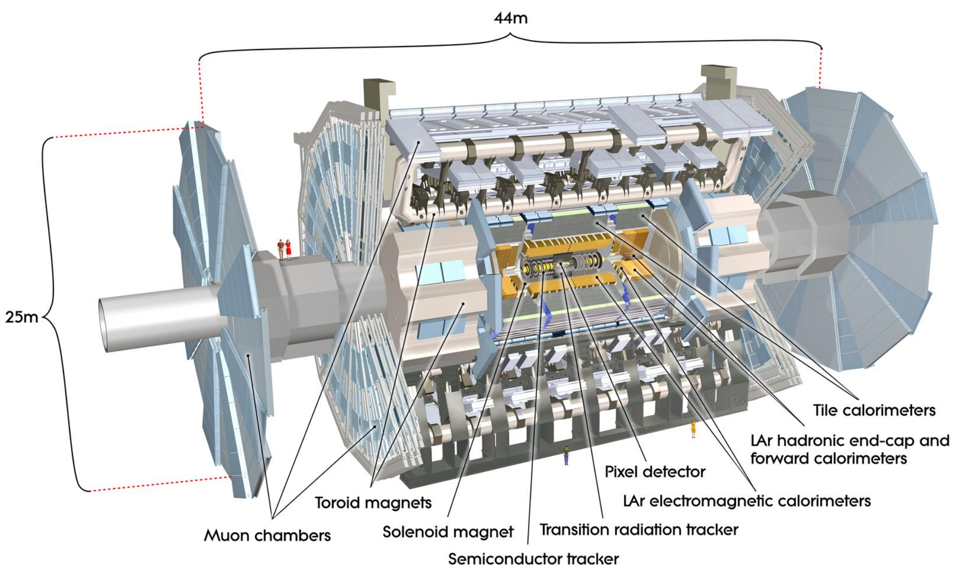

Figure 4.1: Illustration of the ATLAS detector with various subsystems indicated [45].

4.1 Inner Detector

The ID consists of three subsystems, ordered in increasing distance from the beamline and decreasing resolution: the pixel detector, the semi-conductor tracker (SCT), and the transition radiation tracker (TRT). The pixel and SCT systems use doped silicon sensors held under reverse bias to measure the passage of charged particles while the TRT uses drift tubes interleaved with transition radiation material. The three subsystems are depicted in Figure 4.2.

Each system makes multiple measurements of the position of a charged particle, and these measurements are used to fit a trajectory (track) for

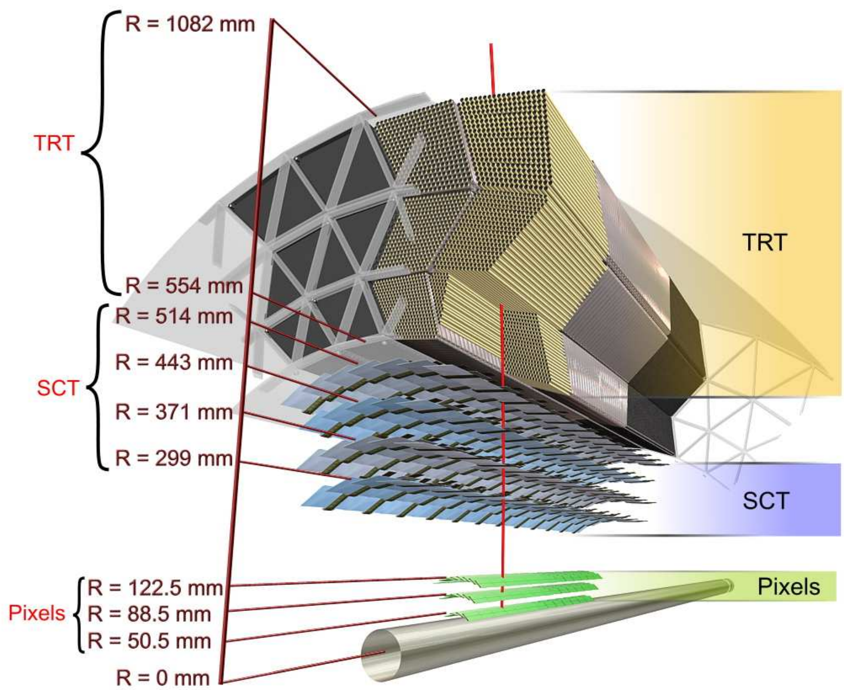

Figure 4.2: View of the barrel region of the ATLAS Inner Detector [44].

the particle as described in Chapter 5. The entire ID sits inside a solenoid that produces a 2T magnetic field oriented along the beamline. As a result, charged particles leaving the interaction point are deflected in the plane transverse to the beam direction, and the tracks measured in the ID are curved. The curvature of a track is then used to determine the transverse momentum of the corresponding particle.

4.1.1 Pixel Detector

The pixel detector is the closest detector system to the beamline. It consists of 1774 modules arranged in three cylindrical layers located at a radius of 50.5 mm, 88.5 mm, and 122.5 mm from the beamline and six endcap disks (three on each side) located along the beam direction at distances of 495 mm, 580 mm, and 650 mm from the center of the detector. This arrangement provides three layers of coverage out to $|\eta| < 2.5$.

Each module contains a silicon sensor connected to a set of front end chips, each responsible for reading out a set of pixels and a module control chip that communicates with all the front ends. The pixel sensors are made with 250 μm thick n-type silicon wafers. High positive and negative dose regions are implanted into opposite sides of the wafer in a rectangular array. Each site on the array is a pixel. A large voltage is applied across the wafer to reverse bias the p-n junction at each pixel. This operating voltage is initially about 150 V but will rise up to 600 V over time due to radiation damage, which will eventually turn the n-type bulk silicon into a p-type bulk.

When a charged particle passes through the wafer, it ionizes atoms, and the resulting free electrons are moved to one side of the wafer by the applied electric field. Charge is collected at each pixel, and the resulting analog signal is converted to a digital time over threshold measurement using a comparator with reference voltage set to reject false signals from electronic noise. The threshold is set around 3500 electrons while a minimally ionizing particle typically generates a signal of around 20000 electrons.

Except for a few pixels located next to the front end chips, each pixel is 50 μm long in the direction transverse to the beamline and 400 μm long in the longitudinal direction. The remaining pixels have a size of 50×600 μm^2. Correspondingly, the pixel modules have a spatial resolution of 10 μm in the transverse direction and 115 μm in the longitudinal direction.

4.1.2 Semi-Conductor Tracker

The SCT is located outside the pixel detector and uses strips instead of pixels to cover a larger area while maintaining a manageable number of readout channels. A total of 4088 modules are arranged in double layers forming four cylinders in the barrel region at a radius of 284 mm, 355 mm, 427 mm, and 498 mm and nine endcap disks on either side at longitudinal distances between 853 mm and 2708 mm. Strips in the first layer are oriented along the beam direction with the second layer tilted at a small stereo angle to obtain resolution in the longitudinal direction that is much better than the strip length of 12 cm. Particles with $|\eta| < 2.5$ will cross at least four of these double layers.

SCT modules use a standard p-in-n silicon sensor with a thickness of 285 μm. Like the pixel detector, the SCT is operated initially at a bias voltage of 150 V that will eventually rise up to 350 V. The barrel modules are made of two 6 cm long sensors put together which are AC-coupled to readout strips with a pitch of 80 μm. Modules in the endcaps use strips with a constant azimuth and mean pitch of about 80 μm. The spatial resolution for SCT modules is 17 μm in the transverse direction and 580 μm in the longitudinal direction.

4.1.3 Transition Radiation Tracker

The final tracking system in the ID is the TRT. The barrel portion consists of 73 layers of drift tubes (also called "straws") interleaved with transition radiation fibers and spans the distance from a radius of 554 mm to a radius of 1082 mm while the endcap has 160 straw planes interleaved with transition radiation foils and is situated between 615 mm and 1106 mm along the beamline. Except for the transition region between the barrel and the endcap, which lies at $0.8 < |\eta| < 1.0$, particles with $|\eta| < 2.0$ cross an average of 36 straws.

Each straw is a polyimide tube 4 mm in diameter filled with a gas mixture of 70% Xe, 27% CO_2, and 3% O_2 and with a 31 μm diameter gold-plated tungsten wire running down the middle. The tube is made of two polyimide films coated on one side with a thin Al layer and bonded back-to-back using a polyurethane layer and has a total thickness of 70 μm. A charged particle passing through the straw tube will leave a trail of ionization behind. The central wire is held at ground and the tube walls at about -1500 V creating an electric field that drives the free electrons towards the wire. Along the way, these electrons ionize more atoms and the newly freed electrons are in turn accelerated by the field in a cascade that continues until the charge reaches the wire, which is connected to readout electronics. TRT straws only measure position in the transverse direction and have a spatial resolution of 130 μm.

Transition radiation material between the straws is used to help distinguish between tracks left by electrons and track left by pions. When a charged particle crosses the boundary between two materials with different dielectric constants, it will give off an amount of transition radiation proportional to its Lorentz factor γ. Thus, for a track of a given momentum, a particle with low rest mass will give more radiation than one with a larger rest mass. This radiation can also ionize gas in the straw tubes leading to a larger signal, called a "high threshold hit." The ratio high threshold hits to ordinary hits can then be used to discriminate between electrons and pions.

4.2 Calorimeter

The calorimeter is located outside the ID and solenoid and is composed of four subsystems used to measure the energy of electrons, photons, and hadrons. A high-granularity electromagnetic (EM) calorimeter provides precise measurements of electrons and photons and extends out to $|\eta| < 3.2$. Hadronic tile and endcap calorimeters (HEC) with a coarser granularity sufficient for measuring jets of hadrons cover the same η range outside of the EM calorimeter. A forward calorimeter (FCal) extends the coverage out to $|\eta| < 4.9$ with one EM layer and two hadronic layers. The EM calorimeter, HEC, and FCal all use liquid argon (LAr) as an active material while the tile calorimeter uses scintillating tiles. All of the calorimeters also use absorber plates to keep showers contained within the calorimeter and limit punch-through into the muon spectrometer.

4.2.1 EM Calorimeter

The EM calorimeter consists of two half barrels that extend out to $|\eta| < 1.475$ and outer and inner endcap wheels on either side that cover $1.375 < |\eta| < 2.5$ and $2.5 < |\eta| < 3.2$, respectively. The barrel and outer wheel have three layers of cells with the innermost layer having the highest granularity. A schematic for a barrel module is shown in Figure 4.3. The first layer is made of thin strips with $\Delta\eta \times \Delta\phi = 0.0031 \times 0.098$ while the second and third layers have more square dimensions of 0.025×0.0245 and 0.05×0.0245. The inner wheel has only the two more coarse layers. The total depth of the EM calorimeter ranges from 22 radiation lengths (X_0) to 33 X_0 in the barrel and 24-36 X_0 in the endcap.

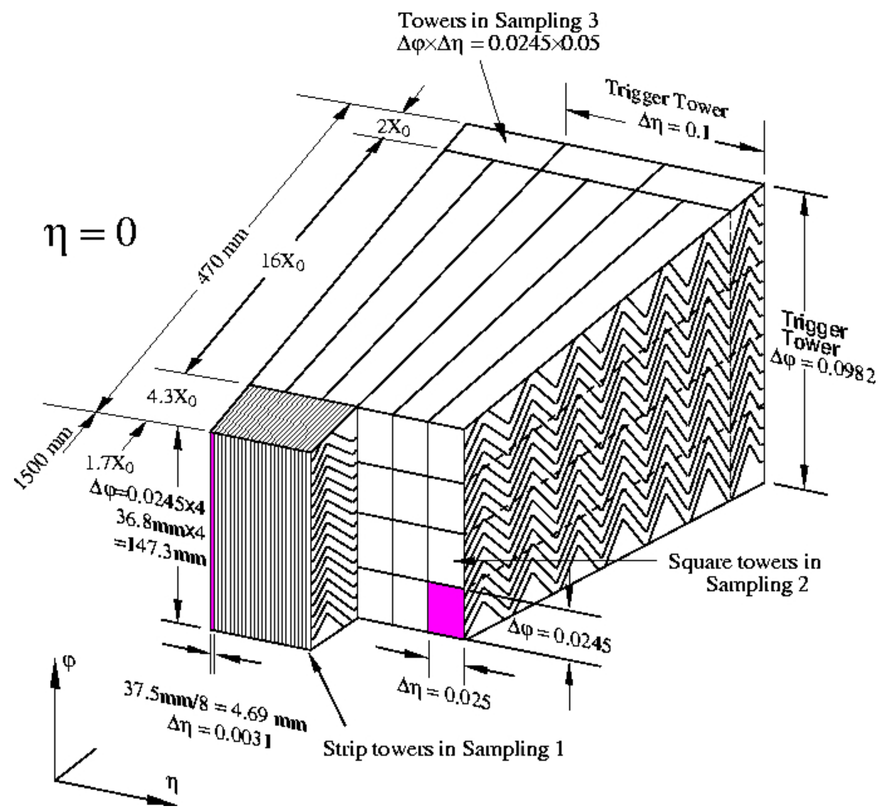

Figure 4.3: Schematic showing the cells in a barrel module of the EM calorimeter [44].

Modules in the EM calorimeter contain lead absorber plates and copper electrodes in an accordion shape with LAr in the gaps. Charged particles and photons ionize argon atoms, initiating a shower of electrons and photons. Charge is then collected at the electrodes, which consist of three copper plates separated by polyimide insulation. The outer two plates are held at high voltage, and the inner plate is used for the readout. Lead absorber plates help keep the shower contained and vary in thickness from 1.53(2.2) mm to 1.13(1.7) mm to limit the decreasing in sampling fraction with increasing(decreasing) $|\eta|$ in the barrel(endcaps).

The EM calorimeter has a measured energy resolution [46] of $\frac{\sigma(E)}{E} = 10\%/\sqrt{E(GeV)} \oplus 0.2\%$ and a spatial resolution of 50 mrad/$\sqrt{E}$ in η. A presampler located in front of the EM calorimeter for $|\eta| < 1.8$ also helps correct for energy lost by electrons and photons before reaching the calorimeter. It consists of a thin LAr layer, 11 mm thick in the barrel and 5 mm thick in the endcaps, with readout electrodes and no absorber plates.

4.2.2 Hadronic Tile Calorimeter

The tile calorimeter sits outside the EM barrel and contains a central barrel that extends out to $|\eta| < 1.0$ and extended barrels on either side that span $0.8 < |\eta| < 1.7$. Each barrel is segmented into three layers in depth. The first two layers have a granularity of $\Delta\eta \times \Delta\phi = 0.1 \times 0.1$ while the last layer has a granularity of 0.2×0.1. The total depth of the tile calorimeter is about 7.4 interaction lengths (λ).

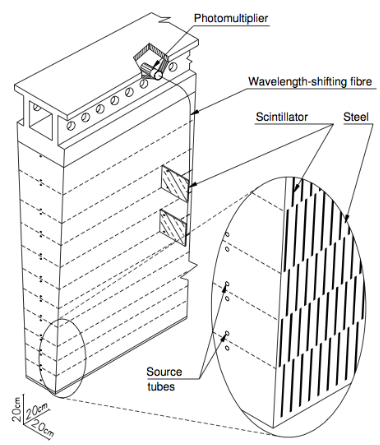

Figure 4.4: Sketch showing the structure of the tile calorimeter [44].

Modules are constructed from alternating steel plates and doped polystyrene tiles with a ratio by volume of 4.7:1. The steel plates act as an absorber, and polystyrene tiles are the active material. Incoming hadrons interact with nuclei in the tiles to produce hadronic showers. Photons produced in these showers are collected by wavelength-shifting fibers into photomultiplier tubes. The tiles are placed in reflective plastic sleeves to increase light yield and prevent damage. A schematic of this structure is shown in Figure 4.4. The energy resolution of the tile calorimeter has been measured to be within the desired resolution of $50\%/\sqrt{E} \oplus 3\%$ [47].

4.2.3 Hadronic Endcap and Forward Calorimeters

Like the EM calorimeter, both the HEC and FCal use LAr as the active material. The HEC has front and rear wheels covering the range of $1.5 < |\eta| < 3.2$ and $1.5 < |\eta| < 2.5$. Each wheel is separated into two layers. The front wheels use 24 copper plates with a thickness of 25 mm as absorbers while the rear wheels have 16 copper plates with a thickness of 50 mm. Regions with $|\eta| < 2.5$ have a granularity of $\Delta\eta \times \Delta\phi$ =0.1×0.1 while the remainder has a granularity of 0.2×0.2.

The FCal covers the range of $3.1 < |\eta| < 4.9$ and it split into three layers, one for electromagnetic measurement and two for hadronic measurement. The first layer uses copper plates as an absorber. The electrodes are coaxial copper rods that run through holes drilled in the copper plates. The second and third layers used tungsten rods that run between two copper end plates. Tungsten slugs fill the gaps between the rods and are the main absorbing material in these layers.

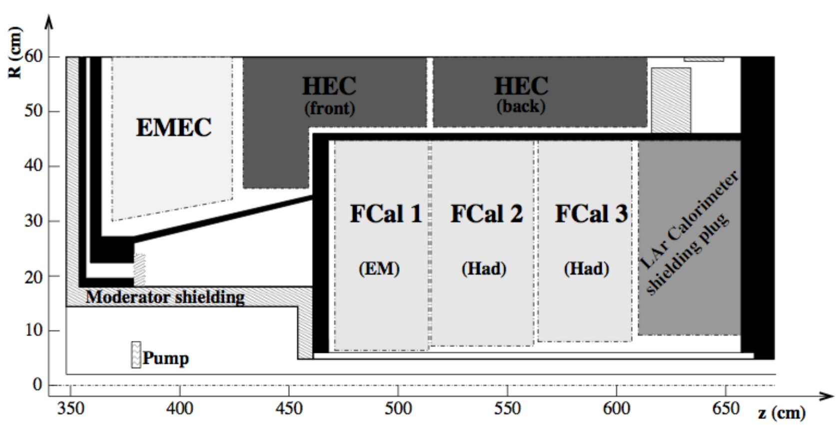

Figure 4.5: Arrangement of endcap and forward calorimeters [44].

The layout of the endcap and forward calorimeters is illustrated in Figure 4.5. The measured energy resolution of the HEC is about $21\%/\sqrt{E}$

for electrons and $70\%/\sqrt{E} \oplus 6\%$ for pions [48]. For the FCal these measurements are approximately $29\%/\sqrt{E} \oplus 3.5\%$ and $70\%/\sqrt{E} \oplus 3\%$, respectively [49].

4.3 Muon Spectrometer

The MS contains four subsystems that sit outside the calorimeter. Monitored Drift Tube chambers (MDTs) and Cathode Strip Chambers (CSCs) are used for precision tracking measurements. The remaining two systems have faster response times and are used for triggering. Resistive Plate Chambers (RPCs) are used in the barrel region, and Thin Gap Chambers are used in the endcaps. All of these systems work by collecting charge from gas ionized by the passage of a charged particle. The layout of the muon system is illustrated in Figure 4.6. The chambers are arranged in barrel layers at a radius of 5 m, 7.5 m, and 10 m and endcap disks located at distances of 7.4 m, 10.8 m, 14 m, and 21.5 m down the beamline.

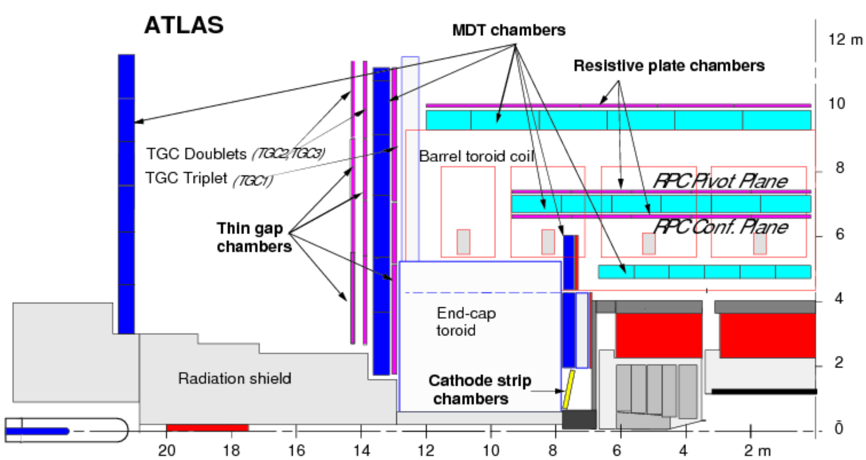

Figure 4.6: Sketch of the ATLAS muon system [50].

As in the inner detector, a magnetic field is used to bend tracks in the MS in order to measure the muons' momenta. The magnetic field in the MS is provided by a 0.5 T barrel toroid for $|\eta| < 1.4$ and two 1 T endcap toroids for $1.6 < |\eta| < 2.7$. The field in transition region of $1.4 < |\eta| < 1.6$ is a combination of the barrel and endcap fields. The MS covers a much larger distance than the ID (several meters as opposed to one meter) which allows for precise measurements of muon momentum up to a few TeV.

4.3.1 Precision Chambers

Monitored Drift Tube chambers make up most of the precision tracking chambers in the MS. Except for the innermost layer, they provide coverage out to $|\eta| < 2.7$. The first layer extends only out to $|\eta| < 2.0$ due to the inability of the MDTs to handle the expected hit rate at $|\eta| > 2.0$. MDT chambers are made of 3-8 layers of drift tubes. The tubes have a diameter of 50 mm and are filled with 93% Ar and 7% CO_2. Charge is collected on a central tungsten-rhenium wire held at a potential of approximately 3 kV. Individual tubes have a spatial resolution of 80 μm, and the average resolution of a chamber in the bending direction is about 35 μm.

Cathode Strip Chambers are used for the first layer of precision tracking for $|\eta| > 2.0$. They are multiwire proportional chambers with 30 μm-diameter anode wires running radially and two sets of cathode strips, one parallel to anode wires and the other perpendicular. The chamber is filled with a gas mixture of 80% Ar and 20% CO_2 and operated at a voltage of 1.9 kV. Charge is collected at each strip and track position is measured by interpolating between them. The disk is made of alternating large and small chambers that have a different spacing between readout strips. Large chambers have a readout pitch of 5.31 mm in the bending direction and 21 mm in the transverse direction. For the small chambers these numbers are 5.56 mm and 12.92 mm, respectively. This results in a resolution of 40 μm in the bending direction and 5 mm in the transverse direction.

4.3.2 Trigger Chambers

The short distances and large electric fields used in the RPCs and TGCs result in short drift times that allow these measurements to be used for fast triggering. Both detectors read out a signal in less than 25 ns and have timing resolution of a few ns, which allows the signal to be accurately matched to a bunch crossing. In addition, they provide a measurement of the azimuthal coordinate which is not measured precisely by the MDTs.

Resistive Plate Chambers are used as the trigger chambers out to $|\eta| < 1.05$. Rather than using wires with a radial electric field, the RPCs have two resistive plates 2 mm apart with a uniform electric field between them. The plates are held at a potential difference of 9.8 kV, and gap is filled with 94.7% $C_2H_2F_4$, 5% Iso-C_4H_{10}, and 0.3% SF_6. Readout strips are attached to the outer faces of the plates with a pitch of 23-35 mm. The resulting spatial resolution is 10 mm in both directions. With the long distance between the first two RPC layers and the third layer, this is sufficient to resolve tracks with momentum up to 35 GeV.

Thin Gap Chambers provide triggering capability for $1.05 < |\eta| < 2.4$. They are multiwire proportional chambers with a wire-to-cathode distance, 1.4 mm, shorter than the wire-to-wire distance, 1.8 mm and use a highly-quenching gas mixture of 55% CO_2 and 45% n-pentane. The wires are held at a potential of 2.9 kV. Better spatial resolution is needed at higher $|\eta|$ to maintain good momentum resolution. This is achieved by varying the size of the wire groups used to measure the position from 6 to 31 wires. The TGCs have a spatial resolution that varies from 2-6 mm in the radial direction and 3-7 mm in the azimuthal direction.

4.4 Trigger System

ATLAS uses a trigger system to reduce the rate of recorded events from the 40 MHz collision rate to 1 kHz. This is done in three stages, referred to as Level 1 (L1), Level 2 (L2), and Event Filter (EF), each using progressively more information (and therefore taking more time) to render a decision as to whether or not to keep the event. This decision is made based on the presence of high transverse momentum objects (leptons, photons, jets), large missing transverse energy ($E_{\mathrm{T}}^{\mathrm{miss}}$), or large total transverse energy.

Unlike the later trigger stages, which are purely software systems, the L1 trigger is implemented in hardware in order to increase speed. It makes its decision using information from calorimeter towers spanning approximately 0.1×0.1 in (η,ϕ) as indicated in Figure 4.3 and the trigger chambers in the muon system. Electron candidates are made from 2×2 clusters of trigger towers, and energy in the surrounding 12 towers is used to determine if the electron is isolated. Muon candidates are formed by looking for a coincidence of hits in the trigger chambers that lie within a road of variable width pointing back to the interaction point. The width of the road depends on the p_{T} threshold of the trigger. After L1, the output rate is about 75 kHz.

That output rate is reduced to 3.5 kHz by the L2 trigger, which selects events based on "Regions of Interest" (RoIs) supplied by the L1 triggers. Each RoI corresponds to an object passing one of the L1 selections. These objects are rebuilt at L2 using information from all subsystems of the detector within the RoI, not just the trigger chambers and towers. The final stage is the EF, which reconstructs the entire event using the same algorithms used for offline event reconstruction, which are discussed in Chapter 5. Events passing a set of EF selections are recorded in one or more data streams based on what type of object passed the trigger.

Chapter 5

Object Reconstruction and Event Selection

5.1 Track and Vertex Reconstruction

Tracks are reconstructed from hits in the inner detector and fit for five parameters, which are measured at the point of closest approach to the beamline: the radius of curvature of the track, from which the ratio of charge to transverse momentum (q/p_{T}) can be derived, the azimuthal and polar angles (ϕ and θ) in the ATLAS coordinate system, and the transverse and longitudinal impact parameters (d_0 and z_0), which are defined as distance in the transverse plane or on the longitudinal axis between the track and origin/interaction region/vertex.

Track reconstruction in ATLAS begins with an inside-out algorithm that builds track candidates from hits in the pixel detector and the first layer of the SCT [51]. Clusters of nearby hits in each layer are converted into three-dimensional space points. Combinations of points define track seeds, and the reconstruction algorithm then looks for points in the last three SCT layers the lie on "roads" extending from the ends of the seeds. Tracks are fit to these collections of points, and outliers are removed.

At this stage, it is possible for a single hit to be associated with more than one track. These ambiguities are resolved by scoring tracks based on how precisely hits match the fitted track and whether the track has any holes (missing hits). Hits shared between tracks are assigned to the highest scoring track, and quality criteria are applied to remove fake tracks.

The remaining tracks are extended into the TRT and refit with the new hits in addition to the hits in the silicon layers. The quality before and after the refit are compared, and TRT hits resulting in a worse fit are labeled as outliers and removed from the fit (but remain associated with the track). Once the extension of silicon tracks into the TRT is finished, an outside-in tracking algorithm takes unused segments of TRT hits as seeds and attempts to extend them back into the silicon layers. This helps recover efficiency for tracks not originating from the primary interaction. The track reconstruction efficiency as a function of $|\eta|$ for simulated muons, pions, and electrons with a p_{T} of 5 GeV is shown in Figure 5.1. Muons have a very high track reconstruction efficiencies while the efficiencies for pions and electrons decrease significantly as the amount of material traversed increases. This is due to hadronic interactions with the detector for pions and bremsstrahlung radiation for electrons.

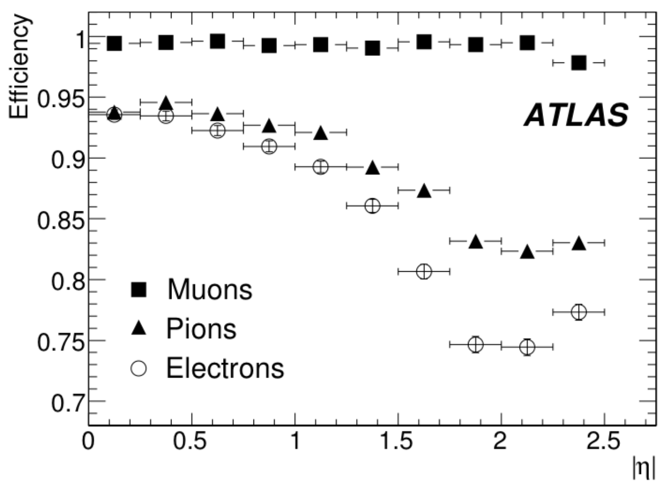

Figure 5.1: Track reconstruction efficiency for tracks belonging to muons, pions, and electrons with a p_{T} of 5 GeV [51].

Vertex reconstruction is performed using tracks that are consistent with originating from the interaction region. The criteria used to select these tracks are specified in Ref. [52]. An iterative procedure is used to find vertices and fit their position. First, a vertex seed is made by looking for a global maximum in the distribution of the z-coordinate of the selected tracks. Then a χ^2-based fitting procedure that down-weights the contribution from outlying tracks is used to determine the vertex position. Multiple iterations of the fit are performed with progressively more down-weighting. Once this is done, all remaining tracks that are incompatible with the fitted vertex by more than 7σ are used to seed a new vertex, and tracks associated with the fitted vertex are refit using the vertex position as a constraint. This is repeated until all tracks are associated with a vertex or until no new vertices can be found. The vertex with the highest Σp_{T}^2 of associated tracks is considered the primary vertex. The efficiency for vertex reconstruction as a function of the number of reconstructed tracks is shown in Figure 5.2, measured for 7 TeV collisions in 2010 [53]. For vertices with three or more tracks, this efficiency exceeds 99%.

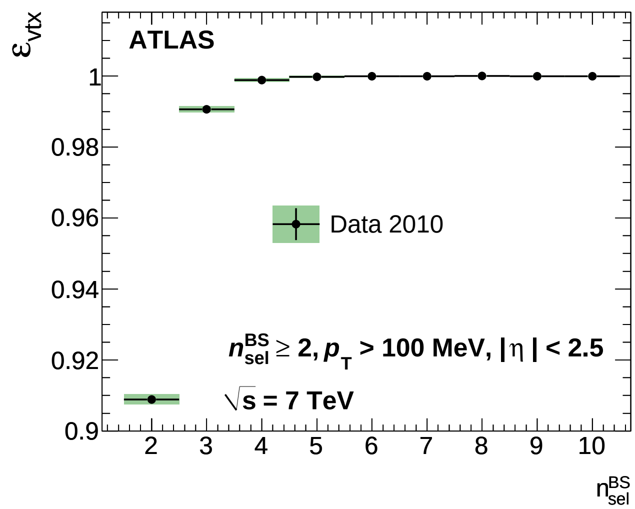

Figure 5.2: Vertex reconstruction efficiency as a function of the number of reconstructed tracks. Figure taken from Ref. [53].

5.2 Electron Reconstruction

Electron candidates within the tracking acceptance ($|\eta| < 2.47$) are reconstructed from a combination of an energy cluster in the EM calorimeter and a track [54]. A sliding-window algorithm with a window size corresponding to a 3×5 block of cells in the middle layer of the calorimeter is used to look for clusters of cell towers with a total transverse energy (E_{T}) greater than 2.5 GeV. Tracks are extrapolated to the middle layer of the calorimeter, and at least one track is required to be within $|\Delta\eta| < 0.05$ and an asymmetric $|\Delta\phi|$ window that is 0.1 on the side where the track bends and 0.05 on the other side. If multiple tracks fit this criteria, the track with the smallest $\Delta R = \sqrt{\Delta\eta^2 + \Delta\phi^2}$ is selected.

After the initial candidates are found, the clusters are rebuilt using a 3×7 block of towers in the barrel and a 5×5 block in the endcap. The total energy of the cluster is then calculated as the sum of the measured energy in the cluster plus estimates of the amount of energy lost before reaching the calorimeter, deposited in cells outside the cluster, and deposited behind the EM calorimeter. These estimates are parameterized as function of measured energies in the presampler and each layer of the EM calorimeter within the cluster using simulations of detector response. The four-momentum for the electron candidate is then constructed using the energy of the rebuilt cluster and the η and ϕ of the associated track.

Outside of the tracking acceptance, electron candidates are reconstructed from a calorimeter cluster only. These clusters do not have a fixed size and are formed using the significance of measured energy over expected noise to group neighboring cells together. To be reconstructed as an electron, the cluster is required to have a small hadronic component and a transverse energy greater than 5 GeV. Since there is no associated track, the electron direction is determined by the average position of cells in the cluster, weighted by the energy in each cell. The remainder of this section will focus on central electrons since forward electrons are not used in this measurement.

Electron candidates are identified as electrons using several selections on shower-shape and tracking variables. Three categories of electrons are defined(loose, medium and tight) in order to have good acceptance and progressively higher background rejection. The loose category imposes requirements on the ratio of energy in the hadronic calorimeter to energy in the EM calorimeter and on the transverse shower shape in the middle layer of the EM calorimeter. The medium category adds further requirements on the shower width in the first layer of the EM calorimeter and on the number of silicon hits and transverse impact parameter of the electron track. The tight category builds on the medium requirements, imposing stricter requirements on track-cluster matching and transverse impact parameter and adding selections on the number of TRT hits and the ratio of high-threshold to total hits. Tight electrons are also required to have a hit in the first layer of the pixel detector and not be matched to any photon conversions.

The efficiency for electron reconstruction and identification has been measured in 8 TeV collision data using a selection designed to pick out $Z \to ee$ events [55]. The results are shown in Figure 5.3 as a function of E_{T} for electrons within the tracking volume and as a function of η for electrons with $E_{\mathrm{T}} > 7$ GeV. The efficiencies of interest for this measurement are the efficiencies for the loose selection (used for estimating non-prompt background and third lepton veto) and the tight selection (nominal electron identification used in the analysis). Typical efficiency for the loose selection is between 90% adn 95% while the efficiency for the tight selection ranges from 65% to 80%.

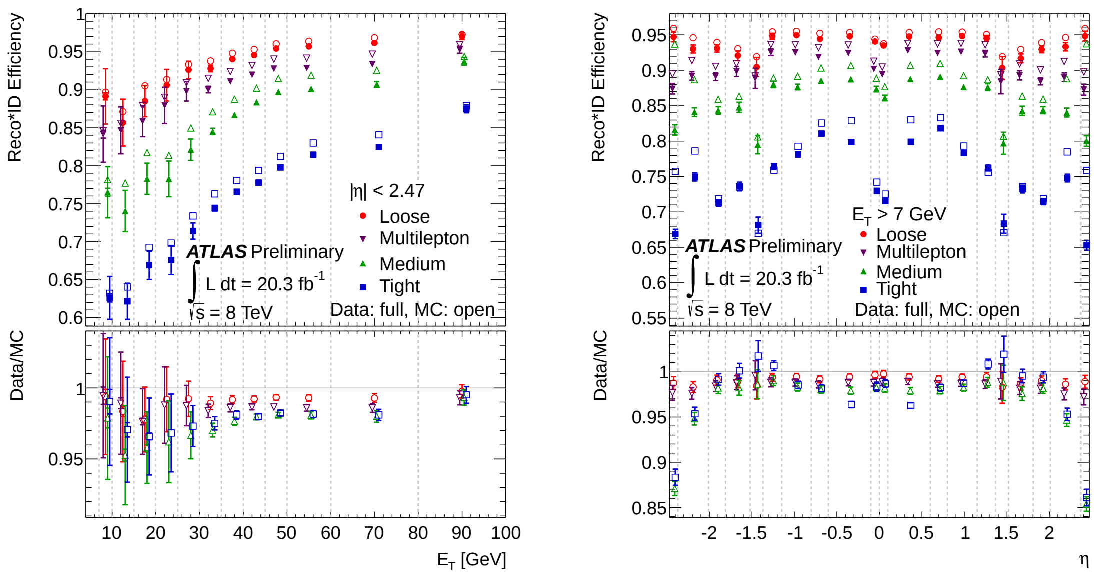

Figure 5.3: Electron reconstruction and identification efficiency as a function of p_{T} (left) and η (right). Filled points show the efficiencies measured in data while efficiencies measured in MC are indicated by the open points. Figure taken from Ref. [55].

5.3 Muon Reconstruction

Muons are reconstructed in three categories based on whether the muon has a track in the MS, ID, or both [51]. Standalone muons consist only of a track in the muon spectrometer. Tracks are formed in the MS starting with a 0.4×0.4 region in (η, ϕ) space centered on a hit in the RPC/TGC trigger chambers [57]. Each precision tracking station that intersects this area is used to look for straight-line track segment that point approximately back to the interaction region. A straight line can be used for the track segments because of the small distance between hits in a station. Track candidates are first formed from segments with a second-coordinate hit (RPC/TGC/CSC hit) by extrapolating between segments in different stations using a scan around a rough estimate of the muon's momentum from one segment. If a match is found, a track is fit to the two segments and the refined momentum estimate is used to extrapolate to other stations. Once the full track has been constructed, it is refit using the raw hit information instead of the straight-line segments and taking into account the matter traversed by the muon.

Combined muons are formed by matching a track in the muon spectrometer to a track in the inner detector. Tracks are matched using a χ^2 that is defined as the difference in track parameters between the two tracks at the point of closest approach to the beamline weighted by the combined covariance matrix. If a match is found, a combined track is made that is a statistical combination of the track parameters of the ID and MS tracks.

Tracks in the ID that are not associated with a combined muon and unused track segments in the MS can be used to form tagged muons. This is done by extrapolating ID tracks out to the muon system and looking for nearby track segment. In this case, the momentum of the muon is taken from the ID track.

Figure 5.4 shows the efficiency for a muon to be reconstructed as a combined muon (CB) and for a muon to be reconstructed as either a combined or tagged (CB+ST) muon, measured in 8 TeV collisions using $Z \to \mu\mu$ events [58]. The reconstruction efficiency for combined muons is about 95% or better across most of the detector but suffers greatly for $|\eta| < 0.1$, where room must be left for the services for the ID and calorimeter, and $1.1 < \eta < 1.3$, where the installation of muon chambers was not completed before the first run of the LHC. The inclusion of tagged muons recovers the lost efficiency for $1.1 < \eta < 1.3$ but only brings the efficiency up to about 65% for $|\eta| < 0.1$.

5.4 Jet Reconstruction

Jets are formed by combining topological clusters of energy deposits in the calorimeter [59]. Clusters are seeded by cells with a signal that is at least four times greater than the expected electronic noise. Any adjacent cell with a signal-to-noise ratio greater than 2 is added to the cluster until there are no such cells remaining. Then all cells adjacent to those cells are added. An energy-weighted average of cell positions is used to define the position of the cluster.

Clusters are combined using the anti-k_t algorithm [60], which works by comparing distances between objects, d_{ij}, to the distance between an object and the beam, d_{iB}. These distances are defined as follows:

$$d_{ij} = \min(\mathrm{k}_{\mathrm{t,i}}^{-2}, \mathrm{k}_{\mathrm{t,j}}^{-2}) \frac{\Delta_{\mathrm{ij}}^2}{\mathrm{R}^2} \tag{5.1}$$

$$d_{iB} = k_{t,i}^{-2} \tag{5.2}$$

where $k_{t,i}$ is the transverse momentum of object i, $\Delta_{ij} = \sqrt{(y_i - y_j)^2 + (\phi_i - \phi_j)^2}$, and R is a parameter used to restrict the size of jets. These distances are calculated starting with the cluster with the highest transverse energy. If the minimum distance is one of the d_{ij}, then object j is added to object i, and the distances are recomputed. Otherwise, object i is considered a complete jet and removed from the algorithm. This process continues until there are no more clusters left to be combined. The factor of $\frac{\Delta_{ij}^2}{R^2}$ in Equation 5.1 prevents the addition low-energy clusters outside a radius of R from the jet center. Jets used for this measurement are clustered with R=0.4.

The efficiency for jet reconstruction (with a radius parameter of 0.6) with respect to "truth" jets is shown as a function of the true jet p_{T} for jets with $|\eta| < 1.9$ in Figure 5.5. Truth jets are defined using the same clustering algorithm used for jet reconstruction, but instead of energy deposits in the calorimeter, the inputs are stable particles from the MC truth record. All particles with a lifetime longer than 10 ps are included in the clustering of truth jets with the exception of muons (which deposit little energy in the calorimeter) and neutrinos (which escape undetected). Truth jets give a good approximation of the object that would be reconstructed if the calorimeter was perfectly efficient. The measured efficiency for jet reconstruction is better than 99% for truth jet p_{T} above 20 GeV.

After jets are formed, the jet energy must be recalibrated to account for the difference in detector response between electromagnetic showers and hadronic showers. Two methods of jet energy calibration are used in this analysis. The simplest method, EM+JES, starts by treating every cluster as an electromagnetic shower. A correction is then applied based on the measured jet energy at the electromagnetic scale. The second method, LCW+JES, classifies individual clusters as electromagnetic or hadronic and applies energy corrections at the cluster level. After these local corrections are done, a second correction is applied to the jet as a whole. Figure 5.6 shows the fractional energy resolution measured in di-jet events in the 2011

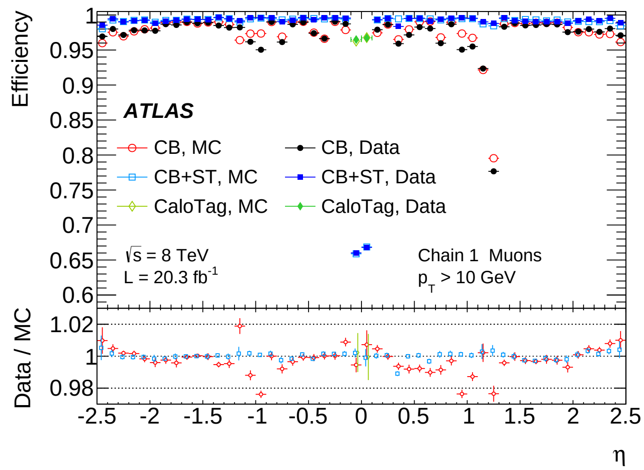

Figure 5.4: Muon reconstruction efficiency as a function of η. Filled points show the efficiencies measured in data while efficiencies measured in MC are indicated by the open points. Figure taken from Ref. [58].

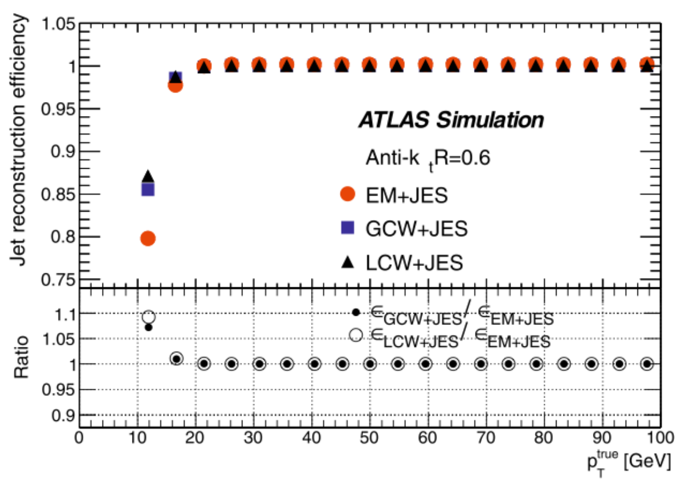

Figure 5.5: Jet reconstruction efficiency as a function of truth jet p_{T} for jets with $\eta < 1.9$ [59].

dataset [61] using two different techniques described in Ref. [62]. The energy resolution ranges from about 20% for jets with a p_{T} of 30 GeV to 5% for jets with a p_{T} of 1 TeV.

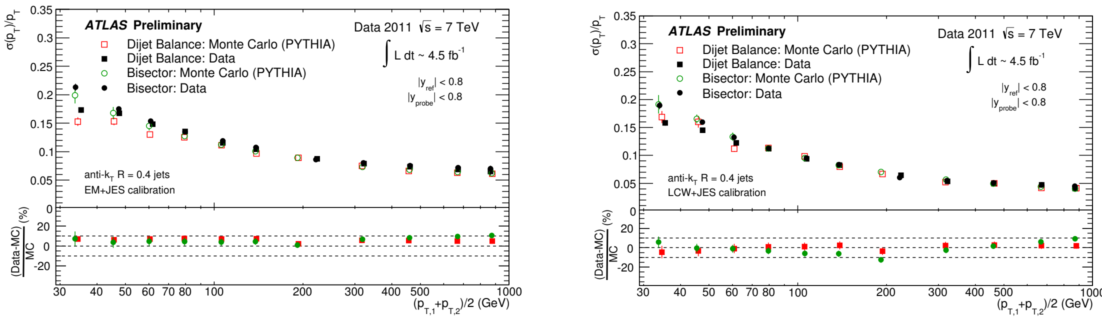

Figure 5.6: Jet energy resolution as a function of the average p_{T} of the two jets in the event for jets calibrated using EM+JES (left) and LCW+JES (right). Filled points show the resolution measured in data while the resolution measured in MC is indicated by the open points. Figure taken from Ref. [61].

For jets with $|\eta| < 2.5$, tracks are also associated with the jets for subsequent use in identifying jets initiated by a b quark (see Section 5.4.1) and rejecting jets originating from pileup interactions. Tracks are assigned to jets via ghost association [63], which includes tracks in the anti-k_t jet clustering but assigns them all very low p_T so that they are only added to nearby jets without otherwise influencing jet formation. Jet vertex fraction (JVF) is defined as the ratio of the sum of the momenta of all tracks in the jet that are associated with the primary vertex to the sum of the momenta of all tracks in the jet that are associated with some vertex in the event. This quantity is used to reject jets originating from extra pp interactions. Figure 5.7 shows the number of reconstructed jets in $Z \to \ell\ell$ events measured in 7 TeV collisions as a function of the number of reconstructed vertices with and without a requirement that jets have JVF greater than 0.75 [64]. Adding the JVF cut creates a nearly flat distribution, indicating good rejection of pileup jets.

5.4.1 Tagging b jets

Due to the small mixing between the third generation of quarks and the first two generations, hadrons containing b quarks have relatively long lifetimes and can travel a measurable distance before decaying. Typical lifetimes/distances traveled before decaying for B hadrons are around 1.5 ps/450 μm. ATLAS has several algorithms that exploit this fact to identify jets initiated by b quarks by using tracks associated to the jet to look for evidence of a B hadron decay [65]. The IP3D algorithm compares 2D distributions of transverse and longitudinal impact parameter significance, defined as the ratio of the impact parameter to its uncertainty, to Monte Carlo templates for b jets and light jets. A likelihood ratio between the two hypothesis is then used to classify the jet in question. Two other algorithms, SV1 and JetFitter, work by reconstructing secondary vertices inside the jet. SV1 only attempts to make one vertex for the B hadron decay while JetFitter also attempts to resolve the subsequent D hadron decay. Both algorithms classify jets using a likelihood from the comparison of several variables related to secondary vertices (e.g. decay length significance, invariant mass of tracking making the vertex) to simulated distributions. In addition to b jets and light jets, JetFitter has a third classification for c jets. Jets used in this analysis are classified using a neural network that combines IP3D, SV1, and JetFitter called MV1. Figure 5.8 shows the efficiency in simulated $t\bar{t}$ events for b, c, and light jets to pass a selection on the MV1 output calibrated to have an efficiency of 70% for b jets with p_{T} greater than 20 GeV and $|\eta| < 2.5$ [66].

5.5 $E_{\mathrm{T}}^{\mathrm{miss}}$ Reconstruction

Although they don't interact with the detector, the presence of one or more neutrinos in an event can be deduced from an observed momentum imbalance in the transverse plane, referred to as missing transverse energy ($E_{\mathrm{T}}^{\mathrm{miss}}$). Longitudinal momentum imbalances cannot be used in the same manner since particles moving collinear with the beamline do not hit the detector. $E_{\mathrm{T}}^{\mathrm{miss}}$ is reconstructed from topological clusters in the calorimeter and reconstructed muons [67].

Cluster energies are calibrated according to which (if any) reconstructed object the cluster belongs to. Clusters matched to photons are calibrated at the EM scale, jets with p_{T} less than 20 GeV are calibrated at the LCW scale without applying a subsequent JES correction, and all other objects use their default calibration. Clusters not belonging to any reconstructed object are also calibrated at the LCW scale. Muons are added using the measured track momentum. In the case of isolated combined muons, energy deposited in the calorimeter is taken into account by the combination of the

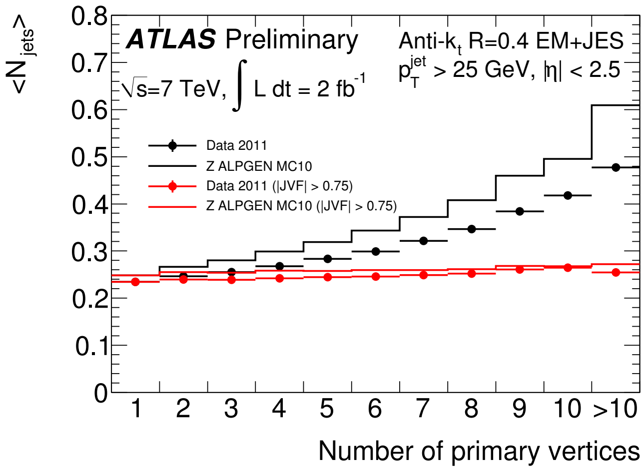

Figure 5.7: Number of reconstructed jets as a function of the number of reconstructed vertices with and without requiring the jet vertex fraction to be greater than 0.75. Figure taken from Ref. [64].

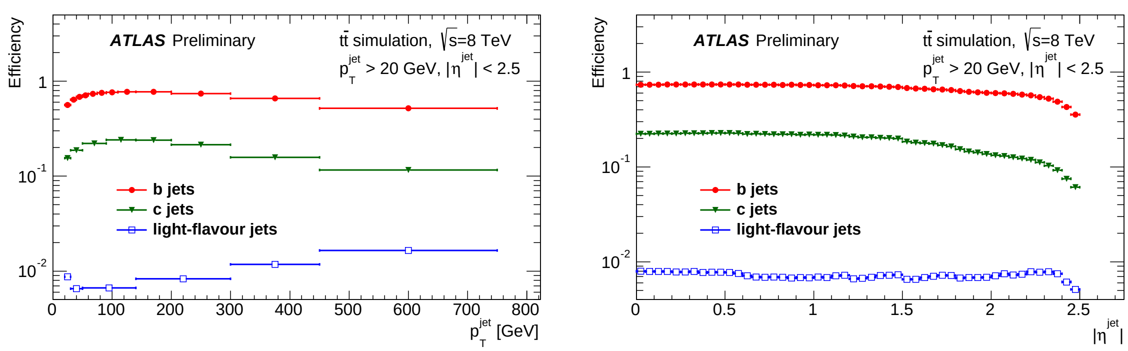

Figure 5.8: Efficiency as a function of p_{T} (left) and $|\eta|$ (right) in simulated $t\bar{t}$ events for b, c, and light jets to pass a selection on the MV1 output calibrated to have an efficiency of 70% for b jets with p_{T} greater than 20 GeV and $|\eta| < 2.5$. Figure taken from Ref. [66].

ID and MS tracks, so clusters associated with the muon are removed from the calculation. Figure 5.9 the $E_{\mathrm{x}}^{\mathrm{miss}}$ and $E_{\mathrm{y}}^{\mathrm{miss}}$ resolution as a function of the scalar sum of all transverse energy in the calorimeter and the transverse momenta of any muons in the event [68]. Similar resolutions of about 5 GeV for events with 50 GeV of transverse energy to about 25 GeV for events with 1 TeV of transverse energy are seen for several types of simulated collisions containing one or more energetic neutrinos.

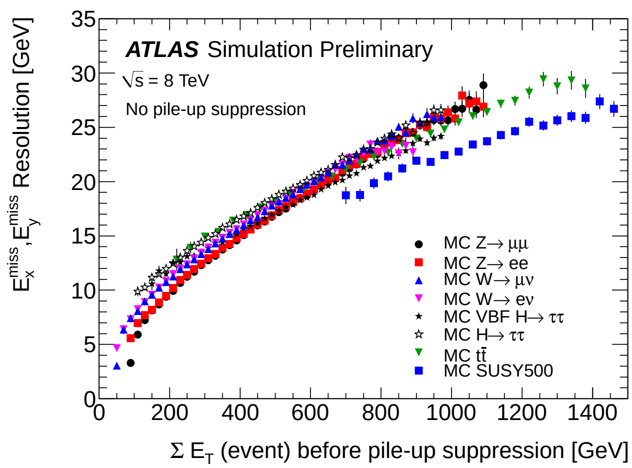

Figure 5.9: $E_{\mathrm{x}}^{\mathrm{miss}}$ and $E_{\mathrm{y}}^{\mathrm{miss}}$ resolution as a function of the scalar sum of all transverse energy in the calorimeter and the transverse momenta of any muons in the event. Figure taken from Ref. [68].

5.6 Event Selection

Events are collected using four single-lepton triggers, two which require the lepton to be isolated and two which do not. The two isolated lepton triggers require an electron or muon with $p_{\mathrm{T}} > 24$ GeV while the remaining triggers have higher thresholds of 36 GeV for muons and 60 GeV for electrons. Events that pass these triggers are subjected to a number of quality requirements before being considered for analysis. They are only used if they are included in a "good runs list," a list of times when the detector was fully operational. This selection is extremely efficient, rejecting less than 5% of recorded data. Further checks are made that the event was written out correctly and that there are no bursts of noise in the calorimeter [69] that interfere with the event. The primary vertex in the event is required to have at least three tracks.

In the remaining events, electrons, muons, and jets are selected from available reconstructed objects. Three types of selection criteria are defined for leptons: a "tight" selection used to select the two same-sign leptons, a "veto" selection used to find additional leptons present in $W^{\pm}Z$ or ZZ events, and a "loose" selection used to estimate the background from events with a single prompt lepton. Tight electrons must satisfy identification criteria similar to the tight selection in Ref. [54] and are subject to several additional requirements. They must have transverse energy greater than 25 GeV and $|\eta| < 2.47$ with the transition between EM barrel and endcap calorimeters excluded ($1.37 < |\eta| < 1.52$). The transverse and longitudinal impact parameters must satisfy $|\frac{d_0}{\sigma(d_0)}| < 3$ and $|z_0 \times \sin\theta| <$0.5 mm. Finally, calorimeter and tracking isolation selections are applied as follows: the sum of the transverse energy of all calorimeter clusters ($E_{\mathrm{T}}^{\mathrm{iso}}$) and the sum of the transverse momenta of tracks ($p_{\mathrm{T}}^{\mathrm{iso}}$) within a cone of radius R=0.3 in (η, ϕ) space are required to be less than 14 percent and 6 percent of the electron's transverse energy, respectively.

In the veto and loose selections, electrons are only required to pass a loose identification selection. The E_{T} threshold is lowered to 7 GeV, and the tracking isolation requirement is removed for veto electrons. For loose electrons, the impact parameter requirements are loosened to $|\frac{d_0}{\sigma(d_0)}| < 10$ and $|z_0 \times \sin\theta| < 5$ mm, and the isolation criteria are reversed but with a new upper limit that the ratio of transverse energy/momentum in the isolation cone to the electron's transverse energy must be less than 2.

Tight muons are required to be reconstructed as combined muons with the same charge measured in the ID and MS. They must have $p_{\mathrm{T}} > 25$ GeV and $|\eta| < 2.5$. The ID tracks associated with these muons must pass a number of quality requirements. The number of hits or dead sensors crossed in the pixel detector must be at least one, and the same quantity for the SCT must be at least five. For muons with $0.1 < |\eta| < 1.9$, the track must have at least six hits in the TRT, and the fraction of these which are outliers must not exceed 0.9. Tight muons also have the same impact parameter requirements as tight electrons and similar isolation requirements of $E_{\mathrm{T}}^{\mathrm{iso}}/p_{\mathrm{T}}^{\mu} < 0.07$ and $p_{\mathrm{T}}^{\mathrm{iso}}/p_{\mathrm{T}}^{\mu} < 0.07$.

The selection of veto muons includes standalone and tagged muons. The p_{T} threshold is lowered to 6 GeV, the calorimeter isolation requirement is dropped, and the track isolation selection is loosed to be less than 15 percent of the p_{T} of the muon. Loose muons still must be combined, but just as for loose electrons, the impact parameter requirements are loosened, and isolation requirements are reversed. In the remaining chapters, "tight" and "loose" will be used to refer to the analysis selections rather than just identification criteria unless otherwise specified.

Jets are required to have p_{T} (calibrated with EM+JES) greater than 30 GeV and $|\eta| < 4.5$. In order to reduce the probability of selecting a jet from a pileup interaction, jets with $|\eta| < 2.4$ and $p_{\mathrm{T}} < 50$ GeV are required to have a jet vertex fraction greater than 0.5. Jets passing these selections are tested with the MV1 algorithm. If the MV1 output exceeds a working point with an efficiency of 70 percent for b jets, then the jet is classified as a b jet.

To avoid the case where a single particle is reconstructed as more than one object, some removal of overlapping objects is performed. If the event contains a tight electron and a jet with $\Delta R(e, jet) < 0.3$, then the jet is removed. If the same is true for a jet and a tight muon, the event is rejected since the muon is likely to originate from the decay of a hadron within the jet. When estimating the background due to such hadron decays, jets are also removed if they fall within $\Delta R < 0.3$ of a loose lepton that is one of the two highest-p_{T} leptons. For tight electrons and tight muons lying within $\Delta R < 0.1$ of each other, the electron is removed. This μ/e overlap removal is also extended to loose leptons within the leading two leptons when estimating the non-prompt background.

After overlaps are resolved, events are selected with exactly two tight leptons with the same electric charge and an invariant mass ($m_{\ell\ell}$) between them greater than 20 GeV. To reduce background from $W^{\pm}Z$, events with a third lepton passing the veto selection are rejected. In the case where the two tight leptons are both electrons, an additional requirement is made that the invariant mass of the two electrons differs from the mass of the Z boson by at least 10 GeV. Since two neutrinos are also expected in the event, $E_{\mathrm{T}}^{miss} > 40$ GeV is also required. Events are required to have at least two jets, but in order to reduce the non-prompt background, the event is rejected if any jet is classified as a b jet. Remaining events with an invariant mass between the leading two jets (m_{jj}) greater than 500 GeV are kept. This selection is referred to as the inclusive signal region (Incl SR), and both the electroweak and strong production mechanisms of $W^{\pm}W^{\pm}jj$ are treated as signal in this region. An addition signal region, called the VBS signal region (VBS SR), is defined to consist of events in the inclusive signal region for which the separation in rapidity between the two leading jets ($|\Delta y_{jj}|$) is greater than 2.4. In this region only the electroweak production is considered signal.

Chapter 6

Signal and Background Estimation

Events populating the signal regions come from a variety of physical processes. Estimates of the number of events produced by each process that are selected by this analysis are necessary in order to obtain a meaningful measurement of the $W^{\pm}W^{\pm}jj$ process. These estimates are made with a combination of Monte Carlo (MC) and data-driven techniques. Modeling of background processes is tested in a variety of control regions designed to be similar to the signal region but with a few selections changed to greatly enhance the contributions from particular backgrounds with respect to the signal.

Processes that produce prompt same-sign leptons and $W^{\pm}\gamma$ events are estimated using Monte Carlo simulation. Events are generated in two steps: the hard scattering of constituents within the proton followed by the hadronization of outgoing quarks and gluons. After events have been generated, the interaction of particles with the detector is simulated [70] using GEANT4 [71]. The event is then reconstructed from the simulated detector signals in the same manner as for actual data. Following reconstruction, several small correction factors are applied to make the simulation more accurately mimic the data. Corrections are applied for the average number of pileup interactions, the average z position of vertices, the identification efficiencies of leptons, the energy/momentum scale and resolution for leptons and jets, and the b-tagging efficiency and mis-tag rate for jets.

Processes that produce just one prompt lepton or two opposite-sign leptons can enter the signal region due to secondary decays and instrumental effects. Contributions from these processes are estimated using data-driven techniques. In each case, the expected number of events in the signal region is determined by extrapolating from observed events in a very similar control region with a different lepton selection. The extrapolation factor between the regions is measured by comparing lepton selections in other control regions that are enriched in the background process of interest. These estimates are described in more detail in Sections 6.2.1 and 6.3.

6.1 Prompt Processes

6.1.1 $W^{\pm}W^{\pm}$

The electroweak and strong production of $W^{\pm}W^{\pm}jj$ events are simulated separately using the SHERPA [72] event generator and normalized to next-to-leading-order (NLO) cross sections calculated in two fiducial regions designed to mimic the signal regions of this analysis. The fiducial regions are defined as follows: Events must contain two leptons (e/μ) with the same electric charge, p_{T} greater than 25 GeV, and $m_{\ell\ell}$ >20 GeV. There must also be two truth jets found using the anti-k_t algorithm with a radius parameter of R=0.4 with a p_{T} greater than 30 GeV and $|\eta|$ <4.5, and the transverse energy of the vector sum of the momenta of all neutrinos in the event must be greater than 40 GeV. For any pair of leptons or lepton-jet pair, $\Delta R(\ell,\ell)$ or $\Delta R(\ell,j)$ is required to be greater than 0.3. Events with m_{jj} >500 GeV form the inclusive region while an additional requirement of $|\Delta y_{jj}|$ >2.4 defines the VBS region.

Cross sections in these two regions ("fiducial cross sections") are calculated using POWHEGBOX [73,74] with CT10 [12] parton distribution functions (PDFs) and with PYTHIA8 [75,76] used for parton showering and underlying event. The acceptance, the fraction of generated events that pass fiducial region selections, of the SHERPA samples is then used to convert the fiducial cross sections into cross sections corresponding to the phase space in which the samples are generated, which are then used to normalize the samples to the correct luminosity. The electroweak process has predicted fiducial cross sections of 1.00 ± 0.06 fb and 0.88 ± 0.05 fb in the inclusive and VBS regions, respectively. For the strong process, the corresponding cross sections are 0.35 ± 0.05 fb and 0.098 ± 0.018 fb. The uncertainties on these numbers account for uncertainties from several sources: PDFs, parton shower modeling, choice of renormalization and factorization scales, and the difference between cross sections calculated with POWHEGBOX and VBFNLO [77]. The derivation of these uncertainties is described in detail in Chapter 7. In the absence of a NLO calculation for the combined (both electroweak and strong production) $W^\pm W^\pm jj$ process, the effect of interference between electroweak $W^\pm W^\pm jj$ and strong $W^\pm W^\pm jj$ is determined at leading order with SHERPA by comparing the cross section of the combined process to the sum of the cross sections of the two sub-processes. Interference is found to increase the total cross section by 12 percent in the inclusive region and 7 percent in the VBS region. The prediction for the electroweak production of $W^\pm W^\pm jj$ is scaled up to include the contribution from interference, and the uncertainty on the interference component is taken to be 50%.

6.1.2 $W^\pm Z$

As for $W^\pm W^\pm jj$ production, the $W^\pm Z$ process is split into electroweak and strong production processes which are simulated separately and normalized to NLO cross sections in each fiducial region. SHERPA is again used for the event generation, and the fiducial cross sections are calculated using VBFNLO. Since VBFNLO cannot be interfaced with a parton showering program at NLO, the normalization is done at the parton level. The truth record in SHERPA is used to identify the products of the hard scatter, and only those objects are used to calculate the acceptance. By normalizing the samples this way, the effect of showering on the fiducial cross sections is taken directly from SHERPA.

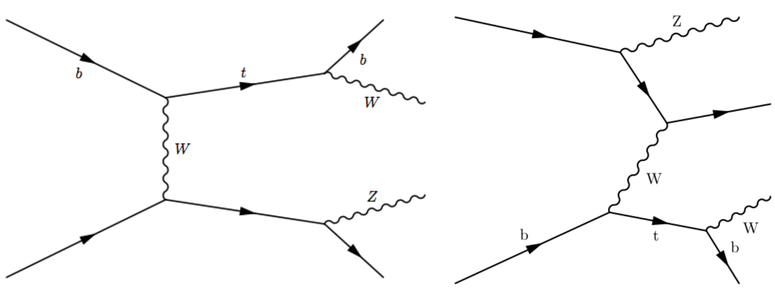

Figure 6.1: Representative diagrams for tZj production with the subsequent top decay yielding WZ plus two jets.

The normalization of the electroweak production of $W^\pm Z$ contains a further complication. This cross section receives a contribution from the associated production of a top quark with a Z boson and an additional parton, illustrated in Figure 6.1, where a W is produced in the top decay. This class of diagrams is neglected by VBFNLO due to the requirement of a b quark in the initial state, but they account for almost a third of events

≤ 1 jet Control Region				
	ee	$e\mu$	$\mu\mu$	Total
$W^{\pm}W^{\pm}$jj ewk+strong	2.72 ± 0.30	8.2 ± 0.8	4.2 ± 0.4	15.1 ± 1.5
OS prompt leptons	152 ± 17	24 ± 4	–	177 ± 21
WZ/γ*,ZZ	46 ± 8	130 ± 23	75 ± 13	251 ± 43
W+γ	39 ± 11	59 ± 17	0.04 ± 0.04	98 ± 29
$t\bar{t}$+W/Z	0.34 ± 0.15	0.8 ± 0.4	0.56 ± 0.25	1.7 ± 0.7
Other non-prompt	38 ± 15	65 ± 26	8 ± 5	111 ± 30
Total Predicted	278 ± 28	288 ± 42	88 ± 14	654 ± 69
Data	288	328	101	717

Table 6.1: Event counts in the ≤ 1 jet control region.

populating the fiducial regions. To account for this, a new normalization is derived by splitting the sample into events that contain a b quark in the initial state and events without an initial b quark. The formula for the cross section used to normalize the SHERPA sample is:

$$\sigma_{norm} = \sigma_{fid}^{\text{VBFNLO}} / A_{ME}^{without-b} + \sigma^{\text{SHERPA}} \times f_b \tag{6.1}$$

where $\sigma_{fid}^{\text{VBFNLO}}$ is the fiducial cross section calculated using VBFNLO, $A_{ME}^{without-b}$ is the parton-level acceptance of the SHERPA subsample without any b quarks in the initial state, σ^{SHERPA} is the total sample cross section calculated with SHERPA, and f_b is the fraction of generated events that contain a b quark in the initial state. In this way, the "without-b" subsample is normalized to the VBFNLO cross section while the SHERPA cross section is used for the "with-b" subsample.

Predictions for the $W^{\pm}Z$ background are tested in two control regions (CRs), referred to as the ≤ 1 jet CR and the tri-lepton CR. The ≤ 1 jet CR is defined by inverting the signal region selection on jet multiplicity to accept only events with fewer than two jets. Subsequent selections on jet-based quantities are also dropped. This region is used to test the modeling of lepton kinematics in events where one of the leptons from the Z decay is not reconstructed. Figure 6.2 shows lepton p_{T} and η distributions for the $e\mu$ and $\mu\mu$ channels (the ee channel is dominated by conversion background, to be discussed in Section 6.2). The number of data events in this control region is shown in Table 6.1. Good agreement is observed between the data and the prediction.

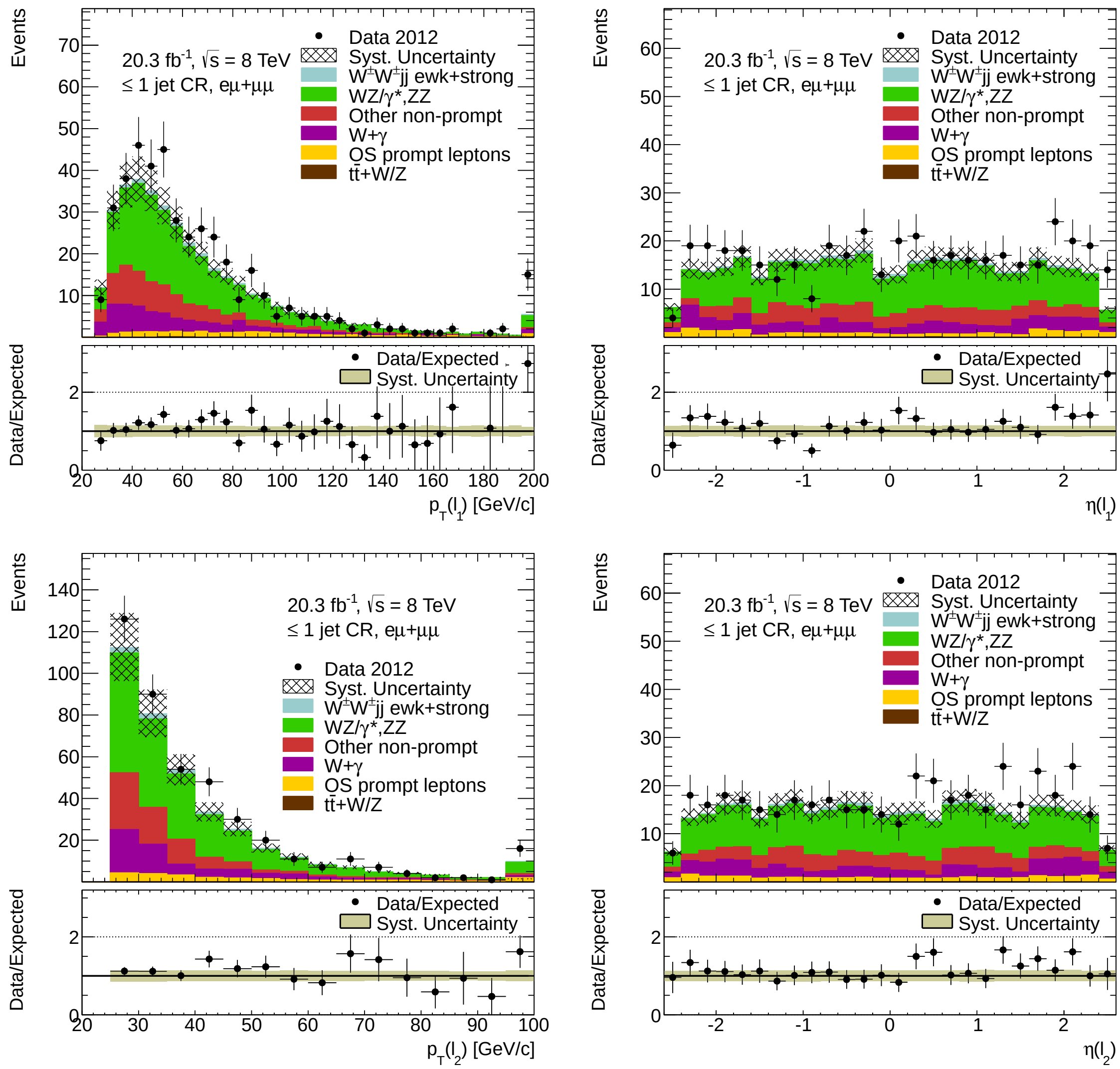

Figure 6.2: Lepton p_{T} (left) and η (right) distributions for the leading (top) and sub-leading (bottom) leptons for $e\mu$ and $\mu\mu$ events in the ≤ 1 jet control region.

Tri-lepton Control Region				
	$e^{\pm}e^{\pm}\ell^{\mp}$	$e^{\pm}\mu^{\pm}\ell^{\mp}$	$\mu^{\pm}\mu^{\pm}\ell^{\mp}$	Total
$W^{\pm}W^{\pm}$jj ewk+strong	0.01 ± 0.01	0.11 ± 0.02	0.00 ± 0.00	0.12 ± 0.02
WZ/γ^{*}	32 ± 5	96 ± 16	57 ± 10	186 ± 31
$ZZ\rightarrow$4l	2.2 ± 0.6	5.3 ± 1.3	1.8 ± 0.5	9.2 ± 2.1
Non-prompt	0.48 ± 0.32	6 ± 5	0.00 ± 0.00	7 ± 5
$t\bar{t}+W/Z$	0.65 ± 0.28	2.4 ± 1.0	1.0 ± 0.5	4.1 ± 1.7
Total Predicted	36 ± 6	110 ± 18	60 ± 10	206 ± 33
Data	40	104	48	192

Table 6.2: Event counts in the tri-lepton control region.

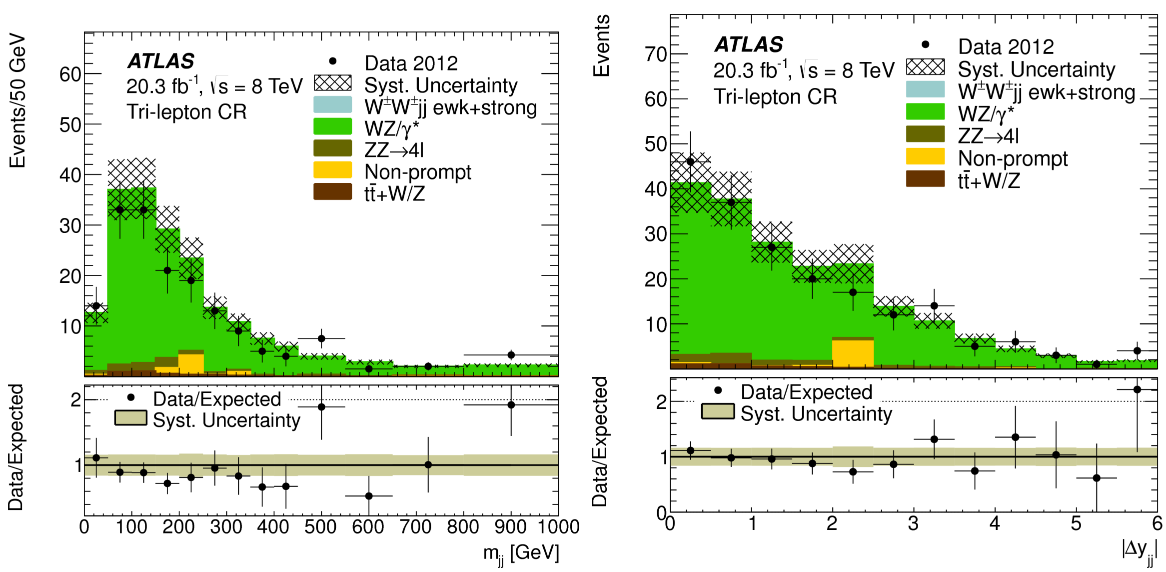

Figure 6.3: Di-jet invariant mass distribution (left) and rapidity difference distribution (right) for events in the tri-lepton control region.

The tri-lepton CR is defined by inverting the third lepton veto. Events containing a fourth lepton passing the veto lepton definition are still rejected. Since the $W^{\pm}Z$ process contains an electroweak component that is sensitive to the same aQGCs that affect $W^{\pm}W^{\pm}jj$, the m_{jj} and $|\Delta y_{jj}|$ selections are dropped. This region provides a test of the modeling of jet kinematics in the $W^{\pm}Z$ MC. Event counts are shown in Table 6.2, and the m_{jj} and $|\Delta y_{jj}|$ distributions are shown in Figure 6.3. A slight excess is visible in the tail of the m_{jj} distribution with a statistical significance of 1.9σ if a cut is placed at m_{jj} >500 GeV. As previously mentioned, this region is not a good control region because event counts here would be enhanced by the same anomalous couplings that would enhance rates in the signal regions. Nonetheless, many distributions were checked for evidence of mismodeling of event kinematics. No evidence of mismodeling was found, and the excess is attributed to a statistical fluctuation.

6.1.3 Other Prompt Backgrounds

$W^{\pm}Z$ production accounts for about 90% of the prompt background. Other sources of prompt same-sign leptons include the associated production of a $t\bar{t}$ pair and a W or Z, $ZZjj$ production, and multiple parton interactions (MPI) where each interaction contributes some of the leptons/jets (e.g. $W^{\pm}j + W^{\pm}j$). $t\bar{t}V$ $(V = W, Z)$ events are generated with MADGRAPH [78] and showered with PYTHIA8. $ZZjj$ is simulated using SHERPA. Several MPI processes capable of producing two same-sign leptons and two jets are simulated with PYTHIA, and this contribution is found to be negligible.

6.2 Background from Photon Conversions

6.2.1 Charge Misidentification

Events that contain two prompt opposite-sign leptons can enter the signal regions if the charge of one of the leptons is misidentified. The dominant mechanism for charge misidentification ("charge misID") of electrons is the"trident" process, shown in Figure 6.4, in which the prompt electron radiates an energetic photon that subsequently converts into an e^+e^- pair. The rate of charge misID in combined muons has been found to be negligible and is therefore not considered in this analysis. Events entering the signal regions due to charge misID consist mainly of fully leptonic $t\bar{t}$ decays and Drell Yan lepton pair production according to simulation. However, this background is estimated using a data-driven technique.

First, the rate of charge misID is measured in a data sample enriched in $Z \to ee$ events. This sample is selected by looking for two tight electrons with a di-lepton invariant mass ($m_{\ell\ell}$) between 70 GeV and 100 GeV, with no requirement made on the lepton charges. An asymmetric window around the Z mass is used account for energy lost to the soft electrons that are not reconstructed when the trident process causes an electron's charge to be misidentified. Contributions to this region from other processes are estimated and subtracted using the sidebands of 40 GeV$< m_{\ell\ell} <$70 GeV and 100 GeV$< m_{\ell\ell} <$130 GeV. The size of the subtraction is less than 1% of the total number of events.

A likelihood fit is used to measure the charge-misID rate as a function of p_{T} and η, taking into account that either electron in a same-sign pair could be the misidentified one. The number of total events and same-sign events are counted in bins of p_{T} and η, and charge-misID rates are chosen for each bin in order to maximize a Poisson-based likelihood given the observed counts:

$$ln(\mathcal{L}(\epsilon|N, N_{SS})) = \sum_{i,j} N_{SS}^{i,j} ln(N^{i,j}(\epsilon^i + \epsilon^j)) - N^{i,j}(\epsilon^i + \epsilon^j) \tag{6.2}$$

where N is the total number of events, N_{SS} is the number of same-sign events, ϵ is the charge-misID rate, and the superscripts i and j refer to the η/p_{T} bin of the first and second electron, respectively. Charge-misID rates are shown in Figure 6.5. Since the rates for bremsstrahlung and photon conversion depend on the amount of material traversed, the rate for charge misID exhibits a strong η dependence. This likelihood assumes that the probability to obtain a same-sign event is $\epsilon^i + \epsilon^j$, which ignores the possibility that both electrons have their charge misidentified. This is justified by the low charge-misID rate, which is a few tenths of a percent over most of the η range and is still only about 2% near $|\eta|$ =2.5.

The measured charge-misID rate is used to predict the amount of background from charge misID by weighting opposite-sign events. Data events are selected using all of the signal region criteria except that the requirement that the leptons have the same charge is changed to require opposite charges. Then, for each electron in the event, a charge-misID event is added to the background estimation, weighted by the charge-misID rate in the η/p_{T} bin corresponding to that electron. This accounts for the ambiguity in the ee channel as to which electron had its charge misidentified.

In addition to the rate of charge misID, an energy correction is determined using $Z \to ee$ MC. For each electron, the difference between the true

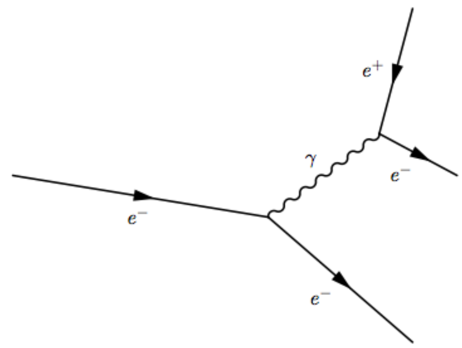

Figure 6.4: Illustration of the “trident” process. If most of the energy of the original e^- ends up with the e^+, it is likely that only the e^+ will be reconstructed. Since the momentum of this lepton is very similar to that of the original prompt lepton, this is referred to as charge misidentification.

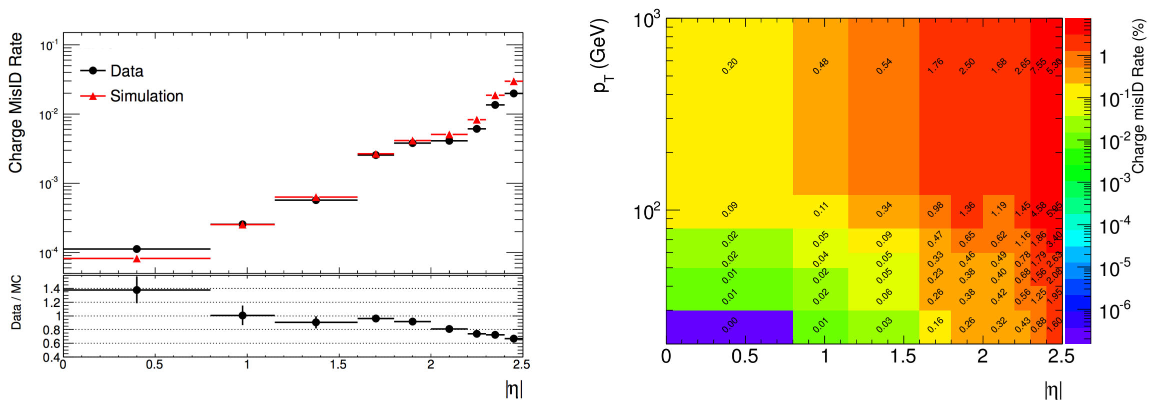

Figure 6.5: Charge-misID rates derived for electrons as a function of $|\eta|$ (left) and as a function of both $|\eta|$ and p_{T}.

energy and the reconstructed energy is obtained by matching reconstructed electrons to the original prompt electron in the MC truth record. The distribution of this energy difference is shown in two η bins in Figure 6.6 for reconstructed electrons that have the same/opposite charge as the original prompt electron. The difference in the mean of these distributions is used to correct the energy of an electron in a charge-misID event, and the quadrature difference in resolution is used to apply a Gaussian smearing to the energy of these electrons. These energy corrections are shown as a function of $|\eta|$ in Figure 6.7. The invariant mass distribution of same-sign di-electron events, shown in Figure 6.9, is used to further calibrate the energy corrections. The size of the energy shift is increased by 35%, and the smearing is increased by 25% to make the predicted Z peak agree with data. These energy corrections are applied before kinematic selections to allow for migration into or out of the signal regions.

Charge misID (denoted "OS prompt leptons" in tables and figures) provides the main source of background for events with two same-sign electrons prior to the m_{jj} >500 GeV selection. The ee channel of the ≤ 1 jet CR is used to test the predicted rate and lepton kinematics. Figure 6.8 shows the η distributions for electrons in this region. The agreement observed in these distributions validates the measured charge-misID rates. Derivation of systematic uncertainties for this background estimate is discussed in Chapter 7. The total uncertainty varies between 15% and 30% depending on region and channel and comes mainly from a comparison of predicted and observed counts of same-sign di-lepton events in $t\bar{t}$ MC.

6.2.2 $W^{\pm}\gamma$

Events with a W boson and on-shell photon can produce same-sign leptons if the photon converts in the detector and one of the leptons is not reconstructed. $W^{\pm}\gamma$ production can be separated into strong and electroweak processes, which are estimated using ALPGEN [79]+HERWIG/JIMMY [80, 81] and SHERPA, respectively. The uncertainty on the total cross section (strong + electroweak) is taken to be 17% following a measurement of this cross section in $\sqrt{s}$ =7 TeV collisions [17]. A comparison of charge-misidentification rates measured in data and MC is used to test the modeling of the conversion rate vs. η since the emission and subsequent conversion of a photon is the dominant mechanism for charge misID. Observed differences are translated into an uncertainty on the $W^{\pm}\gamma$ yield as described in Chapter 7.

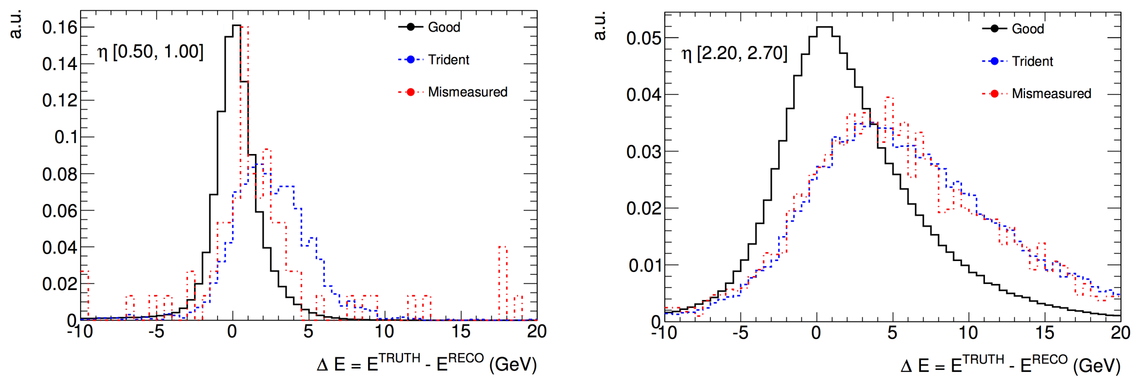

Figure 6.6: Difference between true energy and reconstructed energy for electrons reconstructed with the correct charge (black), electrons reconstructed with the wrong charge due to the trident process (blue), and electrons reconstructed with the wrong charge when no trident was evident in the MC truth record (red).

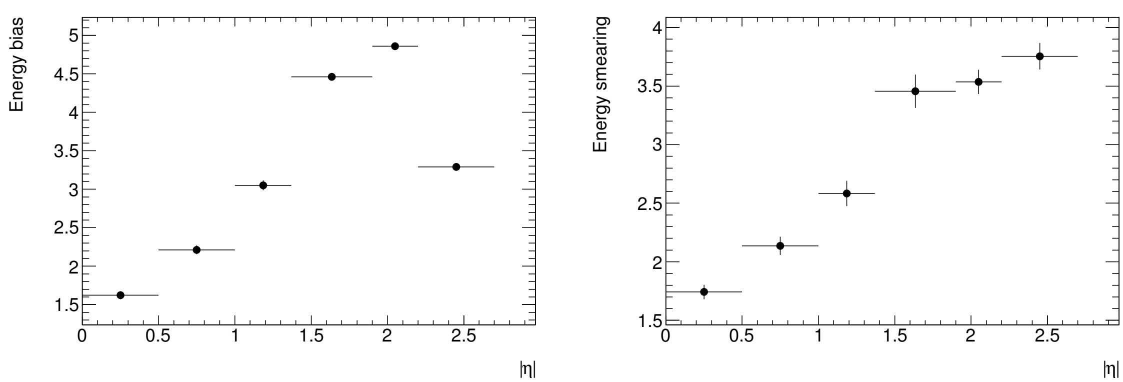

Figure 6.7: Energy bias (left) and smearing (right) corrections in units of GeV derived using $Z \to ee$ MC.

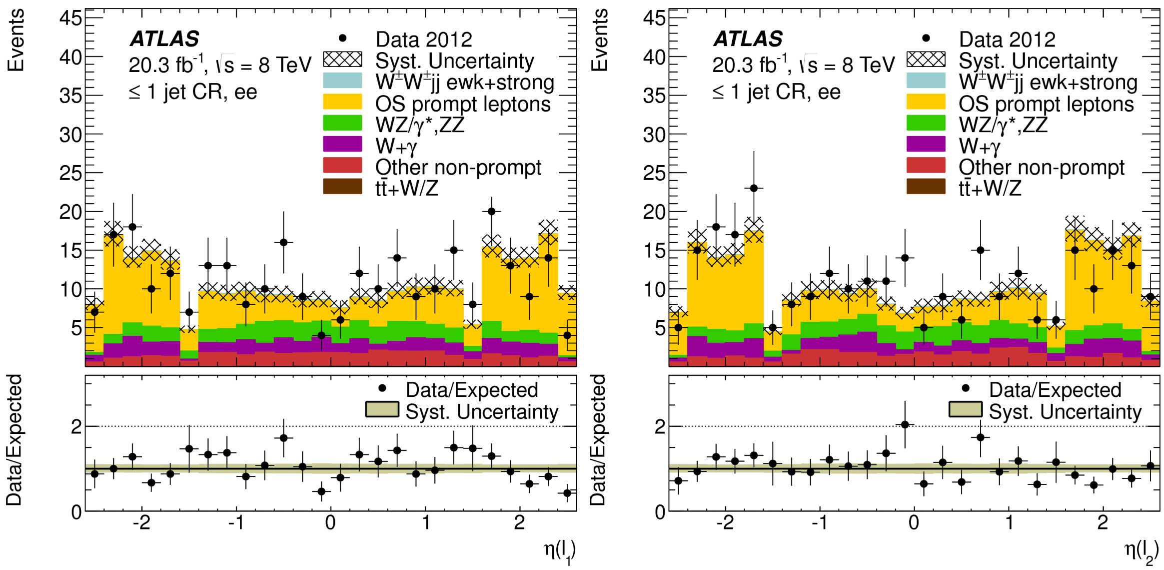

Figure 6.8: Electron η distributions for the leading (left) and sub-leading (right) electrons in the ≤ 1 jet control region.

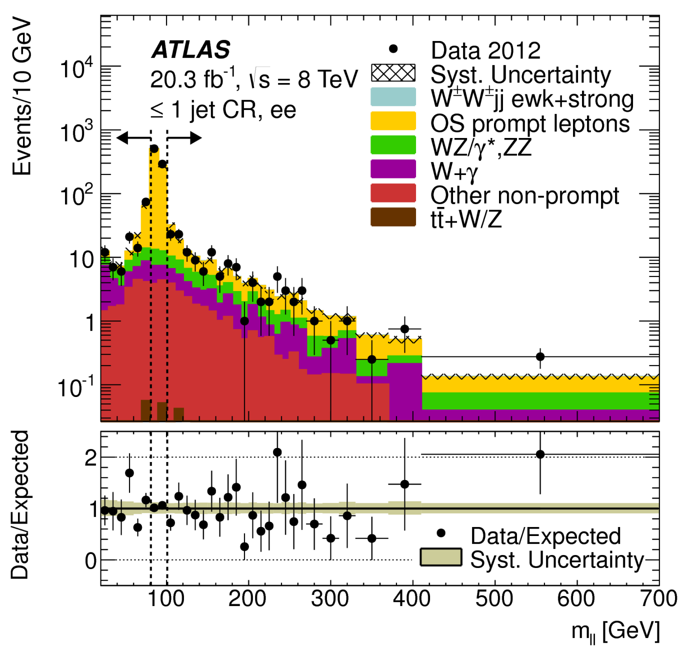

Figure 6.9: Di-electron invariant mass distribution for events in the ≤ 1 jet control region.

6.3 Other Non-prompt Background

Non-prompt background in which one or both leptons come from hadron decays or hadrons misidentified as leptons is estimated using a data-driven method. In a manner similar to the estimation of the charge-misID background, a rate for an isolated lepton to result from hadronic activity is measured from data in a control region enriched in such events, and this rate is applied to data in regions very similar to the signal regions in order to predict the non-prompt background. A "tight + loose" (TL) region used to predict this background is defined by requiring one of the leptons to pass the loose selection instead of the tight selection. Since the loose leptons are non-isolated, the vast majority of them come from hadronic activity. The small contribution from prompt leptons is subtracted using MC. To obtain the number of events that enter the signal region with two tight leptons, events in the TL region are weighted by a "fake factor."

The fake factor used is the ratio of the number of tight leptons to the number of loose leptons measured from data in a region where both tight and loose leptons come predominantly from hadrons. This analysis uses a "di-jet" region which requires one lepton and one jet, each with p_{T} greater than 25 GeV, with additional kinematic selections to pick out events that are likely to be misreconstructed di-jet events. The transverse mass formed using the lepton and $E_{\mathrm{T}}^{\mathrm{miss}}$ is required to be less the 40 GeV, and $\Delta\phi(\ell, j)$ must be greater than 2.8. Figure 6.10 shows the transverse mass distribution for events with a tight lepton after all other cuts have been applied. The remaining contribution from processes with prompt leptons, which comes mainly from W+jets and Z+jets, is estimated using MC and subtracted. This prompt contamination accounts for about half of the events with a tight lepton.

The single leptons triggers used for the analysis have isolation requirements for low-p_{T} leptons and cannot be used to select an event with a single non-isolated lepton. Therefore, different triggers are used to select the di-jet sample. Electron plus jet events are selected using a trigger that looks for calorimeter clusters with energy greater than 20 GeV that passes loose electron identification requirements. Muon + jet events are selected using a trigger similar to the nominal single muon trigger but with no isolation requirements. Due to the track quality requirements in this trigger and the loosened impact parameter requirements of the loose muon selection, this trigger is still expected to have some inefficiency for loose muons with respect to tight muons. The efficiency of the trigger for each type of muon was compared using a tag-and-probe method and found to be 10% higher

b-tag Control Region				
	ee	$e\mu$	$\mu\mu$	Total
$W^{\pm}W^{\pm}$jj ewk+strong	0.81 ± 0.10	2.57 ± 0.28	1.55 ± 0.18	4.9 ± 0.5
OS prompt leptons	22 ± 5	27 ± 6	–	49 ± 11
$t\bar{t}$+W/Z	7.1 ± 3.1	18 ± 8	11 ± 4	36 ± 15
WZ/γ^*,ZZ	2.3 ± 0.5	4.9 ± 0.9	2.2 ± 0.4	9.4 ± 1.6
W+γ	1.7 ± 0.7	2.3 ± 0.9	–	4.0 ± 1.4
Other non-prompt	6.7 ± 2.5	20 ± 8	10 ± 5	37 ± 10
Total Predicted	40 ± 6	75 ± 13	25 ± 7	140 ± 22
Data	46	82	36	164

Table 6.3: Event counts in the b-tag control region.

for tight muons. This difference is applied as a correction to the measured fake factor.

The probability for a non-prompt lepton to be isolated depends on the kinematics of both the lepton and the jet that gave rise to that lepton (the "underlying jet"). The first dependence is taken into account by binning the fake factor in lepton p_{T} and $|\eta|$, as shown in Figure 6.13, but the second is more difficult to deal with since the underlying jet is usually not reconstructed. In the di-jet region used to measure the fake factor, the p_{T} of this jet can be inferred from the p_{T} of the jet on the opposite side. Events in this region are used to derive a relationship between lepton p_{T} + $E_{\mathrm{T}}^{\mathrm{iso}}$ and the average p_{T} of the underlying jet. Average jet p_{T} as a function of lepton p_{T} + $E_{\mathrm{T}}^{\mathrm{iso}}$ is shown in Figure 6.11. This relationship is found to be linear and is applied to the loose leptons in events in the TL region to obtain the p_{T} distribution for underlying jets in those events. In order to increase statistics for this distribution, the m_{jj} and $|\Delta y_{jj}|$ cuts are not applied. Events in the di-jet region are then re-weighted so that the jet p_{T} distribution matches the distribution for underlying jets in the TL region. The effect of re-weighting the jet p_{T} distribution on the lepton isolation distributions is shown in Figure 6.12. After re-weighting, the isolation distribution for loose leptons in the di-jet region agrees much better with the TL region.

Since non-prompt leptons originate mainly from B hadron decays, the non-prompt prediction is tested in a b-tag CR, which is defined by inverting the b-jet veto to require the presence of at least one b-tagged jet. The m_{jj} and $|\Delta y_{jj}|$ selections are also dropped to increase statistics. Event counts for this region are shown in Table 6.3. Transverse momentum distributions for

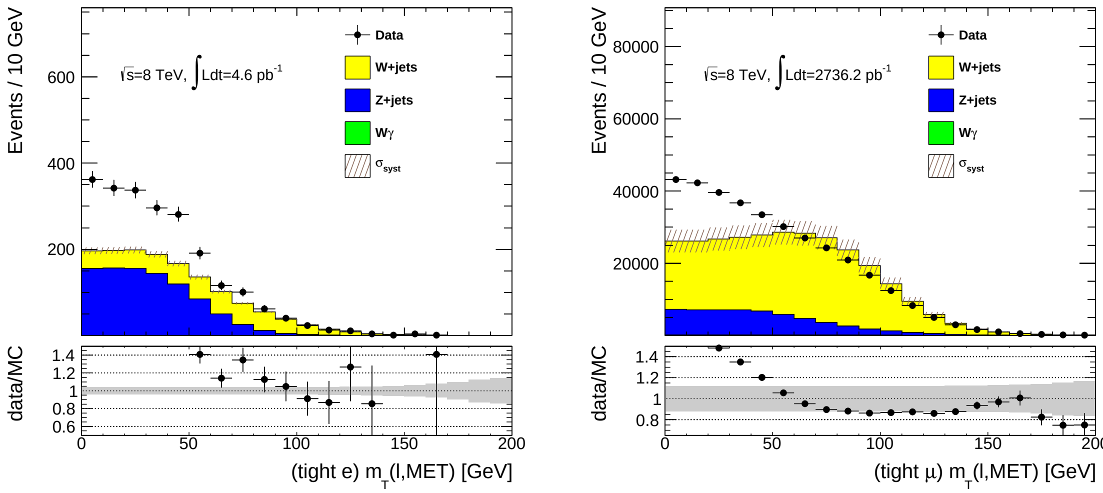

Figure 6.10: $m_{\mathrm{T}}(\ell, E_{\mathrm{T}}^{\mathrm{miss}}$ distribution for events with a tight electron (left) or muon (right) after all other di-jet selections have been applied.

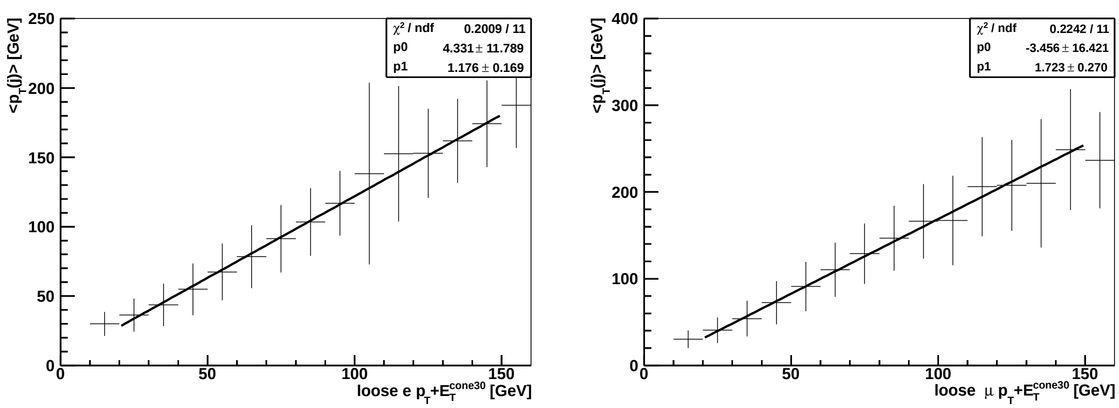

Figure 6.11: Average p_{T} of the jet vs. loose lepton $p_{\mathrm{T}} + E_{\mathrm{T}}^{\mathrm{iso}}$ for events passing the di-jet selection.

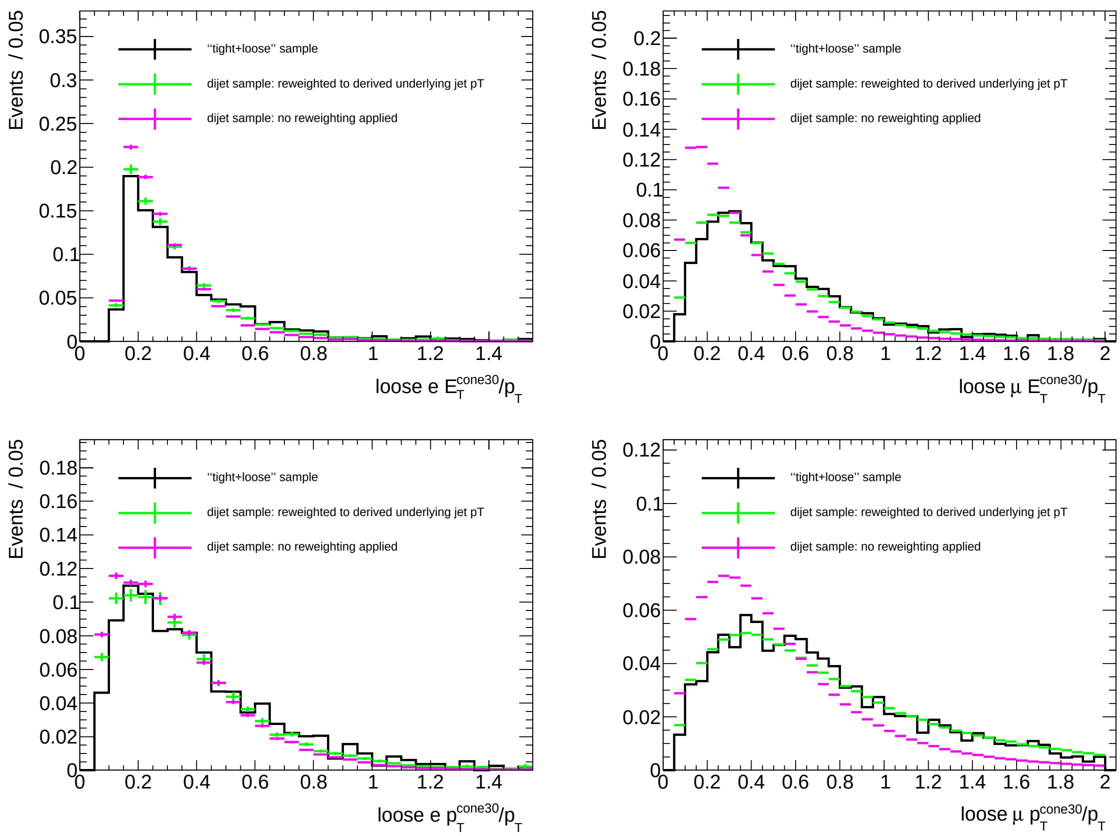

Figure 6.12: $E_{\mathrm{T}}^{\mathrm{iso}}$ (top) and $p_{\mathrm{T}}^{\mathrm{iso}}$ (bottom) as fractions of lepton p_{T} for loose electrons (left) and muons (right). The black curve shows the distribution for the TL region while the pink and green points show the distribution for the di-jet region before and after re-weighting.

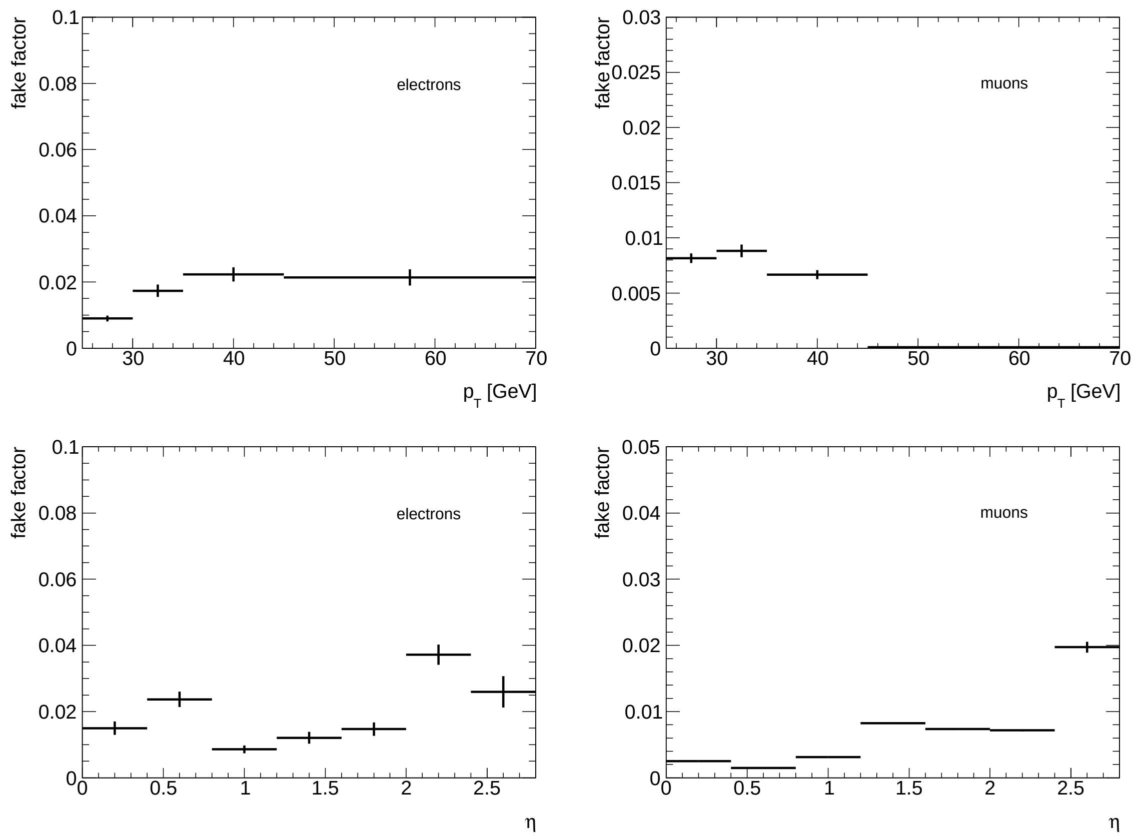

Figure 6.13: Fake factors as a function of lepton p_T (top) and $|\eta|$ (bottom) for electrons (left) and muons (right).

the leading and sub-leading leptons are given in Figure 6.14. Uncertainties on the non-prompt prediction vary from 35% to 50% depending on channel and are mainly due to contamination from prompt leptons in the di-jet region and the jet p_{T} re-weighting. These will be discussed in detail in Chapter 7.

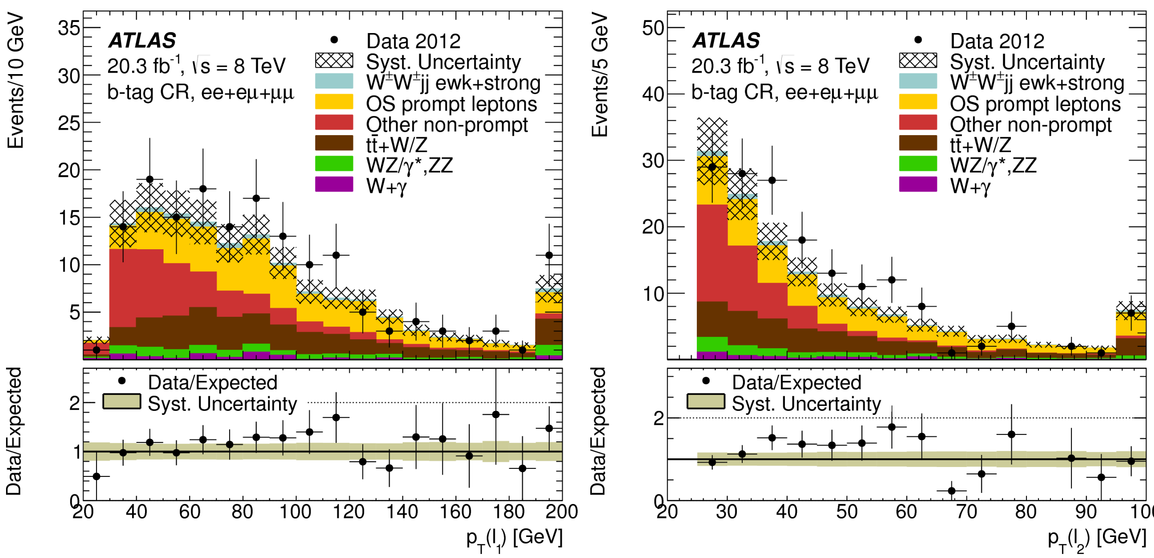

Figure 6.14: Lepton p_{T} distributions for the leading (left) and sub-leading (right) leptons in the b-tag control region.

Chapter 7

Systematic Uncertainties

Estimates of background and signal yields in the signal regions have several sources of systematic uncertainty. For MC-based predictions, these sources can be grouped into two categories: theoretical uncertainties on the cross section used to normalize the Monte Carlo, and uncertainties on correction factors applied to make reconstructed objects in MC more accurately match the data. None of these systematic uncertainties apply to backgrounds that are estimated using data-driven techniques. For these backgrounds, the uncertainty comes mainly from the purity of the data sample and the extrapolation to the signal region.

7.1 Uncertainties due to Theoretical Modeling

Together, $W^{\pm}W^{\pm}jj$ and $W^{\pm}Zjj$ make up about three quarters of the total predicted events in the signal regions, so a good understanding of the uncertainties on their cross sections is needed in order to compare the prediction with data. Sources of uncertainty common to these processes include the uncertainty on the parton distribution functions of the proton, the dependence of the calculated cross section on the choice of renormalization and factorization scales, and the dependence of event kinematics on the showering model. The total uncertainties for these four diboson processes are summarized in Table 7.1.

Parton distribution functions are not known from first principles and must be measured from fits to collider data as described in Chapter 2. Uncertainties on PDF parameters from these fits translate into uncertainties on cross sections predicted using these PDFs. PDF uncertainties are evaluated by repeating the cross section calculation several times using alternate

PDFs with parameters varied up or down by their 90% C.L. intervals. The differences between the cross sections obtained using the alternate PDFs and the central value are then summed in quadrature and scaled down to obtain 68% C.L. uncertainties. Assuming the systematic uncertainty follows a Gaussian distribution, this scale factor is 1.645. Scale uncertainties are derived by independently varying the renormalization and factorization scales by a factor of 2 in either direction. The two cases where one scale has been halved and the other doubled are excluded, and the spread in cross section among the remaining variations is used as the uncertainty due to higher order QCD corrections. Two models for simulating parton showers are compared. PYTHIA uses p_{T} ordering, it generates QCD radiation in order of descending p_{T} until reaching the scale of confinement, while HERWIG++ generates radiation in order of decreasing emission angle. Fiducial cross sections are obtained using each model, and the difference is taken as an uncertainty.

The use of different NLO generators for $W^{\pm}W^{\pm}jj$ and $W^{\pm}Zjj$ was made necessary by the fact that neither generator had an NLO calculation available for all 4 process. The only process to be implemented in both was the electroweak production of $W^{\pm}W^{\pm}jj$. The predictions of the two generators for this process were compared and found to agree within 5%. The difference between them is taken as an uncertainty on the $W^{\pm}W^{\pm}jj$ cross sections.

The electroweak production of $W^{\pm}Zjj$ has a large additional uncertainty due to the tZj component, which is missing from VBFNLO. This component is estimated at LO using SHERPA, and a 50% uncertainty is taken. This translates to a 20% uncertainty on the total electroweak $W^{\pm}Zjj$ cross section and is the dominant systematic uncertainty for this process. However, the effect on the total $W^{\pm}Zjj$ uncertainty is very small due to the dominance of strong production.

The strong production of $W^{\pm}Z$ + jets is unique among these processes in that there exist diagrams with zero or one jet in the final state. This process therefore receives an additional contribution from $W^{\pm}Z$ + 1 jet events where a second jet is produced from the parton shower. The uncertainty of this component is estimated using a LO MADGRAPH $W^{\pm}Z$ + 1 parton sample. This sample is then showered with both PYTHIA8 and HERWIG++, and the difference is taken as an uncertainty. The resulting uncertainty on the $W^{\pm}Zjj$ cross section is 6%.

The uncertainty on strong $W^{\pm}\gamma$ production is derived from the uncertainties on the 2-jet and 3-jet bins of a $\mathrm{d}\sigma_{W\gamma}/\mathrm{dN_{jets}}$ measurement performed by ATLAS using 7 TeV data [17] as well as the uncertainty on the inclusive

Theoretical uncertainties (%)				
Region	$W^{\pm}W^{\pm}jj$ ewk	$W^{\pm}W^{\pm}jj$ strong	$W^{\pm}Zjj$ ewk	$W^{\pm}Zjj$ strong
Inclusive SR	6	14	23	16
VBS SR	6	18	27	12

Table 7.1: Total theoretical uncertainties for the $W^{\pm}W^{\pm}jj$ and $W^{\pm}Zjj$ processes in the Inclusive and VBS signal regions (SR).

cross section from the same measurement. The resulting uncertainty is 17%. A 100% uncertainty is taken on the electroweak component. Uncertainties on $t\bar{t}V$ production due to PDF uncertainties and scale choice have been previously studied [82], and a conservative uncertainty of 30% is assigned. Unlike, $W^{\pm}W^{\pm}jj$ and $W^{\pm}Zjj$, $ZZjj$ is only estimated at leading order. Its uncertainty is estimated assuming that it has a similar ratio of NLO to LO cross sections and similar scale/PDF uncertainties to the other diboson processes. The total estimated uncertainty for $ZZjj$ production is 19%.

7.2 Systematic Uncertainties from Object Reconstruction/Identification

Another source of uncertainty on MC-based prediction comes from the simulation on the interaction between particles produced in a proton-proton collision and the detector. Each reconstructed object has some uncertainty on its energy scale and resolution. If it has been required to pass some particle identification, there is also an uncertainty associated with the efficiency of these selections. The uncertainties affecting this measurement are listed below. In order to estimate the effect of these per-object uncertainties on the event yield in the signal regions, the analysis is repeated twice for each source of uncertainty, with that parameter varied up or down by its uncertainty. The difference between the event yields with the variation and the nominal yield is taken as the uncertainty due to that parameter. The contributions from different sources of uncertainty vary by process, but their relative importance can be seen in Tables 7.9 and 7.10.

- Jet energy scale/resolution (JES/JER): separate variations for light-flavor and heavy-flavor jets
- Jet vertex fraction cut efficiency

- Jet b-tag inefficiency
- Electron energy scale/resolution
- Muon momentum scale/resolution
- Electron identification efficiency
- Muon identification efficiency
- Identification efficiency for leptons passing the "veto" selection
- Single lepton trigger efficiencies
- $E_{\mathrm{T}}^{\mathrm{miss}}$ scale/resolution
- Energy scale of clusters not associated with reconstructed objects

7.2.1 Jet Uncertainties

The jet energy scale and its uncertainties are estimated using a variety of in situ techniques that use an object recoiling off of a jet as a reference for the true p_{T} of the jet [83]. Z+jet and γ+jet events are used for central jets while di-jet events for forward jets. Studies of JES performance using Z+jet events are discussed in more detail in Chapter 8. For jets with p_{T} greater than 1 TeV, uncertainties are estimated from events where a high-p_{T} jets recoils against multiple low-p_{T} jets and from the calorimeter response to single hadrons measured using test-beam data and minimum bias collisions. Figure 7.1 shows these uncertainties for different η and p_{T} ranges.

Additional uncertainties are estimated for specific effects, including corrections for pileup, close-by jets, at the type of parton that initiated the jet. The effects of pileup are studied by examining the dependence of the reconstructed jet p_{T} on the number of reconstructed primary vertices and on the average number of interactions per bunch crossing. The reconstructed p_{T} can be compared to either the true p_{T} in MC or the p_{T} of a recoiling object. The difference in the corrections derived using each reference is taken as an uncertainty and ranges from about 0.5% to 1.5% per vertex/interaction depending on jet p_{T} and η.

An uncertainty due to close-by jets is evaluated by comparing the ratio of reconstructed jet p_{T} to the p_{T} of an associated track jet, a jet clustered using tracks instead of calorimeter clusters, for isolated and non-isolated jets. A jet is considered isolated if the distance in (η, ϕ) space to the nearest other jet is greater than 2.5 times the radius parameter used to cluster the

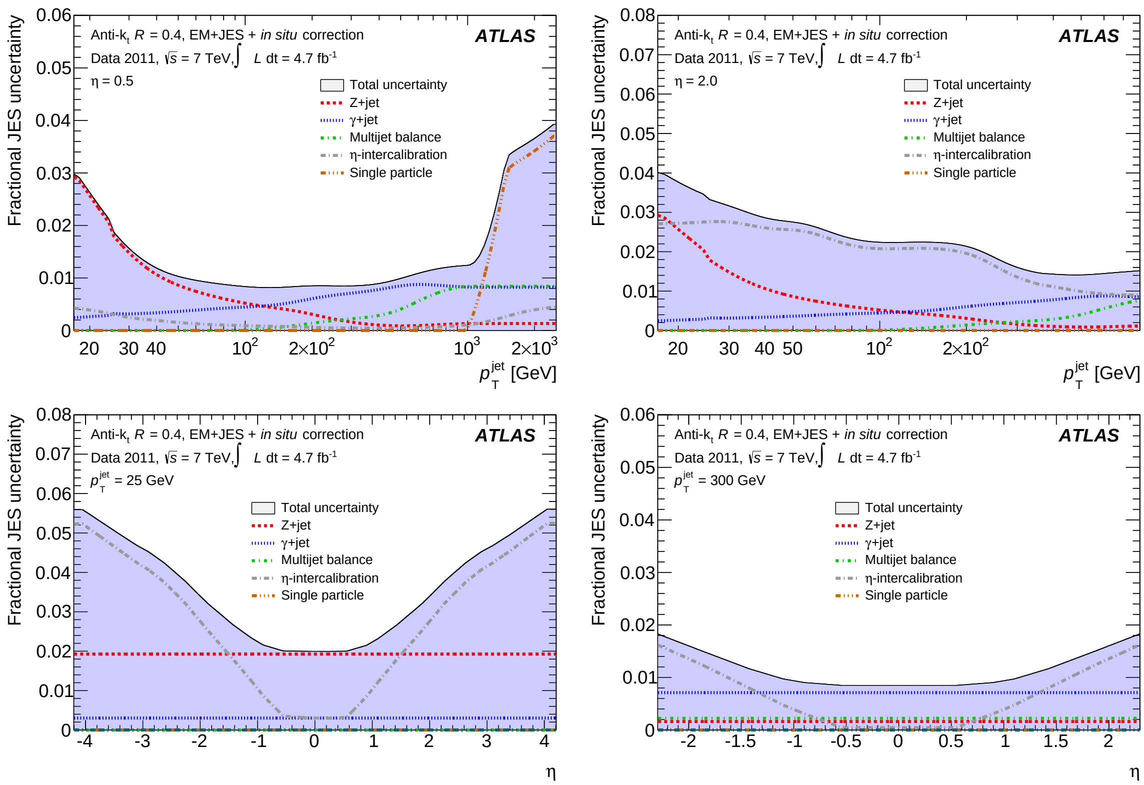

Figure 7.1: Relative uncertainty on in situ JES corrections as a function of p_T (top) for jets with $|\eta|$ around 0.5 (left) and 2.0 (right) and as a function of η (bottom) for jets with p_T near 25 GeV (left) and 300 GeV (right). Figure taken from Ref. [83].

jets. This comparison is made for both data and MC, and the fractional difference is taken as the uncertainty due to close-by jets. This uncertainty is about 3.5% for 30 GeV jets with another jet within a distance of 0.5 and decreases with increasing distance to the nearest jet and increasing jet p_{T} .

Differences in physical characteristics, like the average number of charged particles and average jet width, between jets initiated by a quark or by a gluon can be used to construct a tagging algorithm for separating quark jets from gluon jets. The dependence of the jet energy scale on the operating point of the tagger (corresponding to different purities of the tagged sample) is compared between data and MC, and the difference is taken as an uncertainty due to jet flavor and ranges from 1% to 3% depending on jet p_{T} and whether the sample is dominated by gluon jets or quark jets.

Uncertainties from the in situ calibrations are the dominant contribution to the total uncertainty for jets with high p_{T} or high η, which is expected for events passing the signal region selections. Below 50 GeV, uncertainties from close-by jets and pileup become important, and the uncertainty due to jet flavor is largest for jets with $|\eta| < 1$. When propagated through the analysis, the resulting uncertainty on the event yield is 10-15% for background and 6% for signal.

Events with a jet recoiling against a high-p_{T} ($>$ 30 GeV) Z boson are also used to measure the efficiency of jets originating from the primary vertex to pass the JVF selection [63]. Z+jet events are used to obtain a sample of jets with little contamination from pileup. The difference between the efficiency observed in data and MC is about 1% and is taken as an uncertainty. Variations of the JVF selection around the nominal value that change the efficiency in MC by this difference are used to propagate the uncertainty to physics analyses. The effect of this uncertainty on the final predictions is less than 1%.

The efficiency for b-tagging jets is measured as a function of p_{T} using di-leptonic $t\bar{t}$ decays [84], which produces a sample of jets enriched in b jets. The uncertainty on the b-tagging efficiency is due mainly to the kinematic modeling of $t\bar{t}$ and background processes in MC. The relative uncertainty is less than 4% for jets with 30 GeV $< p_{\mathrm{T}} <$ 200 GeV and 8% for jets with p_{T} greater than 200 GeV. The rate for mistakenly tagging light-flavor jets (mis-tag rate) is measured in an inclusive jet sample by comparing the nominal rate of b tags to the rate when the signs of track impact parameters and secondary vertex decay length are reversed [66]. For jets with p_{T} below 140 GeV, the main source of uncertainty is the modeling of track multiplicity in jets while uncertainties on the efficiency to tag b and c jets form the dominant contribution for jets with p_{T} greater than 140 GeV. The total uncertainty on the mis-tag rate varies from 15-25% depending on jet p_{T} and η. Uncertainty on the b-tagging efficiency/mis-tag rate translates into an uncertainty on the signal region predictions of about 1%.

7.2.2 Lepton Uncertainties

The electron energy scale and resolution and their uncertainties are evaluated using $Z \to ee$ events [56]. Muon momentum scale and resolution corrections and their uncertainties are evaluated using $J/\psi \to \mu\mu$ and $Z \to \mu\mu$ events [58]. In both analyses templates of the invariant mass distribution of the lepton pair are constructed using MC with free parameters for scale and resolution corrections in bins of p_{T} and η. These parameters are then determined using a maximum likelihood fit to the invariant mass distribution observed in data. Uncertainties on the energy/momentum scale for leptons are less than 1%.

Identification efficiency scale factor and their uncertainties are also determined using Z boson decays to charged leptons [55, 58]. This measurement uses a tag-and-probe method in which one lepton (the tag) is required to pass all identification criteria and to form a Z candidate with a second object (the probe) that has not yet been required to pass identification. The efficiency of the ID selections is then determined using the sample of probe leptons in bins of p_{T} and η. Uncertainties on the efficiency are estimated by varying the event selections used to select Z decays. The impact of lepton energy and identification uncertainties on the predicted yields is 1-2% depending on channel. The tag-and-probe studies are also used to measure single-lepton trigger efficiencies. Again, the tag leptons are required to have fired the trigger, and the efficiency of the trigger requirements is evaluated on the probe leptons. The uncertainty from trigger efficiency is less than 1%.

7.2.3 $E_{\mathrm{T}}^{\mathrm{miss}}$ Uncertainties

Since missing transverse energy is evaluated using the measured transverse energies of other objects in the event, the uncertainties on those measured energies also affect the calculated $E_{\mathrm{T}}^{\mathrm{miss}}$. This effect is included when propagating these uncertainties to the predicted event yield. The remaining uncertainty on $E_{\mathrm{T}}^{\mathrm{miss}}$ comes from the energy scale and resolution of energy deposits in the calorimeter that are not part of another object (soft terms). Two methods are used to estimate the uncertainties due to soft terms, both of which use $Z \to \mu\mu$ events [68]. One compares the average $E_{\mathrm{T}}^{\mathrm{miss}}$ measured in data and MC for events without any jets, where the only contributions to $E_{\mathrm{T}}^{\mathrm{miss}}$ come from the muons and soft terms. The second estimates the true soft term contribution using truth information and compares this to the reconstructed soft term. The uncertainty from the soft term on the predicted event yield is about 2%.

7.2.4 Additional Uncertainties

In addition to the uncertainties listed above, there are a few other experimental uncertainties that affect MC-based predictions. In order to have a chance of correctly describing data, MC estimates must be normalized to match the integrated luminosity of the recorded data sample. Luminosity is measured using dedicated detector systems located at large pseudorapidities, and these measurements are calibrated with beam-separation scans similar to those described in Ref. [85]. Sources of uncertainties in the luminosity calibration include the measured product of the two bunch charges, jitter in the beam position, precision of lengths measured in the inner detector, emittance growth during the scans, and dependence on the number of interactions per bunch crossing. The estimated uncertainty of the luminosity of the data used for this measurement is 2.8%.

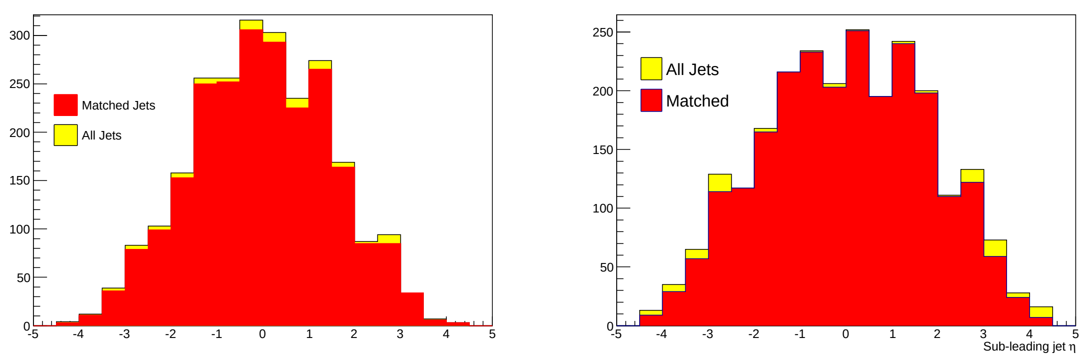

Figure 7.2: Jet η distributions for the leading (left) and sub-leading (right) jets in WZ MC. The yellow histogram contains all events while the red histogram contains only events in which both jets are matched to the primary interaction using truth information. The difference between the two is taken as a systematic uncertainty.

Event yields can also be affected by the presence of "pileup jets," jets that originate from additional proton-proton collision occurring within the same bunch crossing. For example, an event with only 1 jet may still pass analysis selections if a pileup jet is mistaken for another jet from the primary collision. To account for uncertainty from potential mismodeling of pileup interactions, MC truth record information is used to reject pileup jets, and the difference between the resulting event yield and the nominal one, shown in Figure 7.2 for WZ, is taken as an uncertainty. The effect is measured to be 8% in $W^{\pm}Z$ MC, and this is used as a common uncertainty for diboson processes that have fewer than 2 jets at leading order. For $W^{\pm}W^{\pm}jj$ and $t\bar{t}V$ production the effect is of order 1%.

The $W^{\pm}\gamma$ yield has an additional uncertainty due to the modeling of photon conversions in the detector. The extent of this uncertainty is evaluated using scale factors between charge-misID rates measured in data and MC. The discrepancy in charge-misID rates is a good proxy for the photon conversion rate since charge-misID occurs primarily due to the trident process depicted in Figure 6.4. Jet-based selections are relaxed to increase statistics, and two variations are performed using the charge-misID scale factors. First, scale factors are only applied if they are greater than 1 to obtain the maximum possible upward variation. This process is then repeated for scale factors less than 1. These variations are shown in Figure 7.3. This procedure avoids random cancelations between large and small scale factors to give a conservative estimate of the size of the effect. The resulting uncertainty is +22%/-13% on the $W^{\pm}\gamma$ yield.

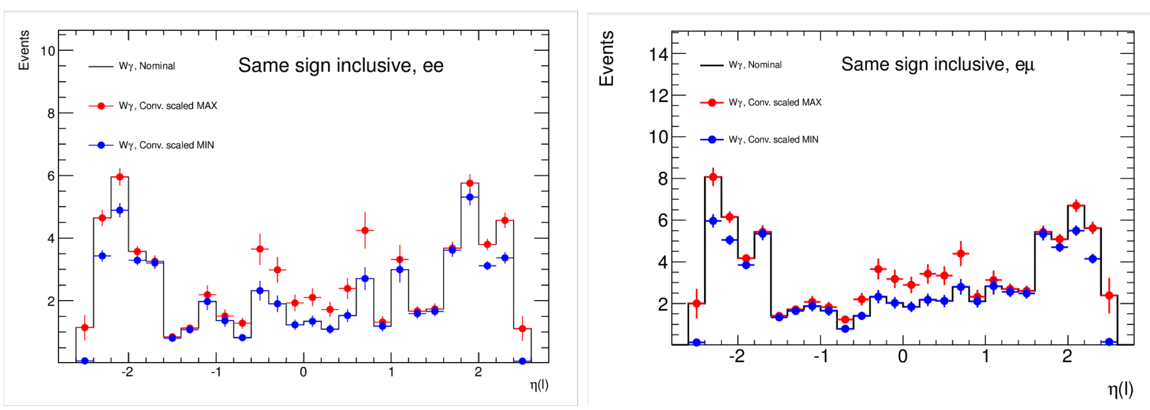

Figure 7.3: Electron η distribution for the ee (left) and $e\mu$ (right) channels. The red(blue) points show the effect of scaling events by charge-misID scale factors when those scale factors are greater(less) than one.

Uncertainties on charge-misID background (%)		
Source	Signal regions	Control regions
misID rate statistics	4.3	4.5
closure test	2.1	2.6
background subtraction	0.2	2
double-counting	+0, -2.5	+0, -0.2
energy corrections	+5.5, -3.1	+9.3, -6.2
Drell-Yan CR tests	6	6
Total	+9.4, -8.6	+12.4, -10.3
$t\bar{t}$ CR tests, ee channel	12	18(b-tag CR)/1(Others)
$t\bar{t}$ CR tests, $e\mu$ channel	31	20(b-tag CR)/11(Others)

Table 7.2: Summary of uncertainties on the charge-misID background. The final two rows indicate channel-specific uncertainties that are applied in addition to the uncertainty given in the "Total" row. This final uncertainty varies considerably depending on the fraction of the charge-misID background in a given region/channel that is expected to come from $t\bar{t}$ events.

7.3 Systematic Uncertainties on Data-Driven Background Estimates

7.3.1 Charge-misID Background

Uncertainties on the charge-misID background come from three areas: uncertainty on the charge-misID rate, uncertainty on the energy correction, and uncertainty from potential double-counting of charge-misID in processes that can produce both opposite-sign lepton pairs and same-sign lepton pairs without charge-misID. Uncertainties on the charge-misID rate come from limited statistics, a closure test of the method, background subtraction, and further tests of the method performed in Drell-Yan and $t\bar{t}$ MC. These uncertainties are summarized in Table 7.2.

The charge-misID rate is measured in a region that is dominated by $Z \rightarrow ee$ events and background from other processes is subtracted. Uncertainty from the background subtraction is estimated by measuring the charge-misID rate without background subtraction and evaluating the difference in the predicted yield between the two rates. For the closure test, the charge-misID rate is measured in $Z \rightarrow ee$ MC using the same method as for data, and the same sample of events is used to test the measured

Region Name	Charge-MisID (OS-scaled)	MC Same-sign Events	Ratio (difference/uncertainty)
SS Z	14780 ± 34	15650 ± 260	0.94 ± 0.02
Low N_{jet} CF	2026 ± 15	2038 ± 95	0.99 ± 0.05
VBF-like SS Z	447.4 ± 7.5	452 ± 43	0.99 ± 0.09
SS Incl.	1412 ± 10	1503 ± 76	0.94 ± 0.05
b-tag	1.7 ± 0.3	4.8 ± 3.9	0.35 (0.8σ)
Inclusive SR	1.77 ± 0.32	8.1 ± 8.1	0.2 (0.8σ)
VBS SR	1.06 ± 0.23	8.1 ± 8.1	0.13 (0.8σ)

Table 7.3: Test comparing the prediction from scaling opposite-sign events by the charge-misID rate to the direct same-sign prediction in Drell-Yan MC. The SS Z region inverts the Z veto used in the signal selection while making no cuts on jets, and the VBF-like SS Z region additionally requires two jets with $m_{jj} > 150$ GeV. The low N_{jet} CF region does not apply a Z veto but is otherwise similar to the ≤ 1 jet control region, and the SS Incl. region requires only two same-sign leptons with no further selections.

rate. Events passing the selections for the charge-misID rate measurement are separated into opposite-sign and same-sign events, and the charge-misID rate is applied to the opposite-sign events to get a prediction for the number of same-sign events. The discrepancy between the prediction and the actual number of same-sign events is taken as an uncertainty.

The applicability of this charge-misID rate to other regions and processes is examined by performing the same comparison of opposite-sign events scaled by the charge-misID rate to same-sign events in MC for several control regions and the two signal regions. This is shown for Drell-Yan MC in Table 7.3 and for $t\bar{t}$ MC in Table 7.4. The largest statistically significant difference seen using Drell-Yan MC is 6% and is taken as an uncertainty. However, this sample lacks sufficient statistics to make this comparison in the b-tag control region and in the signal regions, so $t\bar{t}$ MC is used to probe these regions. In the $t\bar{t}$ MC, the number of same-sign events is underestimated by 20% in the b-tag control region and 40% in the signal regions. To account for this discrepancy, MC is used to estimate relative size of the contributions of various processes to the charge-misID background, and the $t\bar{t}$ component is scaled up by 20% in the b-tag control region and 40% in the signal regions. The size of this scaling is then taken as an additional uncertainty on the prediction. In the signal regions, $t\bar{t}$ events are expected to account for about 30% of the charge-misID background in the ee channel and 80% in the $e\mu$

Region Name	Charge-MisID (OS-scaled)	MC Same-sign Events	Ratio (difference/uncertainty)
		ee channel	
b-tag	20.9 ± 0.2	26.6 ± 1.9	0.79 ± 0.06 (3.5σ)
Inclusive SR	0.57 ± 0.05	0.91 ± 0.39	0.63 ± 0.27 (1.3σ)
VBS SR	0.52 ± 0.04	0.91 ± 0.39	0.57 ± 0.25 (1.7σ)
		$e\mu$ channel	
b-tag	28.5 ± 0.3	33.1 ± 2.1	0.86 ± 0.06 (2.3σ)
Inclusive SR	0.65 ± 0.05	1.15 ± 0.43	0.57 ± 0.27 (1.6σ)
VBS SR	0.60 ± 0.05	0.95 ± 0.41	0.63 ± 0.25 (1.5σ)

Table 7.4: Test comparing the prediction from scaling opposite-sign events by the charge-misID rate to the direct same-sign prediction in $t\bar{t}$ MC.

channel.

The energy correction must be increased by 35% to make the same-sign di-electron mass distribution agree with data in the neighborhood of the Z mass. This change is taken as an uncertainty on the energy correction. In addition, energy corrections derived separately in Drell-Yan MC and $t\bar{t}$ MC differ by 15%. The uncertainty on the predicted background due to the energy correction is therefore estimated by repeating the analysis while varying the energy correction by ±50%.

Processes that produce either same-sign or opposite-sign di-lepton events, mainly $W^{\pm}Z$ events where one of the leptons is not reconstructed or fails identification, can also have events migrate from opposite-sign to same-sign due to charge-misID. This contribution would, of course, be included in the data-driven estimate of the charge-misID background. However, the MC used to estimate these backgrounds also contains this effect, creating a double-counting. This double-counting is removed by subtracting the MC prediction for the number of opposite-sign events from the data sample before applying the charge-misID rate. The size of the subtraction is then taken as an uncertainty to account for any mismodeling of the charge-misID rate in MC.

7.3.2 Non-prompt Background

As described in Chapter 6, the non-prompt background is estimated by applying a “fake factor” measured in a “di-jet” control region to events in the “tight+loose” (TL) control region, which is defined to have the same

	Inclusive SR $ee/e\mu/\mu\mu$	VBS SR $ee/e\mu/\mu\mu$
Total non-prompt background	0.61/1.9/0.41	0.50/1.5/0.34
2 non-prompt leptons	0.01/0.02/0.004	0.01/0.02/0.004
2 prompt leptons	0.13/0.13/0.004	0.09/0.10/0.004

Table 7.5: Contribution in weighted number of events from events where both leptons originate from hadronic activity and from events with two prompt leptons compared to the final non-prompt background prediction (including subtraction of these effects).

selections as the signal region except that one lepton is required to be non-isolated and pass only loose identification criteria. The TL control region also receives contributions from prompt processes that must be subtracted out, and the modeling of these processes when one lepton is non-isolated presents one source of uncertainty on the non-prompt background prediction. This uncertainty is conservatively taken to be 50% of the total prompt subtraction, which is shown in Table 7.5. However, due to the small size of the prompt contribution, it has a negligible effect on the total uncertainty.

It is also possible for both leptons in the event to originate from hadronic activity, an effect which is actually double-counted by the fake factor method. This double-counting is subtracted using events in a “loose+loose” (LL) region scaled the product of the fake factors for each lepton. The size of this subtraction, shown in Table 7.5, is very small and is assigned a 100% uncertainty.

The remaining uncertainties come from the calculation of the fake factor. The di-jet control region used to measure the fake factor also suffers contamination from prompt processes, mainly Z+jets and W+jets. The modeling of these processes is checked in events with $\Delta\phi(\ell, j) < 2.0$ that pass all other di-jet selections except for the transverse mass cut. The lepton is also required to pass tight selections. Table 7.6 shows the number of events observed in data as well as the MC prediction for prompt leptons. Observation and prediction agree within 4% for electrons and 12% for muons. The uncertainty from prompt subtraction is then determined by repeating the fake factor derivation while varying the prediction for prompt process up and down by the level of agreement seen for low-$\Delta\phi(\ell, j)$ events. The resulting variations in the fake factor are shown in Figure 7.4. The new fake factors are then used to determine the effect on the predicted yield. The resulting uncertainty is around 20%.

Channel	Data	MC Prediction	(Data-MC)/MC
electron	329	340.5 ± 1.4	-0.034
muon	137622	155770 ± 670	-0.117

Table 7.6: Comparison of observed event yields and the MC prediction for processes that produce prompt leptons with no m_T cut applied $\Delta\phi(\ell, j)$ required to be less than 2. The relative difference between the predicted and observed event yields is used to estimate the systematic uncertainty on the non-prompt background prediction due to the modeling of prompt contamination in the di-jet sample.

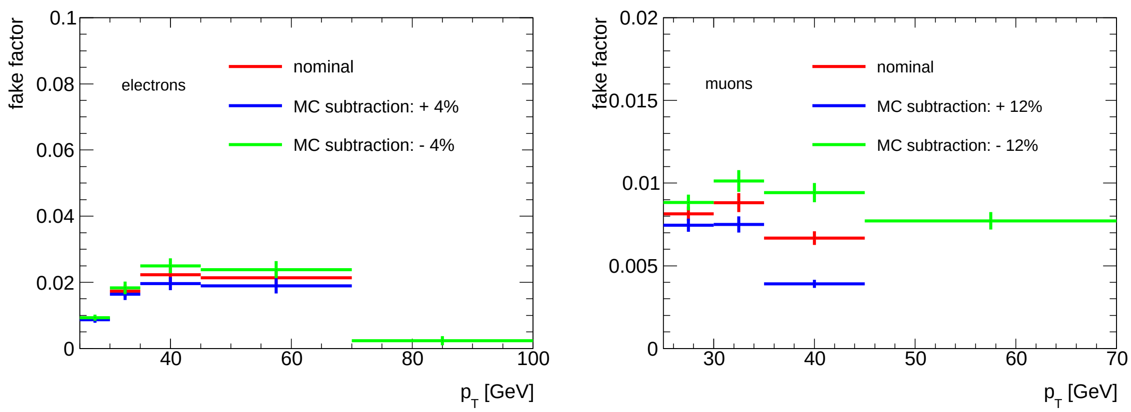

Figure 7.4: Uncertainty on the fake factor for electrons (left) and muons (right) due to the modeling of prompt contamination in the di-jet region.

Uncertainties on non-prompt background (%)			
Source	ee	$e\mu$	$\mu\mu$
di-jet statistics	10	10	5
$\Delta\phi(\ell, j)$ cut variation	10	10	5
$m_{\mathrm{T}}(\ell, E_{\mathrm{T}}^{\mathrm{miss}})$ cut variation	15	10	1
jet p_{T} cut variation	10	10	20
jet p_{T} reweighting	20	25	40
prompt subtraction	20	20	20
Total	35	40	50

Table 7.7: Summary of systematic uncertainties on the non-prompt background prediction due to uncertainties on the fake factor

The fake factor depends on event kinematics in two ways, through the selections used to define the di-jet control region and through the jet p_{T} reweighting used to extrapolate to the signal region. Each of these creates an additional source of uncertainty. The uncertainty due to event selections is evaluated by independently varying the three selections and repeating the measurement. The m_{T} and jet p_{T} selections are each varied by 5 GeV, and the $\Delta\phi(\ell, j)$ cut is varied by 0.1. Together, the variations, shown in Figure 7.5, give an uncertainty of about 20%.

The uncertainty due to the jet p_{T} reweighting is determined by varying the fitted slope of the line relating lepton $p_{\mathrm{T}} + E_{\mathrm{T}}^{\mathrm{iso}}$ to the underlying jet p_{T} up and down by 15%. The size of the variation to apply is determined using truth information in two MC samples, $t\bar{t}$ and W+jets. Events are selected by requiring one prompt lepton and one lepton from a hadron decay. Taking the nearest jet in the truth record to be the underlying jet is insufficient since muons and neutrinos are not included in the clustering, so the true underlying jet momentum is defined as the vector sum of the momenta of all jets, neutrinos, and muons within a radius of 0.3 in (η, ϕ) space around the non-prompt lepton. The p_{T} distribution for the true underlying jets is then compared to the distribution derived using the normal procedure. As shown in Figure 7.6, a 15% variation of the slope is sufficient to make the derived p_{T} distributions bracket the true distribution. The resulting variation in the fake factors is shown in Figure 7.7. After propagating the result to the signal region predictions, this uncertainty is found to be 20% for the ee and $e\mu$ channels and 40% for the $\mu\mu$ channel. Uncertainties from the fake factor measurement are summarized in Table 7.7.

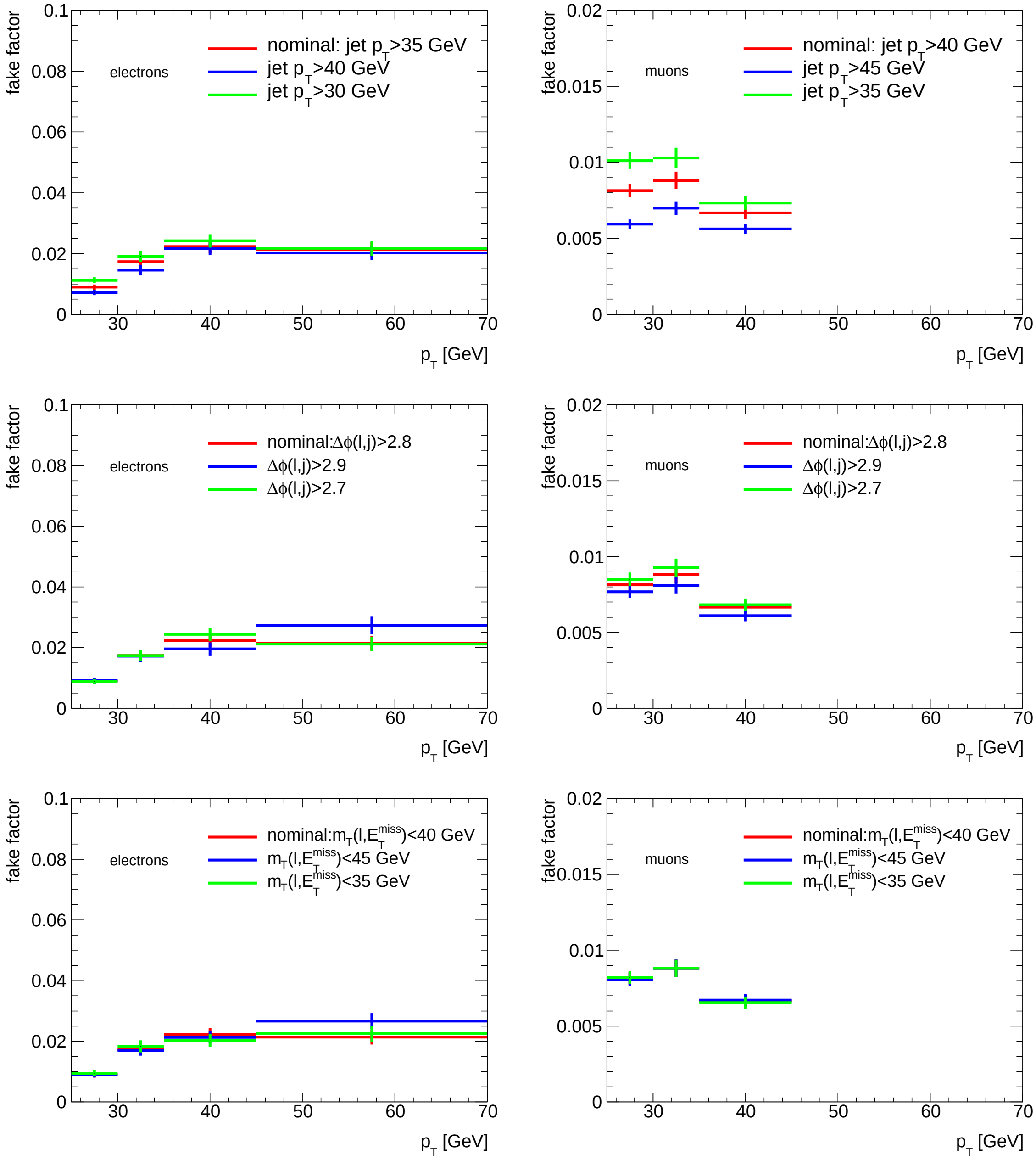

Figure 7.5: Uncertainty on the fake factor for electrons (left) and muons (right) from variations of the selections used to define the di-jet region.

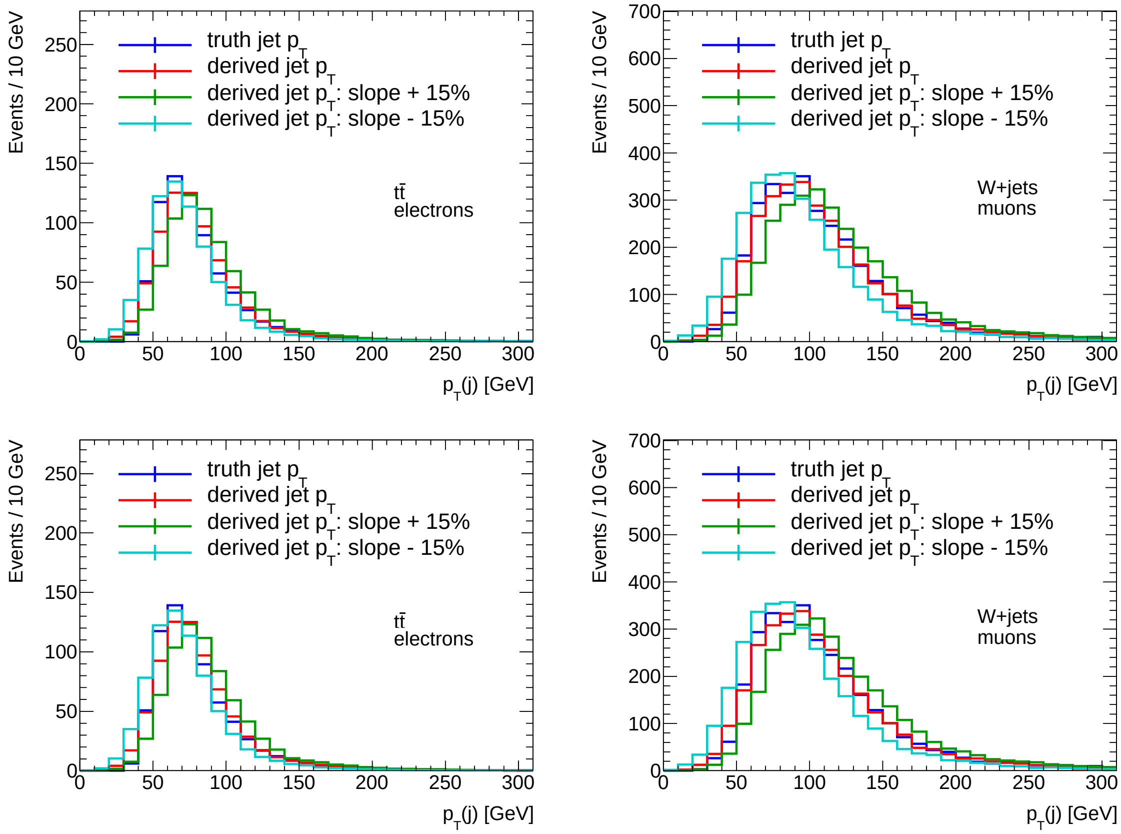

Figure 7.6: Comparison of derived underlying jet $p_{\rm T}$ distributions to the true distribution for different variations of the slope of the line relating lepton $p_{\rm T} + E_{\rm T}^{\rm iso}$ to jet $p_{\rm T}$ for electrons (left) and muons (right) in $t\bar{t}$ (top) and W+jets MC samples.

Region	Di-jet fake factor	High-d_0 fake factor
≤ 1 jet CR	8.4 ± 0.3(stat.) ± 4.5(syst.)	12.2 ± 0.4(stat.) ± 4.0(syst.)
b-tag CR	10.3 ± 0.3(stat.) ± 5.3(syst.)	16.9 ± 0.5(stat.) ± 5.5(syst.)
Low m_{jj} CR	8.1 ± 0.3(stat.) ± 4.2(syst.)	11.8 ± 0.4(stat.) ± 3.8(syst.)
Inclusive SR	0.41 ± 0.06(stat.) ± 0.21(syst.)	0.67 ± 0.10(stat.) ± 0.23(syst.)
VBS SR	0.34 ± 0.06(stat.) ± 0.18(syst.)	0.49 ± 0.09(stat.) ± 0.17(syst.)

Table 7.8: Comparison of non-prompt background predictions for the $\mu\mu$ channel using fake factors derived in the di-jet region and a "high-d_0" region in which both muons must have $d_0/\sigma(d_0) > 3$.

Additional cross-checks are performed to ensure that the estimated uncertainties are adequate. Another potential source of uncertainty on this background is the difference in flavor composition between jets in the TL region and jets in the di-jet region. This could cause the actual fake factor in the TL region to be different from the measured one, but this difference would be caused by differences in kinematic distributions between heavy-flavor jets and light-flavor jets and should be accounted for by the uncertainty on the jet p_{T} reweighting. This is checked by separating the di-jet sample into a subsample containing b-tagged jets and a subsample containing light jets and comparing the fake factors measured in each subsample. The difference between the two is found to be within the uncertainty from the jet p_{T} reweighting, so no additional uncertainty is added.

A second method of measuring the muon fake factor is also used as a cross-check. The fake factor is measured using events with two same-sign muons and two jets where both muons are required to have transverse impact parameter significance greater than 3. An extrapolation factor measured in MC is then used adjust the fake factor for the lepton selections used in the TL region ($d_0/\sigma(d_0) < 3/10$ for tight/loose muons). This method has a larger statistical uncertainty on the fake factor, with additional uncertainties coming from the extrapolation factor and the subtraction of prompt contamination. Table 7.8 compares the non-prompt background predicted using each method. The two methods agree within uncertainties, so no additional uncertainty is taken from the difference.

Systematic Uncertainties $ee/e\mu/\mu\mu$ (%) - Inclusive SR			
Background		Signal	
Jet uncertainties	11/13/13	Jet uncertainties	5.7
Theory WZ/γ^*	5.6/7.7/11	Theory $W^{\pm}W^{\pm}jj$-ewk	4.7
MC statistics	8.2/5.9/8.4	Theory $W^{\pm}W^{\pm}jj$-strong	3.1
Fake rate	3.5/7.1/7.2	Luminosity	2.8
OS lepton bkg/ Conversion rate	5.9/4.2/–	MC statistics	3.5/2.1/2.8
Theory $W+\gamma$	2.8/2.6/–	E_T^{miss} reconstruction	1.1
E_T^{miss} reconstruction	2.2/2.4/1.8	Lepton reconstruction	1.9/1.0/0.7
Luminosity	1.7/2.1/2.4	b-tagging efficiency	0.6
Lepton reconstruction	1.6/1.2/1.2	trigger efficiency	0.1/0.3/0.5
b-tagging efficiency	1.0/1.1/1.0		
Trigger efficiency	0.1/0.2/0.4		

Table 7.9: Summary of systematic uncertainties in the inclusive signal region. The left column indicates uncertainties as a percentage of the total background prediction while the right column indicates uncertainties as a percentage of the total signal prediction.

7.4 Summary

Tables 7.9 and 7.10 provide a summary of the systematic uncertainties discussed in this chapter. The first column shows the size of various groups of related uncertainties as a percentage of the total background prediction while the second column does the same for signal. The largest systematic uncertainty comes from jet uncertainties, which is dominated by the uncertainty on the jet energy scale, followed by the theoretical uncertainty on the $W^{\pm}Zjj$ cross section and MC statistics. The uncertainty on the non-prompt background also makes a significant contribution in $\mu\mu$ and $e\mu$ channels, which have better signal-to-background ratios than the ee channel.

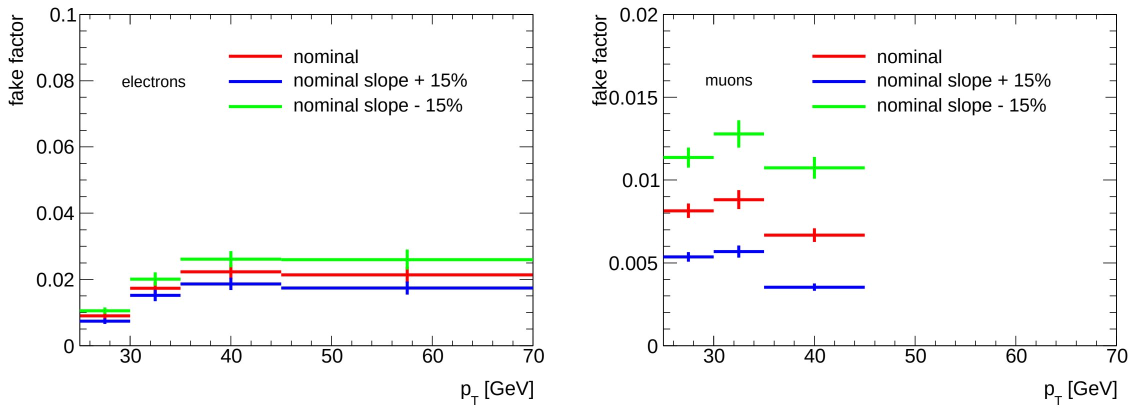

Figure 7.7: Uncertainty on the fake factor for electrons (left) and muons (right) due to the reweighting of the underlying jet p_{T} distribution.

Systematic Uncertainties $ee/e\mu/\mu\mu$ (%) - VBS SR			
Background		Signal	
Jet uncertainties	13/15/15	Theory $W^{\pm}W^{\pm}jj$-ewk	6.0
Theory WZ/γ^{*}	4.5/5.4/7.8	Jet uncertainties	5.1
MC statistics	8.9/6.4/8.4	Luminosity	2.8
Fake rate	4.0/7.2/6.8	MC statistics	4.5/2.7/3.7
OS lepton bkg/ Conversion rate	5.5/4.4/–	E_T^{miss} reconstruction	1.1
E_T^{miss} reconstruction	2.9/3.2/1.4	Lepton reconstruction	1.9/1.0/0.7
Theory $W+\gamma$	3.1/2.6/–	b-tagging efficiency	0.6
Luminosity	1.7/2.1/2.4	trigger efficiency	0.1/0.3/0.5
Theory $W^{\pm}W^{\pm}jj$-strong	0.9/1.5/2.6		
Lepton reconstruction	1.7/1.1/1.1		
b-tagging efficiency	0.8/0.9/0.7		
Trigger efficiency	0.1/0.2/0.4		

Table 7.10: Summary of systematic uncertainties in the VBS signal region. The left column indicates uncertainties as a percentage of the total background prediction while the right column indicates uncertainties as a percentage of the total signal prediction.

Chapter 8

Jet Energy Scale Performance Studies Using Z+jet Events

Since uncertainties on jet energy scale and resolution are the dominant systematic uncertainties on the $W^{\pm}W^{\pm}jj$ measurement, it is important to understand how well these uncertainties are estimated. To check the estimation of these uncertainties, a method is needed to test how well jet energy is reconstructed. One method for testing this uses Z+jet events where the Z decays to a pair of muons. The transverse momentum of the Z can be used to define a reference p_{T} ($p_{\mathrm{T}}^{\mathrm{ref}}$) to compare with the measured jet p_{T} that, since the Z is required to decay to muons, is measured using the muon spectrometer instead of the calorimeters. The ratio $p_{\mathrm{T}}^{\mathrm{jet}}/p_{\mathrm{T}}^{\mathrm{ref}}$ then provides a measure of how accurately jet energy is reconstructed. In an event consisting of only these two objects, the transverse momenta of the Z and the jet must have equal magnitude, so $p_{\mathrm{T}}^{\mathrm{ref}}$ is just the p_{T} of the Z. Real events are affected by additional soft QCD radiation such as an extra low-energy jet or pieces of the jet that emitted at a wide angle and don't get clustered with the rest of the jet, as depicted in Figure 8.1. To minimize these effects on the measurement, $p_{\mathrm{T}}^{\mathrm{ref}}$ is defined to be the projection of p_{T} of the Z onto the jet axis. Results are presented for both the EM+JES and LCW+JES calibrations, and the performance is compared between data and four $Z \to \mu\mu$ MC samples: POWHEG showered with PYTHIA8, ALPGEN showered either with HERWIG++ or PYTHIA8, and SHERPA. The EM+JES calibration has a larger effect on the $W^{\pm}W^{\pm}jj$ measurement since this is the calibration used for jets in this analysis, but the LCW+JES calibration is also used for calculating $E_{\mathrm{T}}^{\mathrm{miss}}$, so it is important to understand its performance as well.

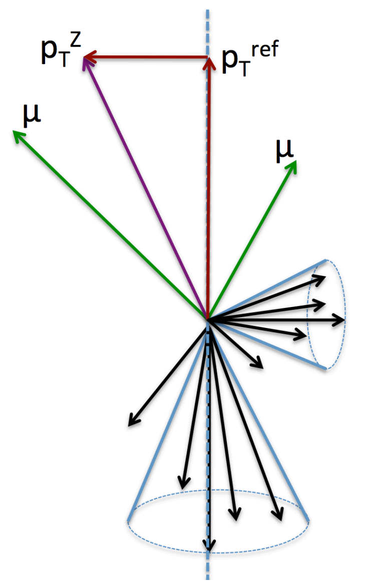

Figure 8.1: The p_{T} balance between the leading jet and the Z boson is spoiled by additional QCD radiation, so the projection of the Z p_{T} onto the jet axis is used.

8.1 Event Selection

Events are collected using the same two single muon triggers used to select $W^{\pm}W^{\pm}jj$ events, as well as a di-muon trigger that requires one muon with $p_{\mathrm{T}} > 18$ GeV and another with $p_{\mathrm{T}} > 8$ GeV. The inclusion of the di-muon trigger allows lower p_{T} thresholds to be used for muons, thereby increasing statistics for this measurement. All of the event quality criteria used in the main analysis are also applied here. Muons are required to pass the tight muon selection, except that the p_{T} threshold is lowered to 15 GeV. The minimum p_{T} for jets is also lowered to 15 GeV with jet selection otherwise identical to that used in the $W^{\pm}W^{\pm}jj$ analysis.

Events are selected to have two muons with opposite electric charge, at least one of which must have p_{T} greater than 20 GeV. The invariant mass of the muon pair is required to be between 66 GeV and 116 GeV. The separation between muons and jets, $\Delta R = \sqrt{(\eta^{\mu} - \eta^{\mathrm{jet}})^2 + (\phi^{\mu} - \phi^{\mathrm{jet}})^2}$, is required to be greater than 0.35. The leading jet in the event is required to have $p_{\mathrm{T}} > 20$ GeV, and events containing a second jet with JVF > 0.75 and p_{T} greater than 20% of the p_{T} of the Z candidate formed by the muon pair are rejected. In order to further reduce the effects of additional jet activity, the angular separation of the leading jet and the Z in the transverse plane is required to be within 0.2 radians of π. The ratio $p_{\mathrm{T}}^{\mathrm{jet}}/p_{\mathrm{T}}^{\mathrm{ref}}$ is then measured in several bins of $p_{\mathrm{T}}^{\mathrm{ref}}$ and jet $|\eta|$.

8.2 Measuring Average p_{T} Balance

Distributions of the p_{T} balance ratio in three bins of $p_{\mathrm{T}}^{\mathrm{ref}}$ for jets with $|\eta| < 1.2$ are shown in Figure 8.2. As can be seen in the left-hand plot, bins with low $p_{\mathrm{T}}^{\mathrm{ref}}$ have a steep turn-on that is caused by the minimum jet p_{T} cut. Since the lead jet must have p_{T} greater than 20 GeV, it is impossible to measure a p_{T} balance ratio less than $20/p_{\mathrm{T}}^{\mathrm{ref}}$ as those events will simply fail to be selected. This doesn't pose a problem as long as $p_{\mathrm{T}}^{\mathrm{ref}}$ is sufficiently high, but for bins with $p_{\mathrm{T}}^{\mathrm{ref}}$ below 50 GeV, it causes the average p_{T} balance to be biased above the true mean.

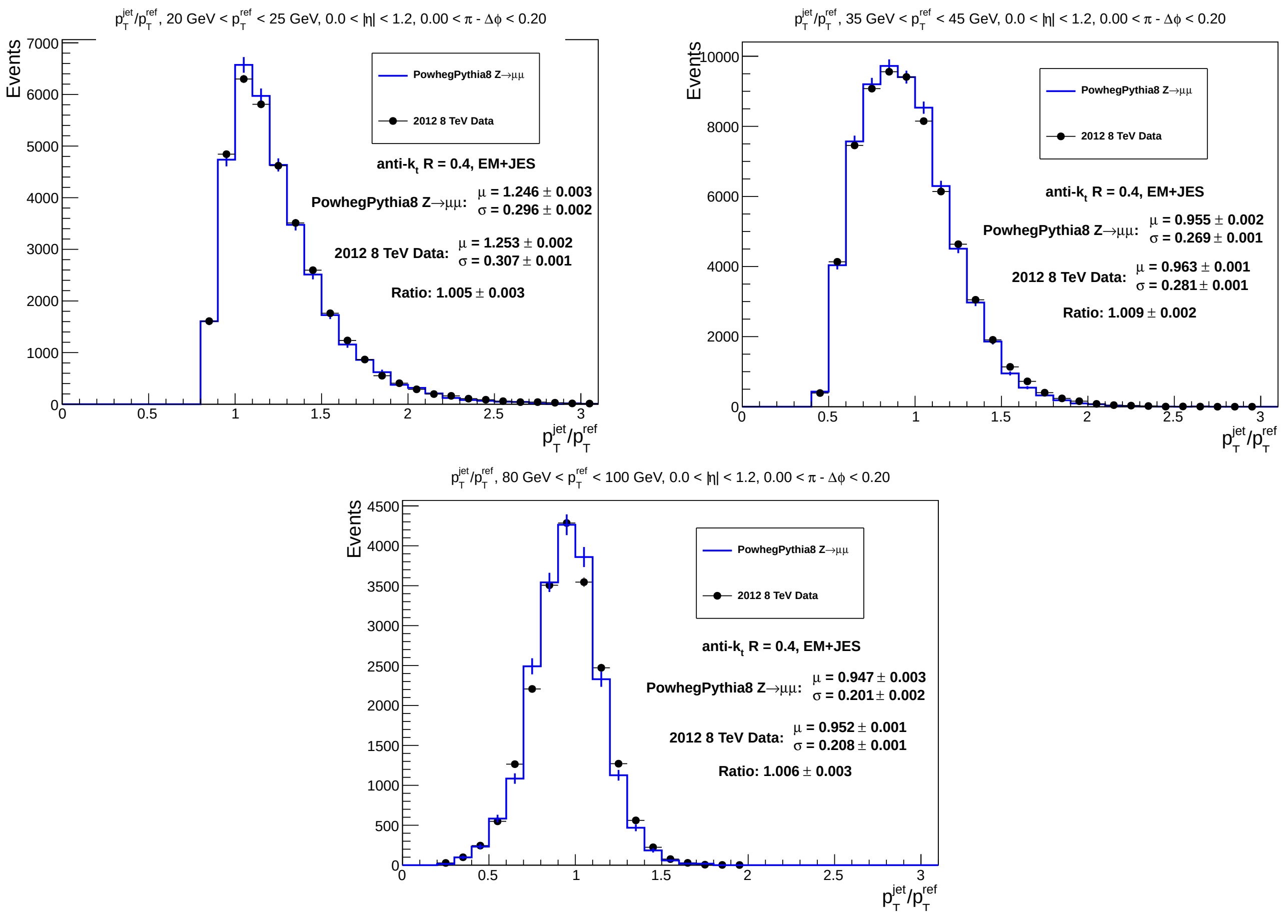

Figure 8.2: p_{T} balance distributions for jets calibrated with EM+JES with $|\eta| < 1.2$ and 20 GeV $< p_{\mathrm{T}}^{\mathrm{ref}} <$ 25 GeV (left), 35 GeV $< p_{\mathrm{T}}^{\mathrm{ref}} <$ 45 GeV (right), and 80 GeV $< p_{\mathrm{T}}^{\mathrm{ref}} <$ 100 GeV (middle). The mean (μ) and RMS (σ) of each distribution is indicated in the text labels along with the ratio of the means.

Two methods have been tried to better measure the average p_{T} balance in low-$p_{\mathrm{T}}^{\mathrm{ref}}$ bins. The first is to fit the distribution with a Poisson distribution convoluted with a linear turn-on function. The turn-on function is taken to be zero below $20/p_{\mathrm{T}}^{\mathrm{ref,max}}$ and one above $20/p_{\mathrm{T}}^{\mathrm{ref,min}}$. The mean of the Poisson is then taken as the true mean of the distribution. This method has been found to work well in a previous Z+jet p_{T} balance study using the Z decay to electrons in 7 TeV data with a leading jet p_{T} cut of 12 GeV [86]. However, the motivation for choosing this fit function was purely empirical, and it does not fit the 8 TeV data well when using the same jet p_{T} cut. This is shown in Figure 8.3. Raising the p_{T} cut to 20 GeV improves the quality of the fits but results in a loss of sensitivity to the position of the mean in lowest $p_{\mathrm{T}}^{\mathrm{ref}}$ bins, where the p_{T} balance distribution is truncated at values near 1. Fits for three $p_{\mathrm{T}}^{\mathrm{ref}}$bins are shown in Figure 8.4.

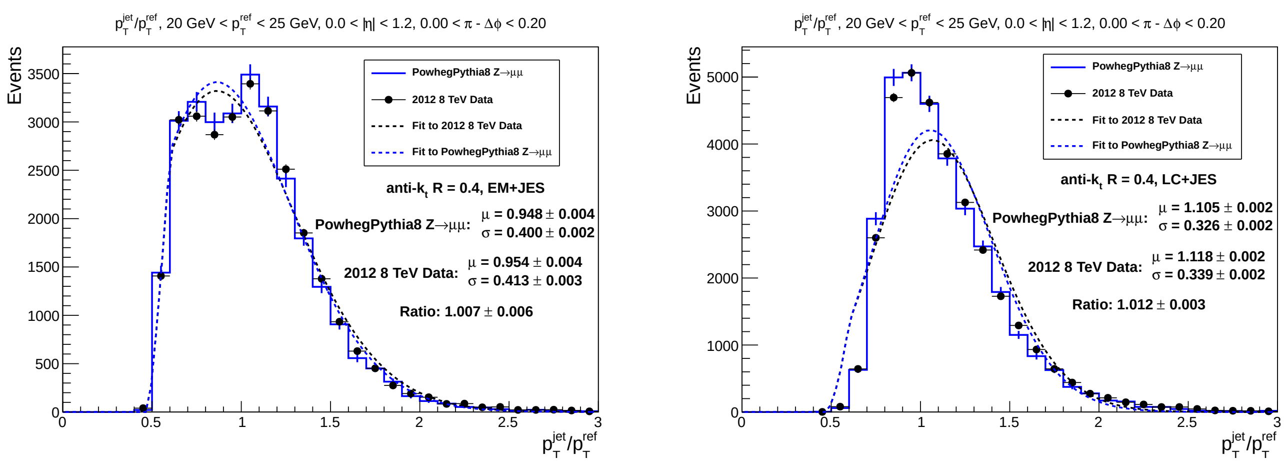

Figure 8.3: p_{T} balance distributions for $p_{\mathrm{T}}^{\mathrm{ref}}$ between 20 GeV and 25 GeV and $|\eta| < 1.2$ for jets calibrated with EM+JES (left) and LCW+JES (right) when requiring the leading jet to have $p_{\mathrm{T}} > 12$ GeV. Neither shape fits a Poisson with a linear turn-on between $12/p_{\mathrm{T}}^{\mathrm{ref,max}} = 0.48$ and $12/p_{\mathrm{T}}^{\mathrm{ref,min}} = 0.6$. The mean ($\mu$) and width ($\sigma$) of Poisson fitted to each distribution is indicated in the text labels along with the ratio of the means.

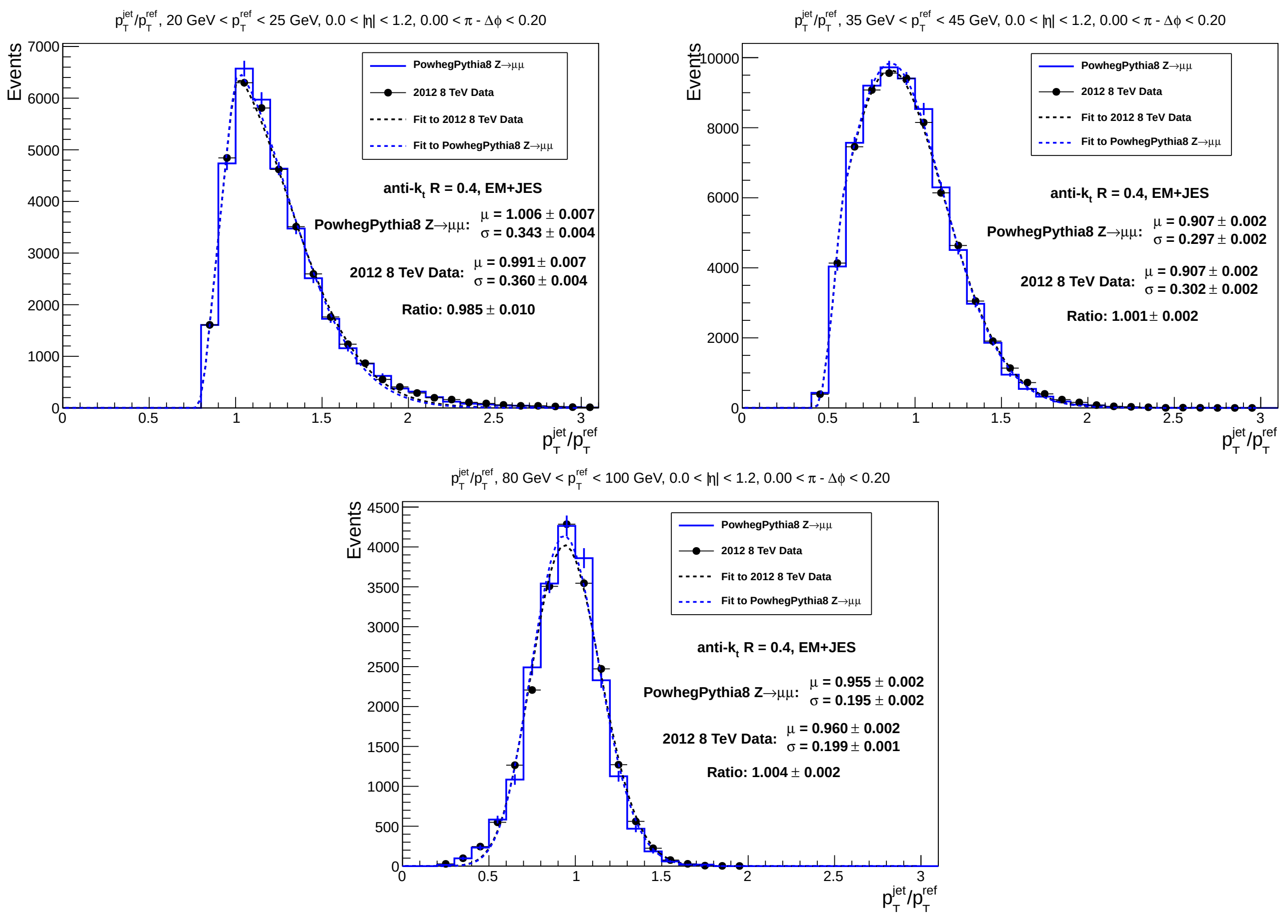

Figure 8.4: p_{T} balance distributions for jets calibrated with EM+JES with $|\eta| < 1.2$ and 20 GeV $< p_{\mathrm{T}}^{\mathrm{ref}} <$ 25 GeV (left), 35 GeV $< p_{\mathrm{T}}^{\mathrm{ref}} <$ 45 GeV (right), and 80 GeV $< p_{\mathrm{T}}^{\mathrm{ref}} <$ 100 GeV (middle). Each distribution is fit with a Poisson function convoluted with a linear turn-on. The mean (μ) and width (σ) of Poisson fitted to each distribution is indicated in the text labels along with the ratio of the means.

Good agreement is seen in the shape of the p_{T} balance distribution between data and MC, and this suggests a more reliable way to fit the data. Instead of choosing an arbitrary function, the data is fit using a template made from the MC. In the fit the template is allowed to shift, and its width is allowed to change. The fitted shift measures the difference in the average p_{T} balance between data and MC. To mitigate the effects of bin-to-bin fluctuations, the template is smoothed by taking a weighted average of adjacent bins. As shown in Figure 8.5, this method can produce better fits in bins where the Poisson fit struggles, but the value that is obtained in the fit is only the difference between the means. The individual means for data and MC are still biased using this method. This bias is reduced by taking the mean using only the neighborhood where the function is above half its maximum value. Figure 8.6 shows template fits for three $p_{\mathrm{T}}^{\mathrm{ref}}$ bins. The template fit shows a bias between those of the Poisson fit and arithmetic mean for the lowest $p_{\mathrm{T}}^{\mathrm{ref}}$ bin, and results are otherwise similar to those obtained using the Poisson fit.

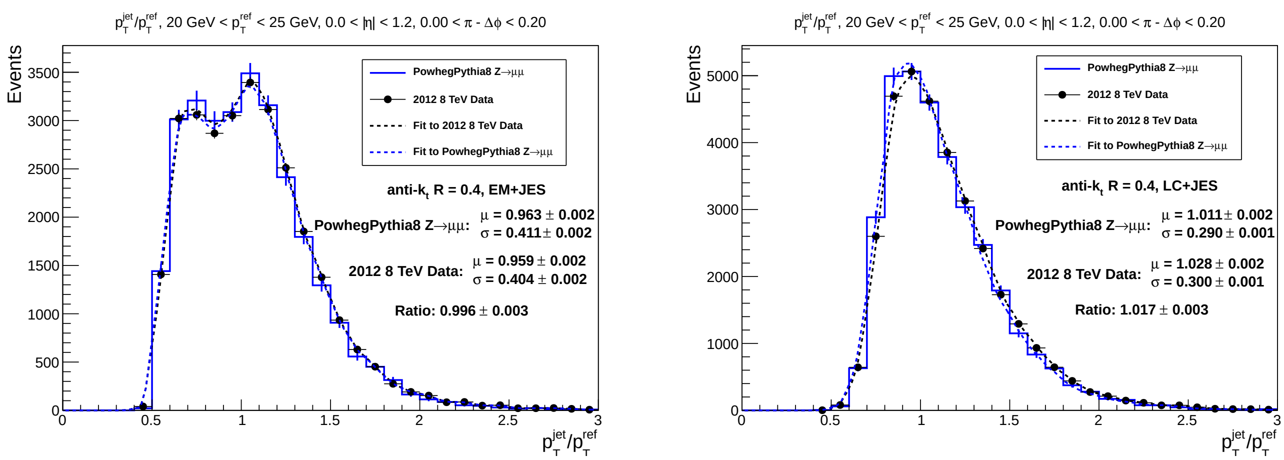

Figure 8.5: p_{T} balance distributions for $p_{\mathrm{T}}^{\mathrm{ref}}$ between 20 GeV and 25 GeV and $|\eta| < 1.2$ for jets calibrated with EM+JES (left) and LCW+JES (right) when requiring the leading jet to have $p_{\mathrm{T}} > 12$ GeV. The template fit used shows good agreement with the distributions but doesn't fix the bias. The half-width at half of the maximum (σ) and mean of the template between the half-maxima (μ) are indicated in the text labels for the fit to each distribution along with the ratio of the means.

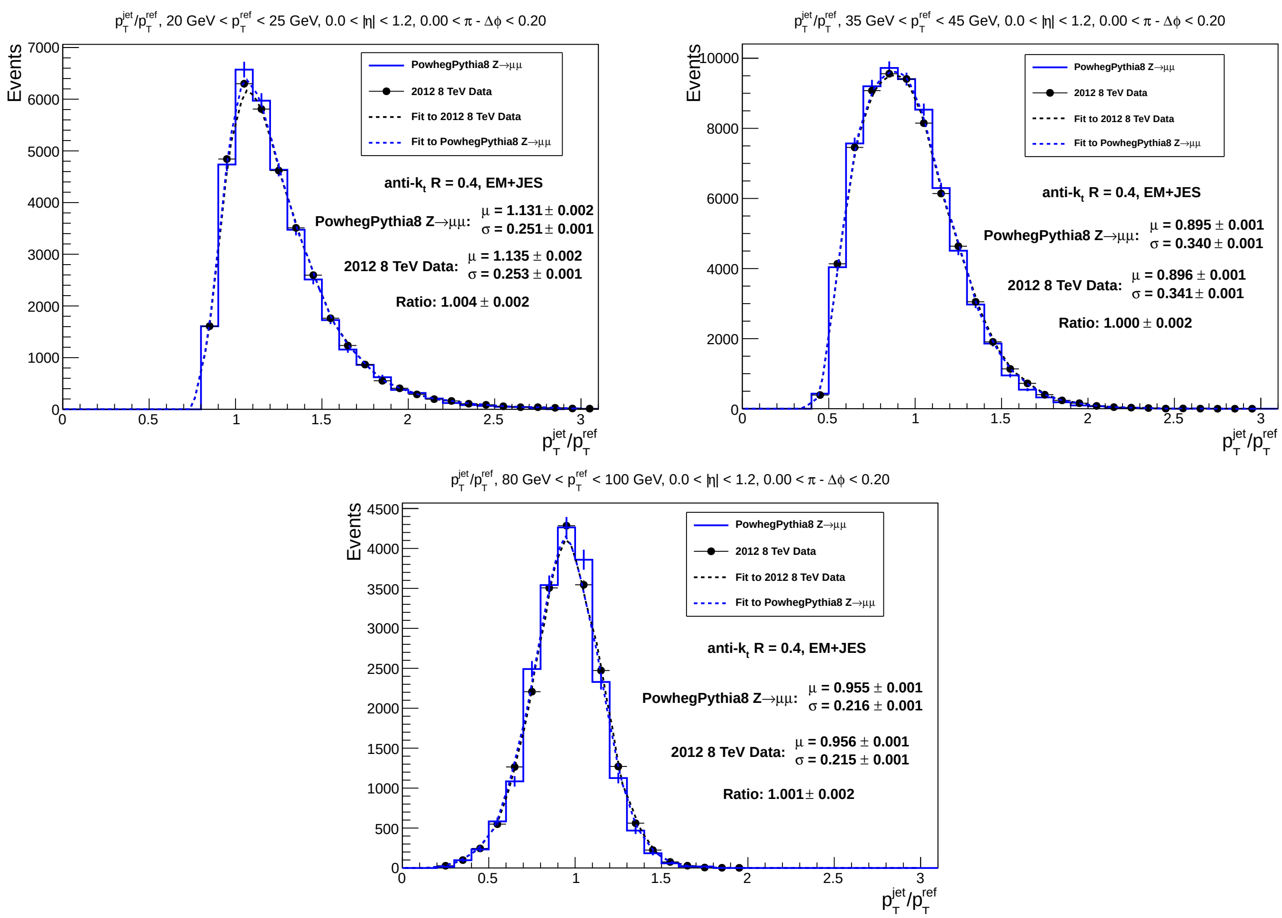

Figure 8.6: p_{T} balance distributions for jets calibrated with EM+JES with $|\eta| < 1.2$ and 20 GeV $< p_{\mathrm{T}}^{\mathrm{ref}} <$ 25 GeV (left), 35 GeV $< p_{\mathrm{T}}^{\mathrm{ref}} <$ 45 GeV (right), and 80 GeV $< p_{\mathrm{T}}^{\mathrm{ref}} <$ 100 GeV (middle). Each distribution is fit with a template constructed from the MC. The half-width at half of the maximum (σ) and mean of the template between the half-maxima (μ) are indicated in the text labels for the fit to each distribution along with the ratio of the means.

8.3 FCAL High Voltage Problem

One interesting application of this Z+jet p_{T} balance study was to quantify the effect of a problem with the high voltage (HV) supplies of the forward calorimeters that affected a portion of the 2012 run. In June, 2012 new HV supply units were installed in two quadrants of the first FCAL layer, covering $1.6 < \phi < 3.1$ on either side of the detector ($|\eta| > 3.2$). Unfortunately, the new units supplied 30% less voltage than they were supposed to, and since events were reconstructed assuming the correct voltage, jets in the affected areas were reconstructed with lower energies. The problem was eventually discovered and the old HV modules put back in, but 1.2 fb^{-1} of data were affected.

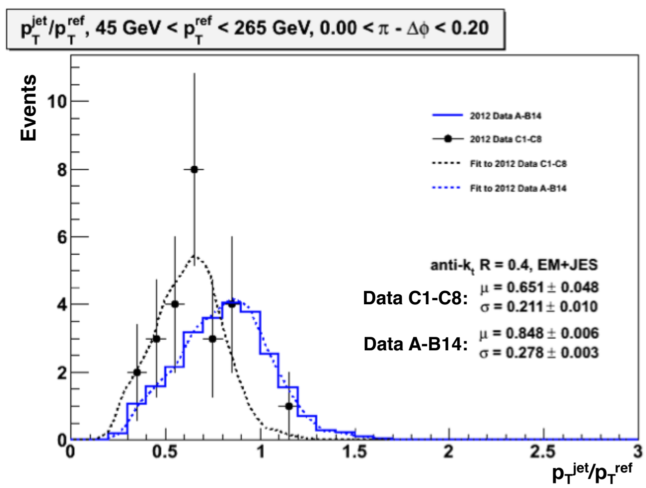

Figure 8.7: p_{T} balance distributions for data taken before the installation of faulty HV modules (solid line) and data taken while the faulty units were in place (points). Average p_{T} balance is measured using the template fit method, with the distribution for the data taken with good HV units used for the template. The half-width at half of the maximum (σ) and mean of the template between the half-maxima (μ) are indicated in the text labels for the fit to each distribution along with the ratio of the means.

Figure 8.7 shows the p_{T} balance distribution for events with jets in the affected area for data taken before the new units were installed and data taken while they were in place. The dashed lines show fits using the unaffected data as a template. The mean p_{T} balance for the data with the faulty HV units is observed to be about 20% lower than for the data with good HV units. The data were eventually reprocessed using the actual HV supplied before being used for the $W^{\pm}W^{\pm}jj$ measurement, eliminating the need to apply a correction, but the ability to see this effect demonstrates the sensitivity of the Z+jet p_{T} balance method to differences between the calibrated jet p_{T} and the true jet p_{T} .

8.4 Results

Figure 8.8 shows the average p_{T} balance for the EM+JES calibration as a function of $p_{\mathrm{T}}^{\mathrm{ref}}$ in four $|\eta|$ bins using just the mean of the distribution. Corresponding plots for the LCW+JES calibration are shown in Figure 8.9. The data/MC ratio is shown in the bottom panel of each plot along with the fractional uncertainty due to the jet energy scale and resolution. Good agreement is seen between data and MC within the systematic uncertainty.

As previously discussed, the average p_{T} balance is biased towards large values for low $p_{\mathrm{T}}^{\mathrm{ref}}$. Since this is true for both data and MC, the data/MC ratio is biased towards one. While an unbiased measurement of the average p_{T} balance is desirable, it is not necessary in order to evaluate whether the systematic uncertainty is sufficient to cover the observed data/MC differences. The JES/JER systematic is propagated to this measurement by repeating the analysis with the energy of each jet varied up and down by the JES uncertainty or with the jet energy smeared by a Gaussian distribution with a width given by the JER uncertainty. The measurements with the JES variations will also be biased towards large average p_{T} balance, which means the ratio MC$\pm1\sigma^{\mathrm{JES}}$/MC will also be biased towards one. This effect is what causes the fractional uncertainty shown in Figure 8.8 to decrease below $p_{\mathrm{T}}^{\mathrm{ref}}= 50$ GeV even though calorimeter resolution is worse at low energy.

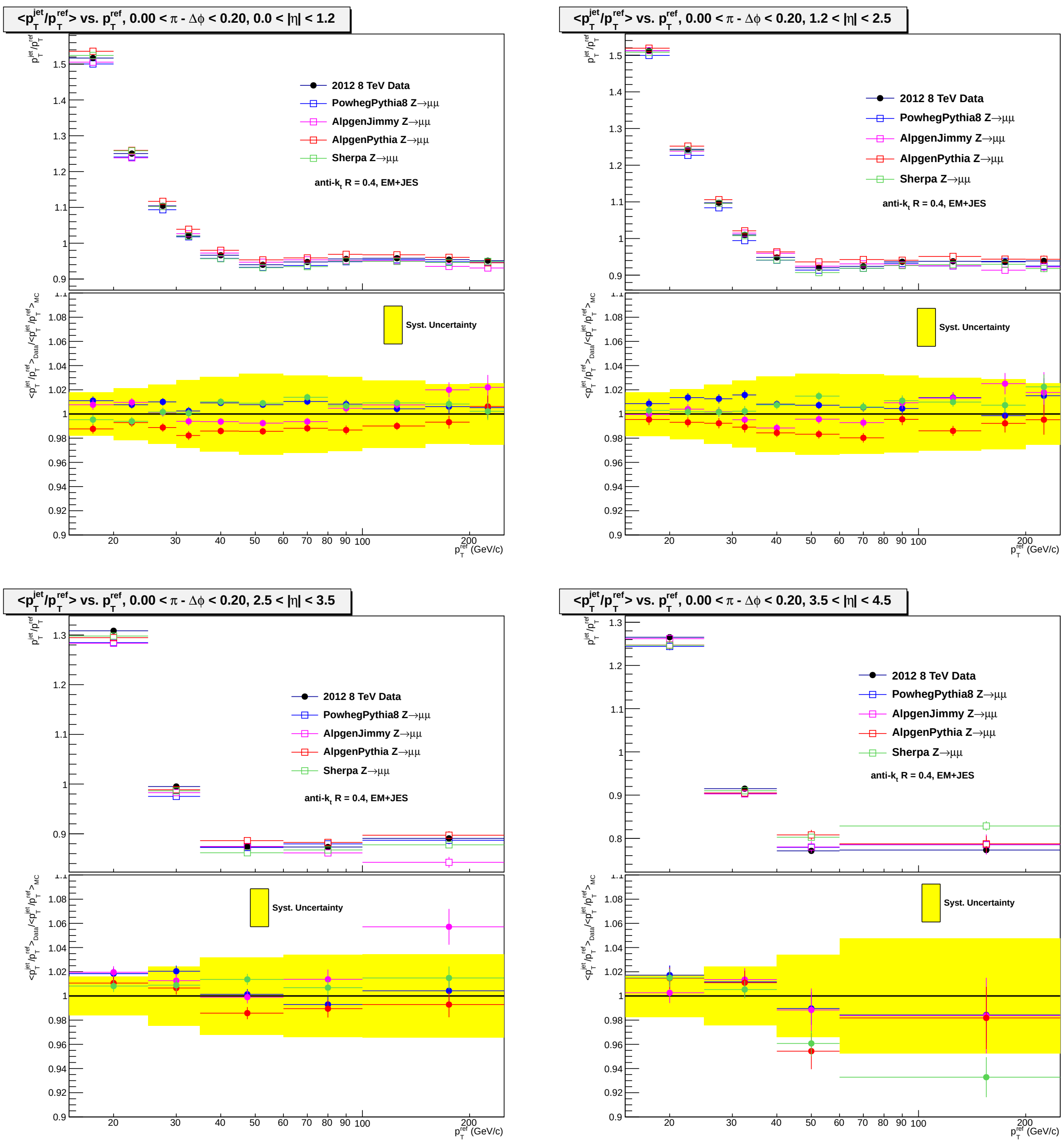

Figure 8.8: Average value of $\frac{p_T^{jet}}{p_T^{ref}}$ for EM+JES-calibrated jets as a function of p_T^{ref} for four bins in jet η with the data/MC double-ratio shown at the bottom. The yellow band on the double-ratio plot shows the systematic uncertainty from the jet energy scale.

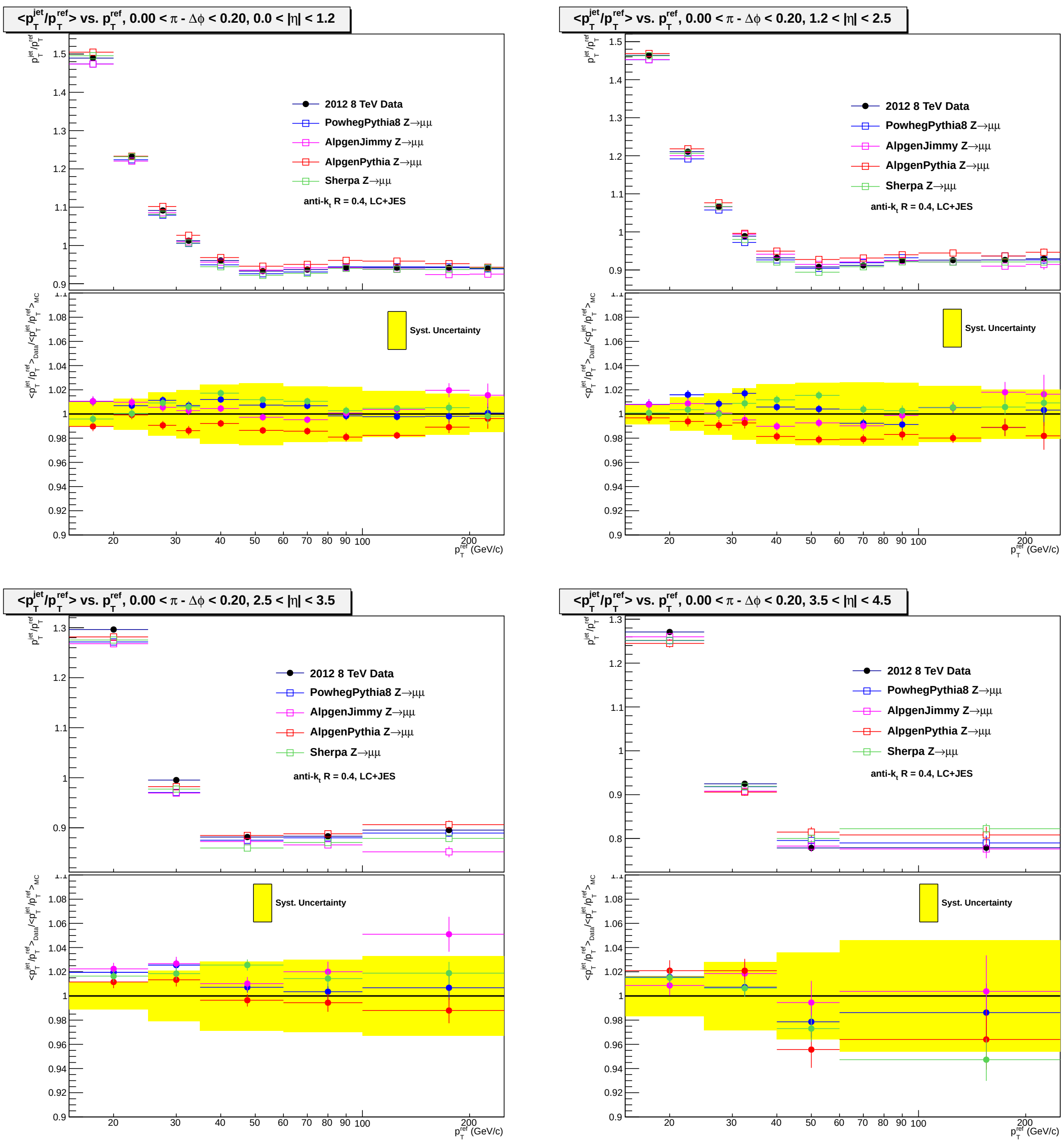

Figure 8.9: Average value of $\frac{p_T^{jet}}{p_T^{ref}}$ for LCW+JES-calibrated jets as a function of p_T^{ref} for four bins in jet η with the data/MC double-ratio shown at the bottom. The yellow band on the double-ratio plot shows the systematic uncertainty from the jet energy scale.

Chapter 9

Results

9.1 Summary of Control Region Observations

In addition to the regions previously described, a low m_{jj} control region is defined by inverting the m_{jj} selection and dropping the $|\Delta y_{jj}|$ selection. The background composition in this region is very similar to the signal regions, but the signal contribution is greatly reduced. This provides a final check of the combined background model in a region very close to the signal regions. The $|\Delta y_{jj}|$ distribution in the low m_{jj} control region is shown in Figure 9.1, and event counts are given in Table 9.1.

The results for all control regions are summarized in Table 9.2. They show good agreement between data and prediction. Nine of the twelve statistically independent control regions have agreement within the estimated uncertainty while the remaining three all agree within twice the uncertainty. Assuming the measurements follow a Gaussian distribution, the expected numbers of 1σ and 2σ deviations are roughly 4 and 0.5, respectively. These results give confidence that the background and its systematic uncertainties are properly estimated.

9.2 Signal Region Observations

Table 9.3 shows the predicted and observed number of events in the two signal regions. A total of 20.1 background events and 21.7 signal events (both electroweak and strong $W^{\pm}W^{\pm}jj$ production) are predicted in the inclusive SR while 15.9 background events and 13.9 signal events (electroweak $W^{\pm}W^{\pm}jj$ only) are predicted in the VBS SR. The observed yields are 50 events and 34 events, respectively, a slight excess over the total prediction.

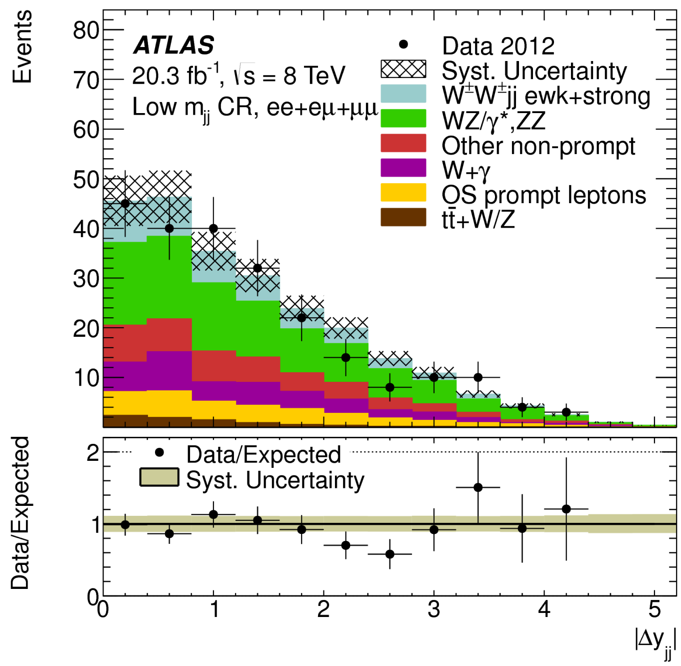

Figure 9.1: $|\Delta y_{jj}|$ distribution for events in the low m_{jj} control region. The top panel shows the number of events for the data (points) and the Standard Model prediction (histogram) while the points in the bottom panel show the ratio of data/prediction. The systematic uncertainty on the prediction is indicated by the hatched band in the top panel and solid band in the bottom panel.

Low m_{jj} Control Region				
	ee	$e\mu$	$\mu\mu$	Total
$W^{\pm}W^{\pm}$jj ewk+strong	6.5 ± 0.7	18.8 ± 1.9	11.4 ± 1.2	37 ± 4
$WZ/\gamma^*,ZZ$	25 ± 4	54 ± 9	18.4 ± 3.1	98 ± 16
$W+\gamma$	14 ± 4	20 ± 6	0.00 ± 0.00	34 ± 10
OS prompt leptons	19.4 ± 2.3	8.4 ± 1.4	–	27.8 ± 3.4
$t\bar{t}+W/Z$	1.7 ± 0.7	3.8 ± 1.6	2.4 ± 1.0	7.9 ± 3.4
Other non-prompt	9 ± 4	21 ± 8	8 ± 4	39 ± 10
Total Predicted	76 ± 9	127 ± 16	40 ± 6	243 ± 27
Data	78	120	30	228

Table 9.1: Event counts in the low m_{jj} control region. Observed event yields agree well with the Standard Model prediction.

Control Region		Trilepton	≤ 1 jet	b-tagged	Low m_{jj}
ee	pred.	36 ± 6	278 ± 28	40 ± 6	76 ± 9
	data	40	288	46	78
$e\mu$	pred.	110 ± 18	288 ± 42	75 ± 13	127 ± 16
	data	104	328	82	120
$\mu\mu$	pred.	60 ± 10	88 ± 14	25 ± 7	40 ± 6
	data	48	101	36	30

Table 9.2: Comparison of predicted ("pred.") and observed ("data") event counts for all control regions.

	Inclusive Region			VBS Region		
	ee	$e\mu$	$\mu\mu$	ee	$e\mu$	$\mu\mu$
Prompt	3.0 ± 0.7	6.1 ± 1.3	2.6 ± 0.6	2.2 ± 0.5	4.2 ± 1.0	1.9 ± 0.5
Conversions	3.2 ± 0.7	2.4 ± 0.8	–	2.1 ± 0.5	1.9 ± 0.7	–
Other non-prompt	0.61 ± 0.30	1.9 ± 0.8	0.41 ± 0.22	0.50 ± 0.26	1.5 ± 0.6	0.34 ± 0.19
$W^{\pm}W^{\pm}jj$ Strong	0.89 ± 0.15	2.5 ± 0.4	1.42 ± 0.23	0.25 ± 0.06	0.71 ± 0.14	0.38 ± 0.08
$W^{\pm}W^{\pm}jj$ Electroweak	3.07 ± 0.30	9.0 ± 0.8	4.9 ± 0.5	2.55 ± 0.25	7.3 ± 0.6	4.0 ± 0.4
Total background	6.8 ± 1.2	10.3 ± 2.0	3.0 ± 0.6	5.0 ± 0.9	8.3 ± 1.6	2.6 ± 0.5
Total predicted	10.7 ± 1.4	21.7 ± 2.6	9.3 ± 1.0	7.6 ± 1.0	15.6 ± 2.0	6.6 ± 0.8
Data	12	26	12	6	18	10

Table 9.3: Predicted and observed event counts in the signal regions. The "Total background" includes strong $W^{\pm}W^{\pm}jj$ production in the VBS region but not in the inclusive region, where both strong and electroweak production are treated as signal.

Figure 9.2 shows the di-jet invariant mass distribution just prior to applying the m_{jj} cut and the Δy_{jj} distribution after requiring $m_{jj} > 500$ GeV. Vector boson scattering processes are characterized by two jets that form a large invariant mass and have a large separation in rapidity. Accordingly, the distribution show an increase in the fraction of predicted events coming from the electroweak production of $W^{\pm}W^{\pm}jj$ at large values of these observables. The data agrees well with the total distribution and disfavors the background-only prediction.

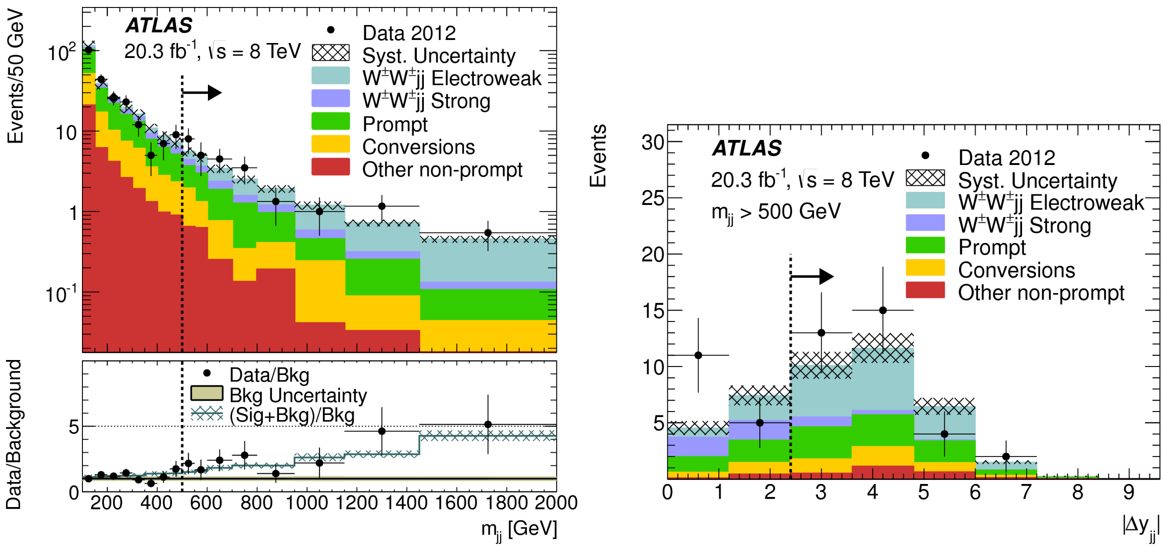

(a) (b)

Figure 9.2: (a) The di-jet invariant mass distribution for events passing all signal selections before the m_{jj} requirement is applied (b) the Δy_{jj} distribution of events in the inclusive SR. In the bottom panel of the m_{jj} plot, the points show the ratio of data to the predicted background while the line and hatched band give the ratio of the total prediction (signal + background) to the background prediction and the systematic uncertainty on this ratio.

Distributions related to the WW system are shown in Figure 9.3 for the VBS SR. Figure 9.3a shows the transverse mass formed using the two leptons and missing transverse energy. Neglecting the lepton masses, it is defined as $m_{\mathrm{T}} = \sqrt{(p_{\mathrm{T}}^{\ell_1} + p_{\mathrm{T}}^{\ell_2} + E_{\mathrm{T}}^{\mathrm{miss}})^2 - (\vec{p}_{\mathrm{T}}^{\ell_1} + \vec{p}_{\mathrm{T}}^{\ell_2} + \vec{E}_{\mathrm{T}}^{\mathrm{miss}})^2}$. The background prediction peaks at low values of m_{T} while the $W^{\pm}W^{\pm}jj$ contribution peaks near $m_{\mathrm{T}} = 2m_W$. The combined distribution agrees well with observation. Figure 9.3b shows the scalar sum of the lepton transverse momenta, which is sensitive to aQGCs. The anomalous couplings operators discussed in Chapter 2 contain derivatives of the gauge fields and will be enhanced when the momenta of the gauge bosons are large. The presence of aQGCs would therefore be expected to appear as an excess at large $\Sigma|p_{\mathrm{T}}^{\ell}|$, as shown in Figure 9.4. The observed data exhibit agreement with uncertainties over the full range of the distribution.

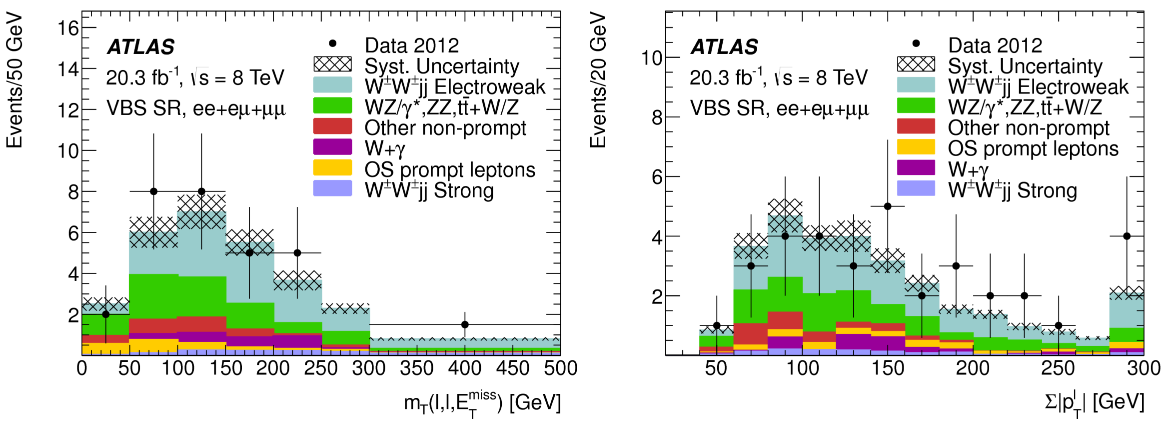

(a) (b)

Figure 9.3: VBS SR distributions for (a) the transverse mass formed using both leptons and missing transverse energy and (b) the scalar sum of the lepton momenta.

Figure 9.5 shows two more distributions that give good separation between the strong and electroweak production mechanism. Lepton centrality (Figure 9.5a) is defined as:

$$\zeta = \min[\min(\eta^{\ell_1}, \eta^{\ell_2}) - \min(\eta^{j_1}, \eta^{j_2}), \max(\eta^{j_1}, \eta^{j_2}) - \max(\eta^{\ell_1}, \eta^{\ell_2})] \quad (9.1)$$

where ℓ_1 and ℓ_2 are the two leptons and j_1 and j_2 are the two highest-p_{T} jets in the event. Positive values indicate events in which the pseudorapidities of the leptons are situated in between the pseudorapidities of the jets, while negative values correspond to events where at least one lepton is not bracketed by the jets. Since the jets in electroweak $W^{\pm}W^{\pm}jj$ production scatter at smaller angles with respect to the beam direction than the jets in strong production, positive values of lepton centrality are expected to be dominated by electroweak production. The jet multiplicity (Figure 9.5b) for electroweak production is also more sharply peaked at two jets than

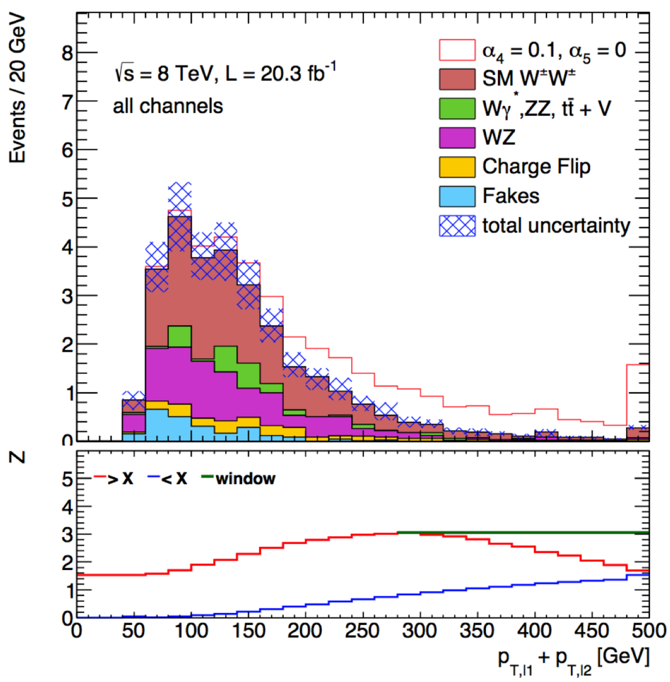

Figure 9.4: Scalar sum of the lepton momenta in the VBS signal region. The Standard Model prediction ($\alpha_4 = \alpha_5 = 0$) is given by the solid histogram, and the red line shows how the prediction would change for $\alpha_4 = 0.1$.

for strong production. In both cases, the data agrees well with the total prediction.

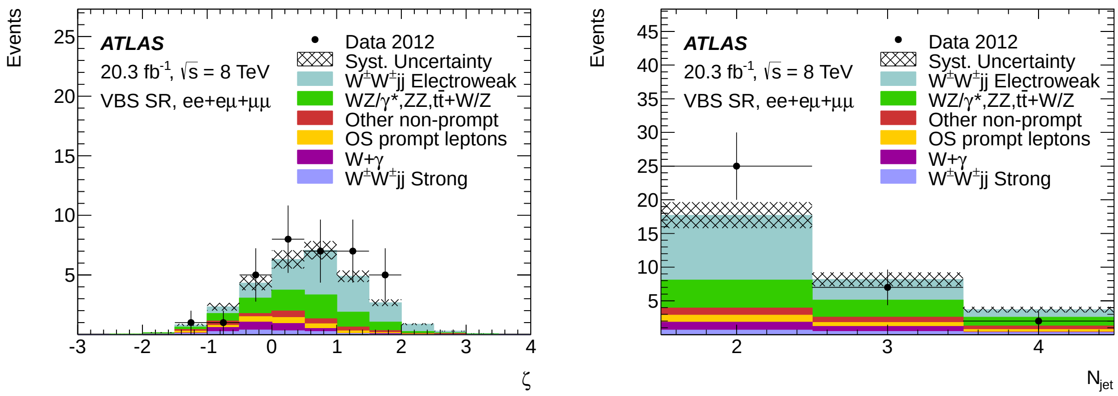

(a) (b)

Figure 9.5: VBS SR distributions for (a) the lepton centrality and (b) the jet multiplicity, which include the requirement $|\Delta y_{jj}| > 2.4$. The points show the observed data while the stacked histogram gives the SM prediction.

As discussed in Chapter 2, the predicted ratio between events with positively charged leptons and events with negatively charged leptons is about 3.3 for $W^{\pm}W^{\pm}jj$ production. This is much greater than for other process with prompt same-sign leptons (expected ratio less than 2) or non-prompt leptons (expect equal numbers of positive and negative charges). Figure 9.6 shows the sum of the lepton charges for events in the VBS region. The data agrees well with the prediction from MC.

9.3 Testing the Standard Model Hypothesis

The event yields and distributions in the signal regions show a clear preference for the Standard Model hypothesis, which includes $W^{\pm}W^{\pm}jj$, over the background-hypothesis. The statistical significance of this statement is evaluated using a profile likelihood test [87]. Before considering systematic uncertainties, the likelihood of observing N_i^{obs} events in a channel where N_i^{exp} are expected follows a Poisson distribution. The total likelihood is then a product across the three channels with one unknown parameter, the $W^{\pm}W^{\pm}jj$ cross section, that changes N_i^{exp}.

$$L(\sigma_{WW}) = \prod_i \mathrm{Poisson}(\mathrm{N_i^{obs}} | \mathrm{N_i^{exp}}(\sigma_{\mathrm{WW}})) \tag{9.2}$$

Systematic uncertainties are taken into account by adding nuisance parameters to Equation 9.2. Uncertainties are assumed to follow a Gaussian distribution, with a shift of 1 standard deviation in the nuisance parameter causing a shift in the expected number of events by the measured value of the associated uncertainty. The leads to the following likelihood function:

$$L(\sigma_{WW}, \vec{\alpha}) = \prod_{\mathrm{chan}} \mathrm{Poisson}(\mathrm{N^{obs}} | \mathrm{N^{exp}}(\sigma_{\mathrm{WW}}, \tilde{\alpha})) \prod_{\mathrm{syst}} \mathrm{Gaus}(\alpha | \mu = 0, \sigma = 1) \tag{9.3}$$

Maximizing the likelihood with respect to all free parameters gives the $W^{\pm}W^{\pm}jj$ cross section that is most consistent with the data. The consistency of a given hypothesis with the data is then determined by comparing the maximum likelihood for that hypothesis (that is, with a given value of σ_{WW}) to the unconditional maximum likelihood using a test statistic. The test statistic used is:

$$\lambda(\sigma_{WW}) = -2 \ln \frac{L(\sigma_{WW}, \hat{\hat{\vec{\alpha}}})}{L(\sigma_{\hat{W}W}, \hat{\vec{\alpha}})} \tag{9.4}$$

Where $\{\hat{x}\}$ denote the set of parameters that give the overall maximum likelihood, and $\hat{\hat{\vec{\alpha}}}$ denotes the set of nuisance parameters that maximize the likelihood for a given σ_{WW}. In the large-statistics limit, this quantity follows a χ^2 distribution, with values near zero corresponding to measurements that agree well with the hypothesis and large values indicating a measurement that is inconsistent with the hypothesis. The significance with which a hypothesis is rejected using this test is $Z = \sqrt{\lambda}$, where Z indicates the likelihood of obtaining a value of the test statistic at least as large as the observed one, translated into units of standard deviations from the mean of a Gaussian distribution. The corresponding probabilities for significances up to 6 standard deviations is shown in Table 9.4.

Using this method, the measured fiducial cross sections are 2.1 ± 0.5(stat.) $\pm$ 0.3(syst.) fb for the sum of electroweak and strong $W^{\pm}W^{\pm}jj$ production in the inclusive SR and 1.3 ± 0.4(stat.) $\pm$ 0.2(syst.) fb for electroweak production plus interference in the VBS region. These values are in agreement with the Standard Model predictions of 1.52 ± 0.11 fb and 0.95 ± 0.06

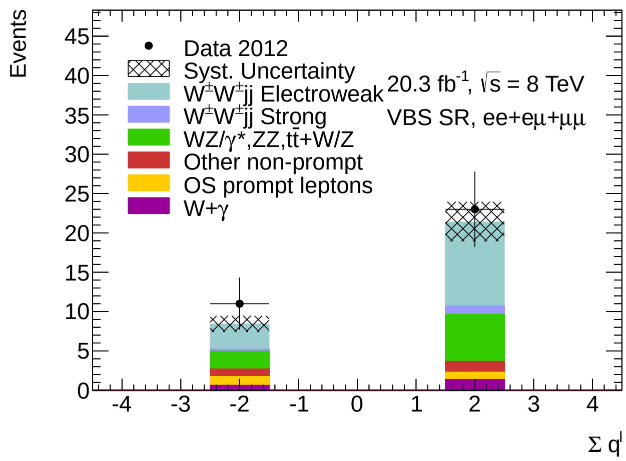

Figure 9.6: Sum of the lepton charges for events in the VBS signal region, which includes the requirement $|\Delta y_{jj}| > 2.4$. The points show the observed data while the stacked histogram gives the SM prediction.

α	Z
0.3173	1σ
4.55×10^{-2}	2σ
2.7×10^{-3}	3σ
6.3×10^{-5}	4σ
5.7×10^{-7}	5σ
2.0×10^{-9}	6σ

Table 9.4: Probability (α) corresponding to a given significance (Z) [8].

fb. The cross sections measured for individual channels are shown in Figure 9.7. The significance with which the background-only hypothesis (which includes strong $W^{\pm}W^{\pm}jj$ production in the VBS region) is rejected is 4.5σ in the inclusive region and 3.6σ in the VBS region. This constitutes the first evidence for $W^{\pm}W^{\pm}jj$ production as a whole and for the electroweak process.

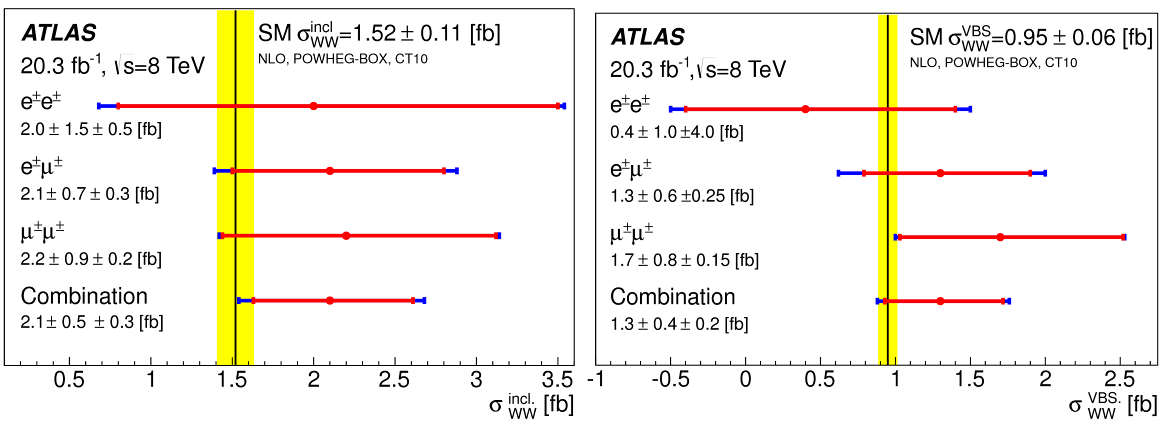

Figure 9.7: Measured fiducial cross sections for electroweak+strong production in the inclusive SR(left) and electroweak+interference in the VBS SR(right). The inner red bands indicate the uncertainties on the measured cross sections due only to statistics while the outer blue bands give the total uncertainty.

9.4 Testing aQGC Hypotheses

The VBS SR is used to test aQGC hypotheses. Using the test statistic defined in Equation 9.4, an aQGC hypothesis, defined by the choice of the parameters (α_4, α_5), is rejected at 95% confidence level (CL) if $\lambda \geq 3.84$. The WHIZARD [88] event generator interfaced to PYTHIA8 for parton showering is used to derive the fiducial cross section for electroweak $W^{\pm}W^{\pm}jj$ production for a given choice of α_4 and α_5. A fine grid of points is used to map out the cross sections in the (α_4, α_5) plane as shown in Figure 9.8. WHIZARD generates events at leading order in in the strong coupling constant. The NLO cross section for the Standard Model point ($\alpha_4 = \alpha_5 = 0$), calculated using POWHEG-BOX as described in Chapter 6, is found to be 1.3 times higher than the WHIZARD cross section. This scale factor is applied to all aQGC points to obtain approximate NLO cross sections. The contribution from interference is also included and is calculated using:

$$\sigma_{VBS}^{INT} = k_{INT}\sqrt{\sigma_{VBS}^{ewk}\sigma_{VBS}^{strong}} \tag{9.5}$$

where σ_{VBS}^{ewk} and σ_{VBS}^{strong} are the cross sections for electroweak and strong production in the VBS signal region, and k_{INT} is a proportionality factor determined from the Standard Model cross sections to be 0.231.

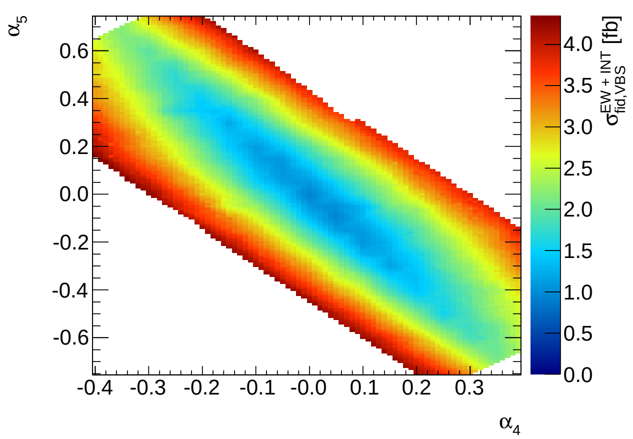

Figure 9.8: Fiducial cross section for electroweak $W^{\pm}W^{\pm}jj$ production, determined using WHIZARD and scaled to include interference, as a function of α_4 and α_5. Contours of constant cross section form ellipses in the (α_4, α_5) plane.

The time required to generate all of these points with full detector simulation is prohibitive, so a coarse grid of points is used to derive a correction for the efficiency of an event in the fiducial region to be reconstructed in the signal region. The efficiency is found to depend linearly on the fiducial cross section for electroweak $W^{\pm}W^{\pm}jj$ production. The linear fits are shown in Figure 9.9. Over the range of aQGC points considered, the efficiency varies by about 35% in the ee channel and 10% in the $e\mu$ and $\mu\mu$ channels. The difference between the efficiency predicted for the Standard Model ($\alpha_4 = \alpha_5 = 0$) using this method and the efficiency derived using the SHERPA sample is taken as an additional uncertainty.

The resulting 95% CL exclusion is shown in Figure 9.10. Due to the small excess in the VBS signal region, the observed limits are slightly weaker than expected. Profile likelihoods as a function of α_4 with $\alpha_5 = 0$ and vice

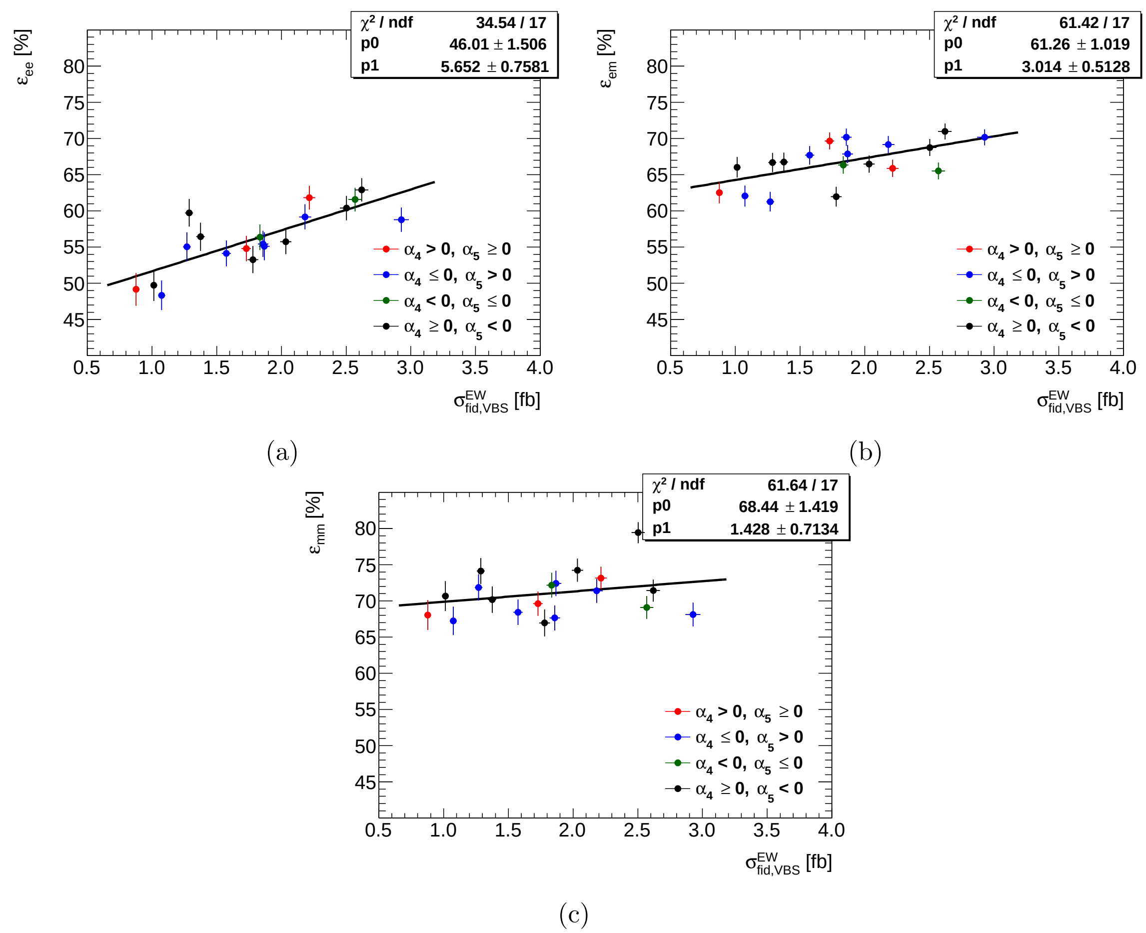

Figure 9.9: Efficiency as a function of the fiducial cross section for electroweak $W^{\pm}W^{\pm}jj$ production in the VBS SR for (a) the ee channel, (b) the $e\mu$ channel, and (c) the $\mu\mu$ channel.

versa are shown in Figure 9.11. The resulting one-dimensional limits on the parameters are $-0.14 < \alpha_4 < 0.16$ and $-0.23 < \alpha_5 < 0.24$.

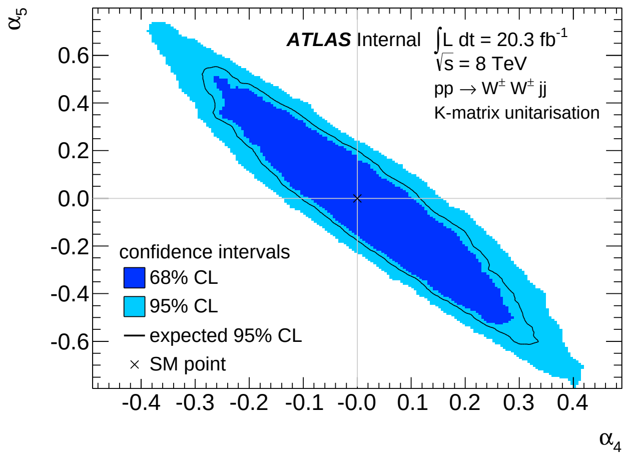

Figure 9.10: Limits on (α_4, α_5). Points outside the light blue ellipse are excluded at 95% CL while points outside the dark blue ellipse are excluded at 68% CL.

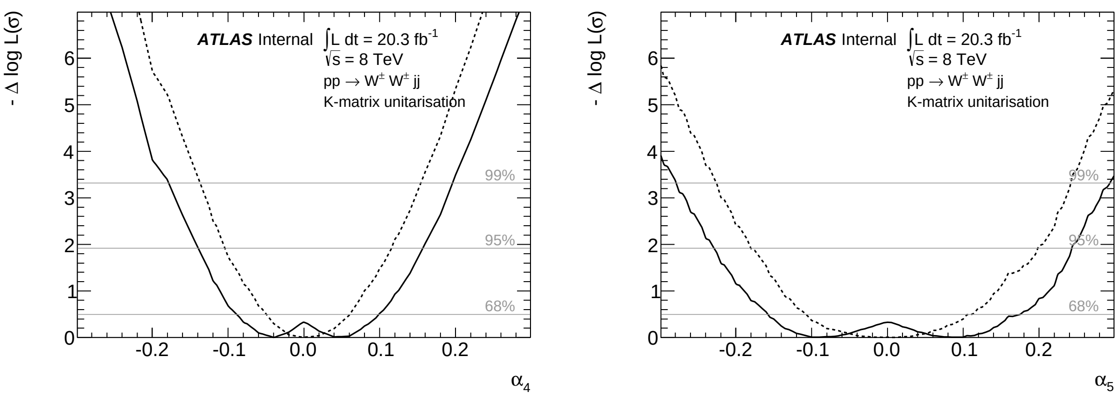

Figure 9.11: Expected (dashed) and observed (solid) profile likelihoods as a function of α_4 (left) and α_5 (right).

Chapter 10

Conclusions and Outlook

Two measurements of fiducial cross sections for $W^{\pm}W^{\pm}jj$ production and its electroweak component have been performed using proton-proton collisions with a center-of-mass energy of 8 TeV at the LHC. The collision data used for these measurements was collected in 2012 using the ATLAS detector and corresponds to an integrated luminosity of 20.3 fb^{-1}. The fiducial cross section for inclusive $W^{\pm}W^{\pm}jj$ production has been measured in events with two leptons with the same electric charge, missing transverse energy, and at least two jets with a large invariant mass. The measurement of the electroweak production of $W^{\pm}W^{\pm}jj$ is performed after making an additional requirement that the two leading jets have a large separation in rapidity.

In the inclusive signal region, 50 events are observed with 20 events expected from background process. The statistical significance of the excess in this region is 4.5σ. In the VBS signal region, 16 background events are expected and 34 are observed, giving a significance of 3.6σ. In both cases, the kinematic distributions of the observed excess are consistent with the Standard Model prediction for $W^{\pm}W^{\pm}jj$ production. The cross section measured in the inclusive region is 2.1 $\pm$ 0.5(stat.) $\pm$ 0.3(syst.) fb, and the cross section measured in the VBS region (for electroweak production) is 1.3 $\pm$ 0.4(stat.) $\pm$ 0.2(syst.) fb. This agrees with the Standard Model predictions of 1.52 $\pm$ 0.11 fb and 0.95 $\pm$ 0.06 fb. Using the VBS signal region, limits have also been placed on aQGC parameters α_4 and α_5 in the electroweak chiral Lagrangian framework with K-matrix unitarization applied. In the case where one of the two parameters is fixed to zero, the 95% CL limits are $-0.14 < \alpha_4 < 0.16$ and $-0.23 < \alpha_5 < 0.24$, which improve on existing upper bounds from electroweak precision measurements of $\alpha_4 < 0.30$ and $\alpha_5 < 0.76$.

The LHC will resume running in 2015 starting with a center-of-mass energy of 13 TeV and eventually reaching the design energy of 14 TeV. Run 2 is scheduled to go until 2018, followed by another shutdown and another run from 2020-2022. The most exciting possibility for the next run is the possibility of new physics existing at energies of a few TeV, leading to the discovery of new particles. However, even if the energy scale of new physics is too large for direct detection at the LHC, the increase in energy will bring an increase in sensitivity to anomalous gauge couplings that may be induced if the new physics couples to electroweak gauge bosons. Since the dominant uncertainties on the measurement presented in this dissertation are due to statistics, a similar $W^{\pm}W^{\pm}jj$ measurement in the next run will also benefit just from the increase in the amount of collision data.

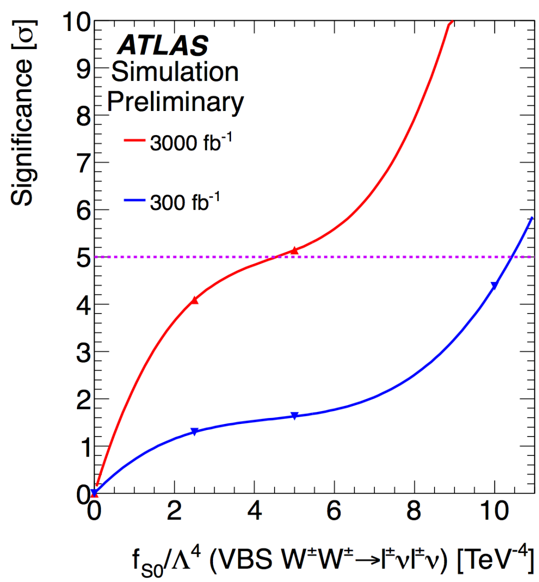

Figure 10.1: Projected sensitivity to the $\frac{f_{S,0}}{\Lambda^4}$ coupling from future measurements of $W^{\pm}W^{\pm}jj$ production at the LHC.

The luminosity projected for Run 2 is ∼80-100 fb^{-1}, with another ∼200 fb^{-1} of data expected in Run 3. Figure 10.1 shows a projection of the sensitivity to the $\frac{f_{S,0}}{\Lambda^4}$ parameters with 300 fb^{-1} of data at 14 TeV [92], roughly corresponding to the end of Run 3. The number of $W^{\pm}W^{\pm}jj$ events in this sample with $m_{jj} > 1$ TeV is expected to be ∼500. Anomalous couplings as low as 10 TeV^{-4} are projected to be observable at this point. The corresponding value of α_4 is about 0.0046. The increase in statistics will also make measurements of differential distributions possible. In short, $W^{\pm}W^{\pm}jj$ production remains a promising process for the study of electroweak symmetry breaking in the next run of the LHC. The current measurement has served to again confirm the Standard Model, but hopefully the next run will give us a peek at something new.

Bibliography

[1] D. Espriu and B. Yencho, Phys. Rev. D **87**, no. 5, 055017 (2013) [arXiv:1212.4158 [hep-ph]].

[2] J. Chang, K. Cheung, C. T. Lu and T. C. Yuan, Phys. Rev. D **87**, no. 9, 093005 (2013) [arXiv:1303.6335 [hep-ph]].

[3] M. J. G. Veltman, Acta Phys. Polon. B **8**, 475 (1977).

[4] B. W. Lee, C. Quigg and H. B. Thacker, Phys. Rev. Lett. **38**, 883 (1977).

[5] B. W. Lee, C. Quigg and H. B. Thacker, Phys. Rev. D **16**, 1519 (1977).

[6] G. Aad *et al.* [ATLAS Collaboration], Phys. Rev. Lett. **113**, 141803 (2014) [arXiv:1405.6241 [hep-ex]].

[7] M. E. Peskin and D. V. Schroeder, An Introduction to Quantum Field Theory. Westview Press, 1995.

[8] K.A. Olive et al. (Particle Data Group), Chin. Phys. C **38**, 090001 (2014).

[9] G. Aad *et al.* [ATLAS Collaboration], Phys. Lett. B **716**, 1 (2012) [arXiv:1207.7214 [hep-ex]].

[10] S. Chatrchyan *et al.* [CMS Collaboration], Phys. Lett. B **716**, 30 (2012) [arXiv:1207.7235 [hep-ex]].

[11] G. 't Hooft and M. J. G. Veltman, Nucl. Phys. B **44**, 189 (1972).

[12] H. L. Lai, M. Guzzi, J. Huston, Z. Li, P. M. Nadolsky, J. Pumplin and C.-P. Yuan, Phys. Rev. D **82**, 074024 (2010) [arXiv:1007.2241 [hep-ph]].

[13] The Durham HepData Project (2014). `http://hepdata.cedar.ac.uk/pdf/pdf3.html`

[14] T. Appelquist and G. H. Wu, Phys. Rev. D **48**, 3235 (1993) [hep-ph/9304240].

[15] S. Schael *et al.* [ALEPH and DELPHI and L3 and OPAL and LEP Electroweak Collaborations], Phys. Rept. **532**, 119 (2013) [arXiv:1302.3415 [hep-ex]].

[16] V. M. Abazov *et al.* [D0 Collaboration], Phys. Lett. B **718**, 451 (2012) [arXiv:1208.5458 [hep-ex]].

[17] G. Aad *et al.* [ATLAS Collaboration], Phys. Rev. D **87**, no. 11, 112003 (2013) [arXiv:1302.1283 [hep-ex]].

[18] G. Aad *et al.* [ATLAS Collaboration], arXiv:1410.7238 [hep-ex].

[19] G. Aad *et al.* [ATLAS Collaboration], Phys. Rev. D **87**, no. 11, 112001 (2013) [Erratum-ibid. D **88**, no. 7, 079906 (2013)] [arXiv:1210.2979 [hep-ex]].

[20] G. Aad *et al.* [ATLAS Collaboration], Eur. Phys. J. C **72**, 2173 (2012) [arXiv:1208.1390 [hep-ex]].

[21] G. Aad *et al.* [ATLAS Collaboration], JHEP **1404**, 031 (2014) [arXiv:1401.7610 [hep-ex]].

[22] T. Aaltonen *et al.* [CDF Collaboration], Phys. Rev. Lett. **107**, 051802 (2011) [arXiv:1103.2990 [hep-ex]].

[23] G. Aad *et al.* [ATLAS Collaboration], JHEP **1303**, 128 (2013) [arXiv:1211.6096 [hep-ex]].

[24] S. Chatrchyan *et al.* [CMS Collaboration], Phys. Rev. D **89**, 092005 (2014) [arXiv:1308.6832 [hep-ex]].

[25] S. Chatrchyan *et al.* [CMS Collaboration], Eur. Phys. J. C **73**, 2610 (2013) [arXiv:1306.1126 [hep-ex]].

[26] S. Chatrchyan *et al.* [CMS Collaboration], Eur. Phys. J. C **73**, 2283 (2013) [arXiv:1210.7544 [hep-ex]].

[27] S. Chatrchyan *et al.* [CMS Collaboration], JHEP **1310**, 164 (2013) [arXiv:1309.1117 [hep-ex]].

[28] S. Chatrchyan *et al.* [CMS Collaboration], CMS-PAS-SMP-13-014 (2014).

[29] V. Khachatryan *et al.* [CMS Collaboration], arXiv:1406.0113 [hep-ex].

[30] S. Chatrchyan *et al.* [CMS Collaboration], CMS-PAS-SMP-12-016 (2013). `http://cds.cern.ch/record/1633371`

[31] P. Achard *et al.* [L3 Collaboration], Phys. Lett. B **527**, 29 (2002) [hep-ex/0111029].

[32] V. M. Abazov *et al.* [D0 Collaboration], Phys. Rev. D **88**, 012005 (2013) [arXiv:1305.1258 [hep-ex]].

[33] S. Chatrchyan *et al.* [CMS Collaboration], JHEP **1307**, 116 (2013) [arXiv:1305.5596 [hep-ex]].

[34] S. Chatrchyan *et al.* [CMS Collaboration], CMS-PAS-SMP-13-009 (2013). `https://cds.cern.ch/record/1563302`

[35] O. J. P. Eboli, M. C. Gonzalez-Garcia and J. K. Mizukoshi, Phys. Rev. D **74**, 073005 (2006) [hep-ph/0606118].

[36] M. Baak, A. Blondel, A. Bodek, R. Caputo, T. Corbett, C. Degrande, O. Eboli and J. Erler *et al.*, arXiv:1310.6708 [hep-ph].

[37] A. Alboteanu, W. Kilian and J. Reuter, JHEP **0811**, 010 (2008) [arXiv:0806.4145 [hep-ph]].

[38] L. Evans and P. Bryant, JINST **3**, S08001 (2008).

[39] CERN, Diagram of an LHC dipole magnet, CERN-DI-9906025 (1999).

[40] TE-EPC-LPC in LHC. `http://te-epc-lpc.web.cern.ch/te-epc-lpc/machines/lhc/general.stm`

[41] M. Benedikt, P. Collier, V. Mertens, J. Poole and K. Schindl, CERN-2004-003-V-3, CERN-2004-003.

[42] M. Lamont, J. Phys. Conf. Ser. **455**, 012001 (2013).

[43] G. Aad *et al.* [ATLAS Collaboration], "ATLAS Experiment - Public Luminosity Results." `twiki.cern.ch/twiki/bin/view/AtlasPublic/LuminosityPublicResults`

[44] G. Aad *et al.* [ATLAS Collaboration], JINST **3**, S08003 (2008).

[45] G. Aad *et al.* [ATLAS Collaboration], Eur. Phys. J. C **71** 1593 (2011).

[46] M. Aharrouche *et al.* [ATLAS Electromagnetic Barrel Calorimeter Collaboration], Nucl. Instrum. Meth. A **568**, 601 (2006) [physics/0608012].

[47] G. Aad *et al.* [ATLAS Collaboration], CERN-LHCC-96-42.

[48] B. Dowler *et al.* [ATLAS Liquid Argon HEC Collaboration], Nucl. Instrum. Meth. A **482**, 94 (2002).

[49] J. P. Archambault, A. Artamonov, M. Cadabeschi, V. Epshteyn, C. Galt, P. Gorbounov, L. Heelan and M. Khakzad *et al.*, JINST **3**, P02002 (2008).

[50] G. Aad *et al.* [ATLAS Collaboration], Eur. Phys. J. C **70**, 875 (2010) [arXiv:1006.4384 [physics.ins-det]].

[51] G. Aad *et al.* [ATLAS Collaboration], arXiv:0901.0512 [hep-ex].

[52] G. Aad *et al.* [ATLAS Collaboration], ATLAS-CONF-2010-069 (2010). `https://cds.cern.ch/record/1281344`

[53] G. Aad *et al.* [ATLAS Collaboration], New J. Phys. **13**, 053033 (2011) [arXiv:1012.5104 [hep-ex]].

[54] G. Aad *et al.* [ATLAS Collaboration], Eur. Phys. J. C **72**, 1909 (2012) [arXiv:1110.3174 [hep-ex]].

[55] G. Aad *et al.* [ATLAS Collaboration], ATLAS-CONF-2014-32 (2014). `http://cds.cern.ch/record/1706245`

[56] G. Aad *et al.* [ATLAS Collaboration], Eur. Phys. J. C **74**, no. 10, 3071 (2014) [arXiv:1407.5063 [hep-ex]].

[57] R. Nicolaidou, L. Chevalier, S. Hassani, J. F. Laporte, E. Le Menedeu and A. Ouraou, J. Phys. Conf. Ser. **219**, 032052 (2010).

[58] G. Aad *et al.* [ATLAS Collaboration], arXiv:1407.3935 [hep-ex].

[59] G. Aad *et al.* [ATLAS Collaboration], Eur. Phys. J. C **73**, 2304 (2013) [arXiv:1112.6426 [hep-ex]].

[60] M. Cacciari, G. P. Salam and G. Soyez, JHEP **0804**, 063 (2008) [arXiv:0802.1189 [hep-ph]].

[61] G. Aad *et al.* [ATLAS Collaboration], "ATLAS Experiment - Public Results." `twiki.cern.ch/twiki/bin/view/AtlasPublic/JetEtmissApproved2013Jer2011`

[62] G. Aad *et al.* [ATLAS Collaboration], Eur. Phys. J. C **73**, 2306 (2013) [arXiv:1210.6210 [hep-ex]].

[63] G. Aad *et al.* [ATLAS Collaboration], ATLAS-CONF-2013-083 (2013). `http://cds.cern.ch/record/1570994`

[64] G. Aad *et al.* [ATLAS Collaboration], "ATLAS Experiment - Public Results." `twiki.cern.ch/twiki/bin/view/AtlasPublic/JetEtmissApproved2011PileupOffsetAndJVF`

[65] G. Aad *et al.* [ATLAS Collaboration], ATLAS-CONF-2011-102 (2011). `http://cds.cern.ch/record/1369219`

[66] G. Aad *et al.* [ATLAS Collaboration], ATLAS-CONF-2014-046 (2014). `http://cds.cern.ch/record/1741020`

[67] G. Aad *et al.* [ATLAS Collaboration], Eur. Phys. J. C **72**, 1844 (2012) [arXiv:1108.5602 [hep-ex]].

[68] G. Aad *et al.* [ATLAS Collaboration], ATLAS-CONF-2013-082 (2013). https://cds.cern.ch/record/1570993

[69] G. Aad *et al.* [ATLAS Collaboration], JINST **9**, P07024 (2014) [arXiv:1405.3768 [hep-ex]].

[70] G. Aad *et al.* [ATLAS Collaboration], Eur. Phys. J. C **70**, 787 (2010) [arXiv:1004.5293 [physics.ins-det]].

[71] S. Agostinelli *et al.* [GEANT4 Collaboration], Nucl. Instrum. Meth. A **506**, 250 (2003).

[72] T. Gleisberg, S. Hoeche, F. Krauss, M. Schonherr, S. Schumann, F. Siegert and J. Winter, JHEP **0902**, 007 (2009) [arXiv:0811.4622 [hep-ph]].

[73] P. Nason, JHEP **0411**, 040 (2004) [hep-ph/0409146]; S. Frixione, P. Nason and C. Oleari, JHEP **0711**, 070 (2007) [arXiv:0709.2092 [hep-ph]]; S. Alioli, P. Nason, C. Oleari and E. Re, JHEP **1006**, 043 (2010) [arXiv:1002.2581 [hep-ph]].

[74] B. Jager, C. Oleari and D. Zeppenfeld, Phys. Rev. D **80**, 034022 (2009) [arXiv:0907.0580 [hep-ph]]; B. Jager and G. Zanderighi, JHEP **1111**, 055 (2011) [arXiv:1108.0864 [hep-ph]]; T. Melia, K. Melnikov, R. Rontsch and G. Zanderighi, JHEP **1012**, 053 (2010) [arXiv:1007.5313 [hep-ph]];

T. Melia, P. Nason, R. Rontsch and G. Zanderighi, Eur. Phys. J. C **71**, 1670 (2011) [arXiv:1102.4846 [hep-ph]].

[75] T. Sjostrand, S. Mrenna and P. Z. Skands, JHEP **0605**, 026 (2006) [hep-ph/0603175]; T. Sjostrand, S. Mrenna and P. Z. Skands, Comput. Phys. Commun. **178**, 852 (2008) [arXiv:0710.3820 [hep-ph]].

[76] G. Aad *et al.* [ATLAS Collaboration], ATL-PHYS-PUB-2012-003 (2012).

[77] K. Arnold, M. Bahr, G. Bozzi, F. Campanario, C. Englert, T. Figy, N. Greiner and C. Hackstein *et al.*, Comput. Phys. Commun. **180**, 1661 (2009) [arXiv:0811.4559 [hep-ph]]; K. Arnold, J. Bellm, G. Bozzi, M. Brieg, F. Campanario, C. Englert, B. Feigl and J. Frank *et al.*, arXiv:1107.4038 [hep-ph]; K. Arnold, J. Bellm, G. Bozzi, F. Campanario, C. Englert, B. Feigl, J. Frank and T. Figy *et al.*, arXiv:1207.4975 [hep-ph]; B. Jager, C. Oleari and D. Zeppenfeld, Phys. Rev. D **80**, 034022 (2009) [arXiv:0907.0580 [hep-ph]].

[78] J. Alwall, P. Demin, S. de Visscher, R. Frederix, M. Herquet, F. Maltoni, T. Plehn and D. L. Rainwater *et al.*, JHEP **0709**, 028 (2007) [arXiv:0706.2334 [hep-ph]].

[79] M. L. Mangano, M. Moretti, F. Piccinini, R. Pittau and A. D. Polosa, JHEP **0307**, 001 (2003) [hep-ph/0206293].

[80] G. Corcella, I. G. Knowles, G. Marchesini, S. Moretti, K. Odagiri, P. Richardson, M. H. Seymour and B. R. Webber, JHEP **0101**, 010 (2001) [hep-ph/0011363].

[81] J. M. Butterworth, J. R. Forshaw and M. H. Seymour, Z. Phys. C **72**, 637 (1996) [hep-ph/9601371].

[82] J. M. Campbell and R. K. Ellis, JHEP **1207**, 052 (2012) [arXiv:1204.5678 [hep-ph]].

[83] G. Aad *et al.* [ATLAS Collaboration], arXiv:1406.0076 [hep-ex].

[84] G. Aad *et al.* [ATLAS Collaboration], ATLAS-CONF-2014-004 (2014). `https://cds.cern.ch/record/1664335`

[85] G. Aad *et al.* [ATLAS Collaboration], ATLAS-CONF-2011-116 (2011). `http://cds.cern.ch/record/1376384`

[86] G. Aad *et al.* [ATLAS Collaboration], ATLAS-CONF-2012-053 (2012). `http://cds.cern.ch/record/1452641`

[87] G. Cowan, K. Cranmer, E. Gross and O. Vitells, Eur. Phys. J. C **71**, 1554 (2011) [arXiv:1007.1727 [physics.data-an]].

[88] W. Kilian, T. Ohl and J. Reuter, Eur. Phys. J. C **71**, 1742 (2011) [arXiv:0708.4233 [hep-ph]]; M. Moretti, T. Ohl and J. Reuter, In *2nd ECFA/DESY Study 1998-2001* 1981-2009 [hep-ph/0102195].

[89] A. Brunstein, O. J. P. Eboli and M. C. Gonzalez-Garcia, Phys. Lett. B **375**, 233 (1996) [hep-ph/9602264].

[90] M. E. Peskin and T. Takeuchi, Phys. Rev. Lett. **65**, 964 (1990).

[91] P. Sikivie, L. Susskind, M. B. Voloshin and V. I. Zakharov, Nucl. Phys. B **173**, 189 (1980).

[92] G. Aad *et al.* [ATLAS Collaboration], ATL-PHYS-PUB-2013-006 (2013). `http://cds.cern.ch/record/1558703`

[93] FE-I4 Collaboration, “The FE-I4B Integrated Circuit Guide”, version 2.3 (2012).

Appendix A

Description of Author Contributions

The measurement presented in this dissertation is result of the collaborative effort of thousands of people spanning two decades. The purpose of this appendix is to highlight the experience that I have gained with a brief description of tasks in which I was directly involved. These can be separated into three broad categories: hardware, software, and data analysis.

Since the ATLAS detector was already built and taking data by the time I joined the experiment in 2010, my work on hardware has been towards future upgrades. All of my work in this area has been with a next-generation pixel chip, designated the "FE-I4," that was used in the Insertable Barrel Layer (IBL), a fourth layer added to the pixel detector during the shutdown that started in 2013. I performed tests of the digital logic of the chip design using Verilog simulations. The chip has independent parameters for setting the voltage reference and rise time of individual pixels. I contributed to software for tuning these parameters that was used in tests of chip performance. A new feature in the FE-I4 is the presence of self-monitoring signals that track potentially interesting quantities like temperature and leakage currents. I helped write firmware for reading out these signals in the IBL.

My involvement in ATLAS software has been confined to monitoring tracking software updates. Developers in ATLAS are continually seeking to improve track reconstruction. Updates are tested nightly by making a standard set of plots with several MC samples. These are compared to those made with previous versions of the software, both to confirm expected improvement and to catch any unexpected changes. In addition to taking shifts monitoring nightly tests, I inherited management of the software package use to make the monitoring plots and have been responsible for updating it as necessary to remain compatible with newer ATLAS software.

The bulk of my effort has been in data analysis. For the $W^{\pm}W^{\pm}jj$ measurement, I performed several studies on optimizing event selections and the isolation criteria for leptons, wrote software for generating plots and tables for each signal and control region, and estimated the impact of experimental uncertainties on the signal/control region predictions. I investigated discrepancies between data and prediction in the control regions to look for evidence of additional backgrounds or systematic effects that were unaccounted for. I also performed cross-checks of fake rate uncertainties using high-d_0 muons as described in Chapter 7 and jet energy scale uncertainties using the Z+jet studies described in Chapter 8.

Appendix B

The FE-I4 Chip

The FE-I4 is a new pixel chip [93] that has been used in the Insertable B-Layer (IBL), a fourth barrel layer added to the ATLAS pixel detector during the 2013/2014 shutdown. The main improvement over the FE-I3 chip used in the rest of the pixel detector is a smaller pixel size. Pixels on the FE-I4 measure 50 μm$\times$ 250 μm, down from 50 μm$\times$ 400 μm. Additional features of the FE-I4 include on-board monitoring signals, internal error logging counters, and a clock multiplier to support high-speed readout. Two voltage regulators (one for analog voltage and one for digital voltage) mitigate the effect of variations in the supply voltage on the voltage received by the chip. The nominal supply voltage is 1.8 V, but the regulators allow operation anywhere between 1.5 V and 2.5 V.

B.1 Single Pixel

The circuit diagram for a single pixel is shown in Figure B.1. The octagon on the left indicates where the pixel is bonded to the sensor. During normal operation, this is where charge would be collected. For purposes of tuning and testing the pixel, there is a built-in capability to inject charge by sending a voltage pulse, sometimes called a "calibration pulse," across the capacitors, C_{inj1}, C_{inj2}. The input signal goes through a two-stage amplifier before being fed into a comparator. When the amplified input signal exceeds the reference voltage of the comparator, the number of clock cycles for which it remains above the reference voltage is recorded as a 4-bit time-over-threshold (ToT) measurement.

The sensitivity pixels can be tuned globally by changing the reference voltages supplied to all pixels (V_{th}, V_{fb}, and V_{fb2}) or locally by adjusting values stored in a local pixel register that are fed into digital-to-analog converters (DACs) to provide additional reference voltages (FDAC, TDAC). The TDAC and V_{th} set the reference voltage of the comparator and can be used to shift the threshold charge required to register a hit. The FDAC, V_{fb}, and V_{fb2} adjust feedback capacitances in the amplifier, affecting both the rise time and the gain. This allows one to tune the ToT corresponding to a given input signal but can also change the threshold. The chip also contains a single analog output, into which the signals of several pixels, at different stages in the analog circuit, are multiplexed. This output can be used to test that a pixel circuit is performing properly.

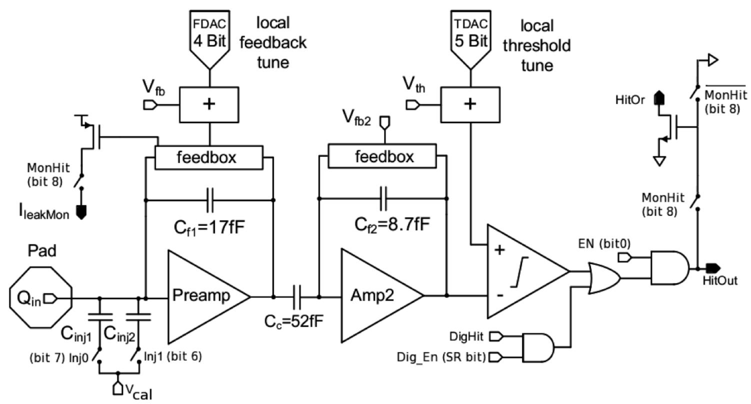

Figure B.1: Schematic of an analog pixel circuit for the FE-I4. Figure taken from Ref. [93]

B.2 Overall Structure

Pixels are arranged into 40 double-columns with 336 rows. Pixel hits are stored in memory blocks shared by a 2×2 block of pixels while waiting for a trigger to be issued. Each memory block can hold up to 5 hits at a time. If a certain number of clock cycles pass without a trigger a hit will be discarded. This number is called the trigger latency and is configurable. Once a trigger is received, hits are read in time order, formatted, and stored in an asynchronous FIFO (first-in-first-out) register until they are read by the data output block. The FIFO can accommodate up to 8 hits at a time and will assert a "FIFO full" signal to stop output from the data formatter if it becomes full. A global register is used to store configuration data that is independent of specific pixels, like the trigger latency and reference voltages, V_{th}, V_{fb}, and V_{fb2}. It is also used in the readout of the on-chip monitoring signals. An illustration of the FE-I4 layout is shown in Figure B.2.

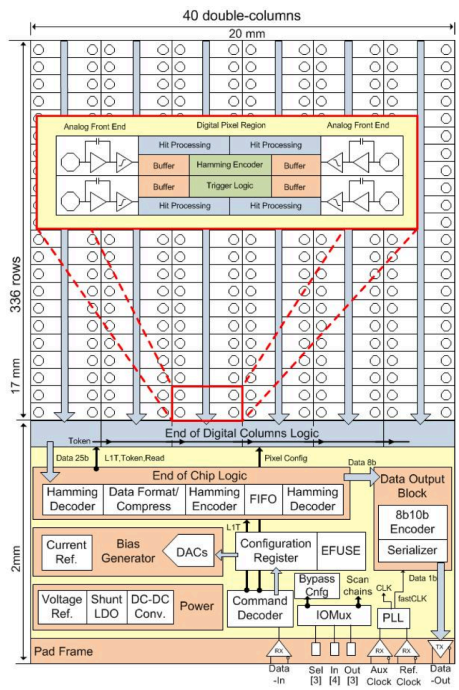

Figure B.2: Schematic drawing showing the layout of the FE-I4 chip, not drawn to scale. Figure taken from Ref. [93]

B.3 Generic ADC

Not pictured in Figure B.2 is the 10-bit generic analog-to-digital converter (GADC), which digitizes various analog monitoring signals. The signal to be fed into the GADC is selected using a multiplexer, and the selection bits given to the multiplexer are stored in the global register. The signals that feed into the multiplexer are: the output of a temperature sensor, that reference voltage supplied to the GADC, the analog ground, the analog output, the analog regulator current, the output of a 10-bit DAC used for calibration pulses, half the regulated analog voltage, and leakage current from the pixels, shown on the upper-left in Figure B.1. Output of the GADC is not automatically stored. A command must be sent to the chip to write the output to the global register. Then it can be read from the global register into the FIFO and finally sent out through the data output block.